Title
Cooperative force generation by actin assembly and myosin-I during endocytosis

Author
Pedersen, Ross Thomas Ambro

Publication Date
2019

Peer reviewed|Thesis/dissertation

Cooperative force generation by actin assembly and myosin-I during endocytosis

By

Ross TA Pedersen

A dissertation submitted in partial satisfaction of

the requirements for the degree of

Doctor of Philosophy

in

Molecular and Cell Biology

in the

Graduate Division

of the

University of California, Berkeley

Committee in charge:

Professor David G Drubin, Chair
Professor Matthew D Welch
Professor Douglas E Koshland
Professor Daniel A Fletcher

Summer 2019

Cooperative force generation by actin assembly and myosin-I during endocytosis

Abstract

Cooperative force generation by actin assembly and myosin-I during endocytosis

by

Ross TA Pedersen

Doctor of Philosophy in Molecular and Cell Biology

University of California, Berkeley

Professor David G Drubin, Chair

Clathrin-mediated endocytosis (CME) is a fundamental cellular membrane trafficking process. The process generates nascent cytoplasmic vesicles from the plasma membrane through a molecular pathway that brings about membrane invagination and scission. Over the last 2 decades, extensive studies in the budding yeast *Saccharomyces cerevisiae* have identified many of the molecules involved in the CME pathway. More than 60 proteins localize to CME sites in distinct spatial and temporal patterns. Initially, the earliest arriving proteins mark the presumptive CME site on the plasma membrane and initiate the assembly of an endocytic coat complex. The timing of this stage of CME is quite variable (< 30 s to > 4 min.). Eventually, additional coat proteins are recruited and the site transitions into a fast, regular phase (~30 s). Later arriving coat proteins recruit actin assembly factors, triggering a burst of actin assembly that invaginates the membrane facilitating scission. Despite the known identities of scores of proteins involved in CME, the molecular mechanisms of the process are incompletely understood. My dissertation work provides important mechanistic details into the molecular mechanism of force generation for membrane invagination and the molecular mechanisms governing the transition from the early, variably-times phase of CME into the later, more regular phase.

The actin cytoskeleton can generate force on membranes either through its assembly, its associated myosin motors, or both. How actin assembly and myosin motor activity are coordinated during processes that require both modes of force generation was unclear. Most recent studies of CME treat the process as an actin assembly-based force generation process. However, in budding yeast, type I myosins (Myo3 or Myo5) are also required. In Chapter 2 of this dissertation, I demonstrate that membrane binding by the type I myosin Myo5 constitutes a critical membrane anchor for actin assembly at endocytic sites, facilitating actin-assembly based force generation. In Chapter 3, I demonstrate that the Myo5 motor itself is also capable of generating appreciable force, indicating that actin assembly can be assisted by myosin activity to bring about membrane morphogenesis.

After initiation, CME sites enter a variably-timed early phase before maturing through a transition point into a phase of more regular kinetics. A previous study from our lab demonstrated that the presence of CME cargo is necessary for efficient maturation through the transition point. In Chapter 4 of this dissertation, I demonstrate that the presence of cargo is also sufficient to drive accelerated maturation through the transition

point. In addition to providing insight into the mechanisms of CME progression, this observation also explains the longstanding observation that late CME markers are polarized towards sites of cell growth. Since the majority of secretory traffic is directed towards sites of cell growth, endocytic cargos are likely to be concentrated there, accelerating maturation of CME sites into the regular late phase of the process.

For my parents and grandparents

Table of Contents

Figures

Tables

Abbreviations

CME	Clathrin-mediated endocytosis
WASP	Wiscott-Aldrich syndrome protein
WIP	WASP interacting protein
PRD	Proline rich domain
SH3	Src homology 3
BAR	Bin1 Amphiphysin RVS
F-actin	Filamentous actin
PM	Plasma membrane
NPF	Nucleation promoting factor
C-terminal	Carboxy-terminal
TIRFM	Total internal reflection fluorescence microscopy
TH1	Tail homology 1
TH2	Tail homology 2
CA	Connector/acidic.
NA	Numerical Aperture
TORC2	Target of rapamycin complex 2
ORF	Open reading frame

Acknowledgements

This work would not have been possible without the mentorship and support of my colleagues, friends, and loved ones.

David Drubin has been the most generous advisor I could possibly ask for. I was lucky to have gotten two advisors for the price of one: I would not have made it through the ups and downs of graduate school without the support of Georjana Barnes. I will forever be grateful to have had the opportunity to work in the rigorous, intellectually intense, laboratory environment cultivated by David and Georjana. If I am successful in my chosen career path, it will be because of the fantastic mentoring that I received in the Drubin/Barnes laboratory.

Labmates and colleagues that have helped me along the way are too numerous to list. I would not have mastered most of the technical skills that I have in graduate school without the patient guidance of my coworkers not just in the Drubin/Barnes laboratory, but also in the Thorner and Koshland laboratories. I am grateful to the members of all of these labs for making me feel welcome to ask questions. I am also indebted to Matthew Welch and the Welch lab for broadening my scientific horizons and tolerating my input. Graduate school would have been a lonely endeavor without any of these brilliant colleagues.

I will remember by years in Berkeley fondly primarily because of the friends I had here. Over the years, I have had a total of 6 roommates, without whom I would never have considered Berkeley home. I will forever remember Elizabeth, George, Allegra, Katie, Aaron, and Heather as my de facto graduate school family. When in need of a listening ear, I always know that I can turn to my friends in the Wednesday Night Drinking Club (on Thursday). Although we have scattered across the country, I know that I can always count on Kelsey, Addison, and Brian when I need them, and I will always be there for them, too. I have explored California with countless traveling partners. I would not trade those experiences for the world, and I hope that there are more adventures to come. Finally, I was lucky to have my friend Axel nearby through all of graduate school, keeping me true to my roots. Together, all of these people have made graduate school unforgettable (in a good way).

Finally, I thank my family and loved ones for their unwavering support through all of my years of education. The road to a doctoral degree is a very long one, and I would not have stayed on it without the encouragement of my family. My Parents, Tom and Alice, have always given me what I needed, and I realize how lucky that makes me. My grandparents, Harold and Audrey, have been a shining example for me of how to live the best life. Watching my sister and brother in law April and Tristan grow their family has been inspiring, and I am so glad to have two more family members to love since the start of graduate school: Camille and Edith. Loving a workaholic can be a challenge, but Kelsey has taken it on and carried me through some of the hardest months of my PhD. I would be lucky to have any of these loved ones in my life. I lead a charmed life because I get to have all of them in it.

Chapter 1 : General introduction: molecular determinants of progression through the budding yeast clathrin-mediated endocytic pathway

Clathrin-mediated endocytosis (CME) is a crucial membrane trafficking process wherein cells generate nascent intracellular vesicles from the plasma membrane. This is accomplished through a complex, robust, and highly conserved molecular pathway (Fig. 1.1). Initially, early arriving proteins and coat proteins including clathrin bind to the inner leaflet of the plasma membrane, marking the presumptive endocytic site (Godlee and Kaksonen, 2013). Over time, the coat remodels and, in most cases, recruits actin assembly factors to the CME site (Avinoam et al., 2015; Kaksonen et al., 2006). This matured CME machine brings about budding of the plasma membrane into a deep pit, which, with the help of membrane binding proteins and specific phospholipid organization, undergoes scission, releasing a vesicle into the cytoplasm (Kaksonen et al., 2006; Liu et al., 2006, 2009). This process allows cells to sample the extracellular environment by internalizing soluble materials from the extracellular space and also facilitates maintenance of membrane homeostasis by allowing cells to internalize components of the plasma membrane, such as phospholipids or membrane associated proteins.

For all of its molecular complexity, the CME pathway exists to accomplish two conceptually simple tasks: invaginating the plasma membrane into a deep tubule, and resolving the membrane tubule into a vesicle. When the plasma membrane is under low tension, the endocytic coat itself is capable of creating membrane pits. However, in situations where bending of the plasma membrane is resisted either by membrane tension or hydrostatic pressure, endocytic coats alone are insufficient to deform the plasma membrane, and the additional required force is provided by the actin cytoskeleton (Boulant et al., 2011; Aghamohammadzadeh and Ayscough, 2009). Even when actin assembly is not strictly required for membrane invagination, as in cultured animal cells, actin assembles at the vast majority of CME sites (Grassart et al., 2014), suggesting that cells ensure robustness of this process through constructing by default an endocytic machine that can invaginate the plasma membrane even if it resists deformation. Intriguingly, although membrane tension must be overcome for plasma membrane invagination, some amount of tension is also required for scission by the GTPase dynamin (Roux et al., 2006). Thus, cells must both overcome and harness membrane tension to accomplish the membrane reshaping required for CME. In a general sense, the CME pathway can be thought of as a means for building and operating a membrane-remodeling machine.

The budding yeast *Saccharomyces cerevisiae* is particularly useful for studying CME due to the extraordinary regularity of the pathway in this organism. In budding yeast, turgor pressure firmly presses the plasma membrane against the surrounding cell wall, creating a particularly acute requirement for F-actin assembly at every endocytic site (Aghamohammadzadeh and Ayscough, 2009). Combined with their highly tractable genetics, ease of examination by live-cell microscopy, and biochemical accessibility, the consistent CME pathway in *S. cerevisiae* has been invaluable in defining a parts list and dissecting mechanisms of CME (Boettner et al., 2012). Here I will briefly review our knowledge of the process of CME in *S. cerevisiae* and outline outstanding questions in the field.

Decades of research on CME in budding yeast have resulted in a list of over 60 proteins that localize to CME sites. These proteins can be sorted into several “modules” based on shared spatial and temporal behaviors: the early module of endocytic proteins establish endocytic sites and nucleate a coat module, the coat module in turn recruits a

WASP/Myosin module, which in turn triggers actin assembly and recruitment of the actin module and drives membrane invagination. Finally, proteins of the scission module bind to the neck of the endocytic invagination to bring about scission (Fig. 1.1, Lu et al., 2016; Kaksonen et al., 2005). While the field of CME has exhaustive knowledge of which proteins belong to each functional module, far less is known about how specific transitions within the CME pathway are controlled molecularly. Of particular interest are the mechanisms governing initiation of CME sites, maturation from a variable early phase of the pathway to a more regular later phase, initiation of actin assembly, membrane invagination, and vesicle scission (Fig. 1.1).

Initiation

The earliest arriving proteins that mark the presumptive endocytic site on the interior leaflet of the plasma membrane include Ede1, Syp1, Hrr25, Pal1, clathrin, the yeast AP2 complex homologue, and the yeast AP180 complex homologue (Kaksonen et al., 2005; Stimpson et al., 2009; Peng et al., 2015; Carroll et al., 2012, 2009). These proteins can be separated into an early module that disassembles before endocytic vesicle internalization and an early coat module that ultimately internalizes with the vesicle. Current data indicate that cargo arrives at CME sites only after they have been initiated (Toshima et al., 2006).

Despite extensive live cell imaging of early arriving CME proteins, the actual mechanism of site initiation remains unclear (Godlee and Kaksonen, 2013). No single early or early coat protein consistently arrives before the others, making it unlikely that a single protein nucleates site formation (Carroll et al., 2012). This conclusion is further supported by the observation that CME sites can still initiate when genes encoding any of the early or early coat proteins are deleted. *EDE1* deletion causes the most pronounced phenotype, dramatically reducing the number of CME sites (Kaksonen et al., 2005; Stimpson et al., 2009; Lu and Drubin, 2017). Deletion of *HRR25* causes a similar phenotype (Peng et al., 2015). However, in each of these mutants, CME sites do still initiate, albeit at a reduced rate, indicating that Ede1 and Hrr25 are not strictly required for initiation. Surprisingly, when genes encoding seven of the earliest arriving endocytic proteins including *EDE1* are simultaneously deleted, CME sites still initiate, although once again in lower numbers, similar to the *ede1Δ* phenotype (Brach et al., 2014). Phospholipids are also likely to play a role in site initiation. Most early arriving endocytic proteins bind directly to the inner leaflet of the plasma membrane, and depletion of phosphatidic acid from cells has been found to cause a reduction in the number of endocytic sites, similar to elimination of early arriving proteins (Sun and Drubin, 2012). Elimination of a variety of factors leads to partial loss of function phenotypes with respect to CME initiation, but how these factors cooperate to make CME initiation robust is unknown.

While no individual CME component is completely necessary for initiation, several of the earliest arriving proteins have been found to be sufficient to seed CME sites and recruit additional CME machinery. Tethering many of the earliest arriving proteins to eisosomes, areas of the plasma membrane typically devoid of CME sites, leads to subsequent recruitment of other early arriving proteins, although these sites do not go on to internalize (Brach et al., 2014). The minimal domains of Ede1 sufficient to localize it to the plasma membrane are also able to support seemingly wild-type CME initiation,

indicating that Ede1 is able to function in endocytic site initiation so long as it can localize to the membrane (Lu and Drubin, 2017). The highly robust nature of CME initiation may be partially explained by the fact that many factors seem to be sufficient to nucleate CME sites.

One important but poorly understood aspect of endocytic initiation is the role of posttranslational modification. Many of the earliest arriving CME proteins are extensively phosphorylated and one of them, Hrr25, is itself a protein kinase. Ubiquitylation is also likely an important signal, as permanently ubiquitylated versions of Ede1 drive aberrant endocytic site establishment on endosomal membranes (Weinberg and Drubin, 2014). Future research into how specific combinations of proteins can initiate CME sites and how posttranslational modifications play into this pathway could help shed light on the molecular mechanism of endocytic site selection.

Transition point

Regardless of the specific mechanism of initiation, once initiated, early CME sites remain stationary on the plasma membrane for a long (< 30s to >4 min.), variable period of time before proceeding into a period (~30sec) of more regular dynamics (Kaksonen et al., 2005; Newpher et al., 2005; Carroll et al., 2009, 2012; Stimpson et al., 2009). While the specific molecular changes that occur during this transition point remain unclear, the presence of cargo accelerates entry into the more regular later phases of CME. In small and medium budded cells, the majority of exocytic cargo is targeted to the bud for secretion, likely creating a localized concentration of endocytic cargo (Field and Schekman, 1980). Ede1 lifetimes in such buds are shorter, and therefore progression through the transition point is faster (Layton et al., 2011). Furthermore, blockage of exocytic traffic through use of a temperature sensitive allele increases Ede1 lifetimes, indicating that progression through the transition point is slower in the absence of cargo (Carroll et al., 2012). How the endocytic site changes at this transition point and how cargo triggers that change remains unclear to date.

Actin nucleation

Once CME sites have entered the regular phase of the CME pathway, actin assembly factors quickly accumulate and organize at endocytic sites. These proteins trigger assembly of a branched actin network that is nucleated by the Arp2/3 complex (Winter et al., 1997). The Arp2/3 complex on its own is a weak actin nucleator, but binding to filamentous actin (F-actin) and trans activators called nucleation promoting factors triggers a conformational change, activating the nucleation activity of the complex (Espinoza-Sanchez et al., 2018; Rodnick-Smith et al., 2016; Rodal et al., 2005b). Four Arp2/3 activating NPFs have been discovered within the CME pathway: the intersectin homologue Pan1, the Wiscott-Aldrich Syndrome protein (WASP) homologue Las17, Type I myosins Myo3 or Myo5 in cooperation with the WASP interacting protein (WIP) homologue Vrp1, and Abp1 (Duncan et al., 2001; Winter et al., 1999; Sun et al., 2006; Goode et al., 2001). Of these Arp2/3 complex activators, Las17 and is the most potent (Sun et al., 2006). Curiously, despite the fact that Las17 is not autoinhibited, it arrives at endocytic sites tens of seconds before actin

assembly is initiated (Rodal et al., 2003; Kaksonen et al., 2003). How activation of the Arp2/3 complex by Las17 is inhibited and how this inhibition is removed to initiate actin assembly is to-date unresolved. The actin assembly factors involved in CME are well known, but the mechanisms controlling them merit further research.

One possible mechanism for control of Las17 activity involves the binding of inhibitory proteins in trans. Two proteins in the CME pathway have been demonstrated to bind to Las17 and inhibit its ability to activate the Arp2/3 complex: Sla1 and Bbc1 (Rodal et al., 2003). Sla1 arrives at endocytic sites with similar timing to Las17 and is likely to be directly bound to Las17 in the cytoplasm, making it an attractive candidate for control of Las17 NPF activity during CME (Feliciano and Di Pietro, 2012). However, in *sla1Δ* and cells bearing *sla1* mutations rendering the expressed protein incapable of binding Las17, Las17 recruitment nevertheless precedes actin assembly, indicating that Sla1 is not solely responsible for controlling the timing of Las17 NPF activity (Kaksonen et al., 2005; Sun et al., 2017). Bbc1, on the other hand, arrives to endocytic sites after Las17 has already been activated, so it too cannot be the sole regulator of Las17 NPF activity (Kaksonen et al., 2005). Although these negative regulators could play important roles, fully accounting for Las17 regulation at endocytic sites requires invoking additional mechanisms.

One hint as to how Las17 NPF activity may be controlled comes from the observation that Las17 consistently accumulates to an apparent threshold level before actin assembly is triggered (Sun et al., 2017). Recruitment of sufficient levels of Las17 to endocytic sites depends upon multivalent interactions of src homology 3 (SH3) and proline rich domain (PRD) containing proteins within the CME coat and WASP/Myosin module (Sun et al., 2017). These same types of interactions have previously been shown to drive formation of higher order biomolecular condensates, and organization of NPF proteins into such condensates can regulate their ability to activate the Arp2/3 complex (Li et al., 2012; Case et al., 2019). Determining whether the apparent threshold level of Las17 or any NPF involved in CME indicates the formation of a biomolecular condensate may shed significant light upon how initiation of actin assembly is controlled at endocytic sites.

While considerable research has examined regulation of NPFs, the Arp2/3 complex can also be controlled by the presence or absence of mother filaments from which nascent actin branches are nucleated. How the initial mother filament at a CME site is generated is not well understood. In stark contrast with animal cells, budding yeast lack a dense actin cortex, so it is unlikely that actin assembly is seeded by preexisting cortical actin filaments near CME sites (Collins et al., 2011; Rodal et al., 2005a). Research on the fission yeast *Schizosaccharomyces pombe* has lead to two possible models of accounting for the initial mother actin filament. Chen and Pollard proposed that disassembly of actin following CME is incomplete, resulting in small F-actin seeds that are free to diffuse in the cytoplasm. Upon landing on a CME site primed with NPFs, these seed filaments would activate actin assembly by the Arp2/3 complex (Chen and Pollard, 2013). A different, but not mutually exclusive model involves the activity of the WISH/DIP/SPIN90 family protein Dip1, which activates the Arp2/3 complex in the absence of a mother filament and generates unbranched F-actin (Wagner et al., 2013; Balzer et al., 2018). Mutant cells lacking Dip1 manifest irregular timing of actin assembly at endocytic sites, possibly due to the lack of a suitable mother filament for Arp2/3 complex driven actin assembly (Basu and Chang, 2011). The *S. cerevisiae* homologue of Dip1, Ldb17, localizes to CME sites, but its function has not been thoroughly investigated (Burston et al., 2009). It is likely that the timing of

initiation of actin assembly at CME sites is controlled in part by both presence of mother filaments and biochemical inhibition of NPF proteins.

Invagination

The mechanism of membrane deformation by the actin cytoskeleton at CME sites has been researched extensively. Actin assembly is clearly required for the formation of deep membrane invaginations, since inhibition of actin assembly with the actin monomer sequestering drug Latrunculin A arrests CME sites at a flat or slightly dimpled stage (Kukulski et al., 2012; Idrissi et al., 2012). Furthermore, assembly of an endocytic actin network is itself capable of generating appreciable force, since plastic beads coated with actin assembly factors can assemble an actin tail and propel themselves about in crude yeast cytoplasmic extracts (Michelot et al., 2010). However, how the actin network is organized to produce sufficient force to invaginate the plasma membrane remains an area of intense interest.

The majority of research on budding yeast CME supports a cone-shaped model of actin organization with new monomers added to the actin network at the base of the endocytic pit near the plasma membrane and F-actin bound to the tip of the endocytic invagination by coat proteins (Kaksonen et al., 2006). In this organization, addition of new actin monomers to actin filaments near the plasma membrane would push the filaments deeper into the cytoplasm, dragging with them the tip of the endocytic invagination (Fig. 1.2A). Three major observations support this organizational model. First, the organization of actin assembly factors at CME sites suggests that most actin growth occurs at the base of the endocytic pit. The entire WASP/Myosin module, accounting for the majority of the NPF activity at CME sites, does not move into the cytoplasm with endocytic vesicles, leading to the conclusion that these proteins remain at the base of CME sites throughout the process (Kaksonen et al., 2005; Sun et al., 2006). The WASP/Myosin module proteins are organized as a ring around the presumptive invagination site, ensuring uniform growth of the actin network around the growing invagination (Mund et al., 2018). Second, elimination of the coat proteins responsible for coupling actin filaments to the tips of endocytic invaginations leads to a striking phenotype wherein large “fans” of actin stream off of the plasma membrane (Skruzny et al., 2012; Kaksonen et al., 2003). Within these aberrant actin structures, photobleached spots and fiduciary marks move away from the plasma membrane and toward the cytoplasm, indicating that actin monomers join the actin network near the plasma membrane and flow toward the cytoplasm (Kaksonen et al., 2003; Okreglak and Drubin, 2007, 2010; Lewellyn et al., 2015; Michelot et al., 2013). Finally, when fluorescence recovery after photobleaching experiments are performed on GFP labeled actin in CME sites within wildtype cells, the recovery pattern indicates that actin plus ends face the plasma membrane (Picco et al., 2015). A competing model for the organization of actin at endocytic sites comes from research on *S. pombe* and posits that force is generated by the opposed growth of two actin networks, one at the tip of endocytic pits and one at the base (Arasada et al., 2017; Arasada and Pollard, 2011). However at present, no data from *S. cerevisiae* support this organization; additional research will be required to reconcile these two models (Sun, Pollard, and Drubin, manuscript in

preparation). In all proposed organizations, actin assembly is assumed to be the major mode of force generation for CME.

Curiously, while CME has been largely considered to be driven by actin-assembly based forces, type I myosins are also required for the process (Geli and Riezman, 1996; Sun et al., 2006; Lewellyn et al., 2015; Idrissi et al., 2012). Myo3 and Myo5, the two type I myosins involved in CME, localize to the base of endocytic pits along with the WASP/Myosin module (Sun et al., 2006; Lewellyn et al., 2015). Interestingly, different type I myosins have been reported to have different load dependent kinetics (Greenberg and Ostap, 2013). While some Myosins I are capable of generating force against a resistive load, others are locked in a high actin affinity conformation under even very modest forces (Greenberg et al., 2012; Laakso et al., 2008). Determining how force sensitive the endocytic type I myosins are will shed light on whether myosins generate appreciable force for CME.

Scission

The driving force generated by the CME actin network facilitates deep invagination of the plasma membrane and the transition from a U-shaped tubule to an omega-shaped pit (Hassinger et al., 2017). In the omega configuration, the CME site is primed for membrane scission. Three main mechanisms have been invoked to account for scission of endocytic vesicles in *S. cerevisiae*, including the involvement of the budding yeast dynamin homologue Vps1, the generation of a line tension around CME tubules, and the influence of Bin/amphiphysin/RVS (BAR) proteins on the membrane at CME sites.

Canon holds that the GTPase dynamin facilitates scission of endocytic vesicles in plant and animal cells. Dynamin assembles as a helical polymer around membrane tubules and constricts to bring about membrane fission (Antonny et al., 2016). The *S. cerevisiae* homologue of dynamin, Vps1, has been reported to localize to CME sites, and *vps1Δ* mutants were reported to have defects in scission during CME (Smaczynska-de Rooij et al., 2010). This function of Vps1 depends upon its interaction with actin filaments, a possible means of coordinating membrane invagination and scission (Palmer et al., 2015). Curiously a different study reported no localization of Vps1 to CME sites and no scission defect in *vps1Δ* cells (Kishimoto et al., 2011). One possible explanation for this discrepancy is a difference in cell cycle state or cell growth phase in different experiments. The endocytic function of Vps1 is regulated by phosphorylation by Pho85, a kinase that is primarily active when nutrients are plentiful (Smaczynska-de Rooij et al., 2016; Huang et al., 2007). While current data are inconclusive, dynamin may be involved in scission of vesicles during CME in budding yeast.

An alternative mechanism to drive scission involves the generation of a line tension around CME tubules due to phospholipid phase boundaries. In this model, segregation of specific phospholipids along the length of a CME tubule creates a boundary between phospholipid phases. Such a boundary is energetically unfavorable due to intrinsic incompatibilities of the different phospholipids, such as hydrophobic mismatch. Decreasing the length of the phase boundary is therefore thermodynamically favored, creating a driving force that culminates in scission, i.e. complete elimination of the phospholipid phase boundary (Fig. 1.2B, Liu et al., 2006). In the original formulation of the model, segregation of phospholipids into different phases was proposed to be driven by the

immobility of phospholipids bound to membrane-binding proteins. Subsequent research demonstrated extensive biochemical modification of phospholipids at endocytic sites by the phosphoinositide phosphatase Sjl2 (Stefan et al., 2005; Sun et al., 2007; Toret et al., 2008), leading to a revised model dependent upon localized Phosphatidylinositol (4,5) bisphosphate consumption near the tip of endocytic invaginations (Liu et al., 2009). Whether or not such a line tension model can completely account for scission, it likely contributes to the process of CME.

Regardless of the specific mechanism of scission, there is broad consensus in the field that BAR proteins are crucial to the process. The *S. cerevisiae* BAR proteins Rvs161 and Rvs167 localize to CME sites around the time of vesicle scission, and Rvs161/167 deletion mutants manifest scission defects (Kishimoto et al., 2011; Kaksonen et al., 2005). These proteins may cooperate with Vps1 to cause vesicle scission (Smaczynska-de Rooij et al., 2012). They may also contribute to scission through stabilizing deep membrane invaginations, facilitating scission by one of the previously mentioned mechanisms (Kishimoto et al., 2011). One final exciting possibility is that the BAR proteins themselves drive scission during CME. If a BAR protein-coated membrane tubule is pulled with sufficient velocity, the BAR protein coating precludes flow of phospholipids into the tubule, eventually leading to scission of the tubule through lysis, a phenomenon termed friction-driven scission (Simunovic et al., 2017). Because CME is a highly robust process, it is likely that multiple mechanisms including dynamin activity, phase-boundary driven line tension, and friction-driven scission contribute to making the final cut.

Summary and other outstanding questions

Years of research have led to a detailed understanding of the process of CME. We now have an extensive parts list for the pathway, and even considerable knowledge about how the parts interact with one another. However, mechanistic knowledge of how progression through this crucial pathway is controlled remains limited. Here I have outlined several crucial transitions that remain partially mysterious.

Continued research into the CME pathway will not only provide further mechanistic understanding of the process of endocytosis, it will also indicate which steps in this process represent tunable transitions that can be modulated for physiological purposes. CME researchers should not forget that endocytosis is central to the things that cells do, including growth, signal transduction, and adaptation to available resources. Exciting recent research has examined how abundance of specific nutrients leads to endocytosis of the plasma membrane transporter for said nutrient (Lee et al., 2019; Busto et al., 2018; Becuwe et al., 2012). Other studies have demonstrated that the rate of CME can be tuned by relevant signal transduction pathways within the cytoplasm (Roelants et al., 2017). As our knowledge of the molecular mechanisms of CME becomes more extensive, we can begin to appreciate how the process fits in to larger scale biological systems.

Acknowledgments

I thank J. Hill for critically reading this chapter and C. Toret for providing the original diagram adapted for Figure 1.1.

References

Aghamohammadzadeh, S., and K.R. Ayscough. 2009. Differential requirements for actin during yeast and mammalian endocytosis. *Nat. Cell Biol.* 11:1039–1042. doi:10.1038/ncb1918.

Antonny, B., C. Burd, P. De Camilli, E. Chen, O. Daumke, K. Faelber, M. Ford, V.A. Frolov, A. Frost, J.E. Hinshaw, T. Kirchhausen, M.M. Kozlov, M. Lenz, H.H. Low, H. McMahon, C. Merrifield, T.D. Pollard, P.J. Robinson, A. Roux, and S. Schmid. 2016. Membrane fission by dynamin: what we know and what we need to know. *EMBO J.* 35:2270–2284. doi:10.15252/embj.201694613.

Arasada, R., and T.D. Pollard. 2011. Distinct roles for F-BAR proteins Cdc15p and Bzz1p in actin polymerization at sites of endocytosis in fission yeast. *Curr. Biol.* 21:1450–1459. doi:10.1016/j.cub.2011.07.046.

Arasada, R., W.A. Sayyad, J. Berro, and T.D. Pollard. 2017. High-speed superresolution imaging of the proteins in fission yeast clathrin-mediated endocytic actin patches. *Mol. Biol. Cell*. 29:295–303. doi:10.1091/mbc.e17-06-0415.

Avinoam, O., M. Schorb, C.J. Beese, J.A.G. Briggs, and M. Kaksonen. 2015. Endocytic sites mature by continuous bending and remodeling of the clathrin coat. *Science*. 348:1369–1372. doi:10.1126/science.aaa9555.

Balzer, C.J., A.R. Wagner, L.A. Helgeson, and B.J. Nolen. 2018. Dip1 Co-opts Features of Branching Nucleation to Create Linear Actin Filaments that Activate WASP-Bound Arp2/3 Complex. *Curr. Biol.* 28:3886-3891.e4. doi:10.1016/j.cub.2018.10.045.

Basu, R., and F. Chang. 2011. Characterization of Dip1p reveals a switch in Arp2/3-dependent actin assembly for fission yeast endocytosis. *Curr. Biol.* 21:905–16. doi:10.1016/j.cub.2011.04.047.

Becuwe, M., N. Vieira, D. Lara, J. Gomes-Rezende, C. Soares-Cunha, M. Casal, R. Haguenauer-Tsapis, O. Vincent, S. Paiva, and S. Léon. 2012. A molecular switch on an arrestin-like protein relays glucose signaling to transporter endocytosis. *J. Cell Biol.* 196:247–259. doi:10.1083/jcb.201109113.

Boettner, D.R., R.J. Chi, and S.K. Lemmon. 2012. Lessons from yeast for clathrin-mediated endocytosis. *Nat. Cell Biol.* 14:2–10. doi:10.1038/ncb2403.

Boulant, S., C. Kural, J.-C. Zeeh, F. Ubelmann, and T. Kirchhausen. 2011. Actin dynamics counteract membrane tension during clathrin-mediated endocytosis. *Nat. Cell Biol.* 13:1124–31. doi:10.1038/ncb2307.

Brach, T., C. Godlee, I. Moeller-Hansen, D. Boeke, and M. Kaksonen. 2014. The initiation of clathrin-mediated endocytosis is mechanistically highly flexible. *Curr. Biol.* 24:548–54. doi:10.1016/j.cub.2014.01.048.

Burston, H.E., L. Maldonado-Báez, M. Davey, B. Montpetit, C. Schluter, B. Wendland, and E. Conibear. 2009. Regulators of yeast endocytosis identified by systematic quantitative analysis. *J. Cell Biol.* 185:1097–1110. doi:10.1083/jcb.200811116.

Busto, J. V, A. Elting, D. Haase, F. Spira, J. Kuhlman, M. Schäfer-Herte, and R. Wedlich-Söldner. 2018. Lateral plasma membrane compartmentalization links protein function and turnover. *EMBO J.* 37:1–17. doi:10.15252/embj.201899473.

Carroll, S.Y., H.E.M. Stimpson, J. Weinberg, C.P. Toret, Y. Sun, and D.G. Drubin. 2012. Analysis of yeast endocytic site formation and maturation through a regulatory transition point. *Mol. Biol. Cell*. 23:657–668. doi:10.1091/mbc.E11-02-0108.

Carroll, S.Y., P.C. Stirling, H.E.M. Stimpson, E. Gießelmann, M.J. Schmitt, and D.G. Drubin. 2009. A Yeast Killer Toxin Screen Provides Insights into A/B Toxin Entry, Trafficking, and Killing Mechanisms. *Dev. Cell*. 17:552–560. doi:10.1016/j.devcel.2009.08.006.

Case, L.B., X. Zhang, J.A. Ditlev, and M.K. Rosen. 2019. Stoichiometry controls activity of phase-separated clusters of actin signaling proteins. *Science*. 363:1093–1097. doi:10.1126/science.aau6313.

Chen, Q., and T.D. Pollard. 2013. Actin filament severing by cofilin dismantles actin patches and produces mother filaments for new patches. *Curr. Biol.* 23:1154–1162. doi:10.1016/j.cub.2013.05.005.

Collins, A., A. Warrington, K. a Taylor, and T. Svitkina. 2011. Structural organization of the actin cytoskeleton at sites of clathrin-mediated endocytosis. *Curr. Biol.* 21:1167–75. doi:10.1016/j.cub.2011.05.048.

Duncan, M.C., M.J. Cope, B.L. Goode, B. Wendland, and D.G. Drubin. 2001. Yeast Eps15-like endocytic protein, Pan1p, activates the Arp2/3 complex. *Nat. Cell Biol.* 3:687–90. doi:10.1038/35083087.

Espinoza-Sanchez, S., L.A. Metskas, S.Z. Chou, E. Rhoades, and T.D. Pollard. 2018. Conformational changes in Arp2/3 complex induced by ATP, WASp-VCA, and actin filaments. *Proc. Natl. Acad. Sci. U. S. A.* 115:E8642–E8651. doi:10.1073/pnas.1717594115.

Feliciano, D., and S.M. Di Pietro. 2012. SLAC, a complex between Sla1 and Las17, regulates actin polymerization during clathrin-mediated endocytosis. *Mol. Biol. Cell*. 23:4256–72. doi:10.1091/mbc.E11-12-1022.

Field, C., and R. Schekman. 1980. Localized secretion of acid phosphatase reflects the pattern of cell surface growth in saccharomyces cerevisiae. *J. Cell Biol.* 86:123–128. doi:10.1083/jcb.86.1.123.

Geli, M.I., and H. Riezman. 1996. Role of Type I Myosins in Receptor-Mediated Endocytosis in Yeast. *Science*. 272:533–535.

Godlee, C., and M. Kaksonen. 2013. From uncertain beginnings: Initiation mechanisms of clathrin-mediated endocytosis. *J. Cell Biol.* 203:717–725. doi:10.1083/jcb.201307100.

Goode, B.L., A.A. Rodal, G. Barnes, and D.G. Drubin. 2001. Activation of the Arp2/3 Complex by the Actin Filament Binding Protein Abp1p. *J. Cell Biol.* 153:627–634. doi:10.1083/jcb.153.3.627.

Grassart, A., A.T. Cheng, S.H. Hong, F. Zhang, N. Zenzer, Y. Feng, D.M. Briner, G.D. Davis, D. Malkov, and D.G. Drubin. 2014. Actin and dynamin2 dynamics and interplay during clathrin-mediated endocytosis. *J. Cell Biol.* 205:721–735. doi:10.1083/jcb.201403041.

Greenberg, M.J., T. Lin, Y.E. Goldman, H. Shuman, and E.M. Ostap. 2012. Myosin IC generates power over a range of loads via a new tension-sensing mechanism. *Proc. Natl. Acad. Sci. U. S. A.* 109:E2433-40. doi:10.1073/pnas.1207811109.

Greenberg, M.J., and E.M. Ostap. 2013. Regulation and control of myosin-I by the motor and light chain-binding domains. *Trends Cell Biol.* 23:81–9. doi:10.1016/j.tcb.2012.10.008.

Hassinger, J.E., G. Oster, D.G. Drubin, and P. Rangamani. 2017. Design principles for robust vesiculation in clathrin-mediated endocytosis. *Proc. Natl. Acad. Sci. U. S. A.* 114:E1118–E1127. doi:10.1073/pnas.1617705114.

Huang, D., H. Friesen, and B. Andrews. 2007. Pho85, a multifunctional cyclin-dependent protein kinase in budding yeast. *Mol. Microbiol.* 66:303–314. doi:10.1111/j.1365-2958.2007.05914.x.

Idrissi, F.-Z., A. Blasco, A. Espinal, and M.I. Geli. 2012. Ultrastructural dynamics of proteins involved in endocytic budding. *Proc. Natl. Acad. Sci. U. S. A.* 109:E2587–E2594. doi:10.1073/pnas.1202789109.

Kaksonen, M., Y. Sun, and D.G. Drubin. 2003. A pathway for association of receptors, adaptors, and actin during endocytic internalization. *Cell*. 115:475–87.

Kaksonen, M., C.P. Toret, and D.G. Drubin. 2005. A modular design for the clathrin- and actin-mediated endocytosis machinery. *Cell*. 123:305–20. doi:10.1016/j.cell.2005.09.024.

Kaksonen, M., C.P. Toret, and D.G. Drubin. 2006. Harnessing actin dynamics for clathrin-mediated endocytosis. *Nat. Rev. Mol. Cell Biol.* 7:404–414. doi:10.1038/nrm1940.

Kishimoto, T., Y. Sun, C. Buser, J. Liu, A. Michelot, and D.G. Drubin. 2011. Determinants of endocytic membrane geometry, stability, and scission. *Proc. Natl. Acad. Sci. U. S. A.* 108:E979-88. doi:10.1073/pnas.1113413108.

Kukulski, W., M. Schorb, M. Kaksonen, and J.A.G. Briggs. 2012. Plasma membrane reshaping during endocytosis is revealed by time-resolved electron tomography. *Cell*. 150:508–520. doi:10.1016/j.cell.2012.05.046.

Laakso, J.M., J.H. Lewis, H. Shuman, and E.M. Ostap. 2008. Myosin I can act as a molecular force sensor. *Science*. 321:133–6. doi:10.1126/science.1159419.

Layton, A.T., N.S. Savage, A.S. Howell, S.Y. Carroll, D.G. Drubin, and D.J. Lew. 2011. Modeling vesicle traffic reveals unexpected consequences for Cdc42p-mediated polarity establishment. *Curr. Biol.* 21:184–194. doi:10.1016/j.cub.2011.01.012.

Lee, S., H.C. Ho, J.M. Tumolo, P.C. Hsu, and J.A. MacGurn. 2019. Methionine triggers Ppz-mediated dephosphorylation of Art1 to promote cargo-specific endocytosis. *J. Cell Biol.* 218:977–992. doi:10.1083/jcb.201712144.

Lewellyn, E.B., R.T.A. Pedersen, J. Hong, R. Lu, M. Huntly, and D.G. Drubin. 2015. An Engineered Minimal WASP-Myosin Fusion Protein Reveals Essential Functions for Endocytosis. *Dev. Cell*. 35:281–294. doi:10.1016/j.devcel.2015.10.007.

Li, P., S. Banjade, H.C. Cheng, S. Kim, B. Chen, L. Guo, M. Llaguno, J. V. Hollingsworth, D.S. King, S.F. Banani, P.S. Russo, Q.X. Jiang, B.T. Nixon, and M.K. Rosen. 2012. Phase transitions in the assembly of multivalent signalling proteins. *Nature*. 483:336–340. doi:10.1038/nature10879.

Liu, J., M. Kaksonen, D.G. Drubin, and G. Oster. 2006. Endocytic vesicle scission by lipid phase boundary forces. *Proc. Natl. Acad. Sci. U. S. A.* 103:10277–10282. doi:10.1073/pnas.0601045103.

Liu, J., Y. Sun, D.G. Drubin, and G.F. Oster. 2009. The mechanochemistry of endocytosis. *PLoS Biol.* 7. doi:10.1371/journal.pbio.1000204.

Lu, R., and D.G. Drubin. 2017. Selection and stabilization of endocytic sites by Ede1, a yeast functional homologue of human Eps15. *Mol. Biol. Cell*. 28:567–575. doi:10.1091/mbc.E16-06-0391.

Lu, R., D.G. Drubin, and Y. Sun. 2016. Clathrin-mediated endocytosis in budding yeast at a glance. *J. Cell Sci.* 129:1531–1536. doi:10.1242/jcs.182303.

Michelot, A., M. Costanzo, A. Sarkeshik, C. Boone, J.R. Yates, and D.G. Drubin. 2010. Reconstitution and protein composition analysis of endocytic actin patches. *Curr. Biol.* 20:1890–1899. doi:10.1016/j.cub.2010.10.016.

Michelot, A., A. Grassart, V. Okreglak, M. Costanzo, C. Boone, and D.G. Drubin. 2013. Actin filament elongation in Arp2/3-derived networks is controlled by three distinct mechanisms. *Dev. Cell*. 24:182–95. doi:10.1016/j.devcel.2012.12.008.

Mund, M., J.A. Van Der Beek, J. Deschamps, S. Dmitrieff, P. Hoess, J.L. Monster, A. Picco, F. Nedelec, M. Kaksonen, and J. Ries. 2018. Systematic Nanoscale Analysis of Endocytosis Links Efficient Vesicle Formation to Patterned Actin Nucleation. *Cell*. 174:884–896. doi:10.1016/j.cell.2018.06.032.

Newpher, T.M., R.P. Smith, V. Lemmon, and S.K. Lemmon. 2005. In vivo dynamics of clathrin and its adaptor-dependent recruitment to the actin-based endocytic machinery in yeast. *Dev. Cell*. 9:87–98. doi:10.1016/j.devcel.2005.04.014.

Okreglak, V., and D.G. Drubin. 2007. Cofilin recruitment and function during actin-mediated endocytosis dictated by actin nucleotide state. *J. Cell Biol.* 178:1251–64. doi:10.1083/jcb.200703092.

Okreglak, V., and D.G. Drubin. 2010. Loss of Aip1 reveals a role in maintaining the actin monomer pool and an in vivo oligomer assembly pathway. *J. Cell Biol.* 188:769–77. doi:10.1083/jcb.200909176.

Palmer, S.E., I.I. Smaczynska-de Rooij, C.J. Marklew, E.G. Allwood, R. Mishra, S. Johnson, M.W. Goldberg, and K.R. Ayscough. 2015. A Dynamin-Actin Interaction Is Required for Vesicle Scission during Endocytosis in Yeast. *Curr. Biol.* 25:868–878. doi:10.1016/j.cub.2015.01.061.

Peng, Y., A. Grassart, R. Lu, C.C.L. Wong, J. Yates, G. Barnes, and D.G. Drubin. 2015. Casein Kinase 1 Promotes Initiation of Clathrin-Mediated Endocytosis. *Dev. Cell*. 32:231–240. doi:10.1016/j.devcel.2014.11.014.

Picco, A., M. Mund, J. Ries, F. Nedelec, and M. Kaksonen. 2015. Visualizing the functional architecture of the endocytic machinery. *Elife*. 1–29. doi:10.7554/eLife.04535.

Rodal, A.A., L. Kozubowski, B.L. Goode, D.G. Drubin, and J.H. Hartwig. 2005a. Actin and Septin Ultrastructures at the Budding Yeast Cell Cortex. *Mol. Biol. Cell*. 16:372–384. doi:10.1091/mbc.E04.

Rodal, A.A., A.L. Manning, B.L. Goode, and D.G. Drubin. 2003. Negative Regulation of Yeast WASp by Two SH3 Domain-Containing Proteins. 13:1000–1008. doi:10.1016/S.

Rodal, A.A., O. Sokolova, D.B. Robins, K.M. Daugherty, S. Hippenmeyer, H. Riezman, N. Grigorieff, and B.L. Goode. 2005b. Conformational changes in the Arp2/3 complex leading to actin nucleation. *Nat. Struct. Mol. Biol.* 12:26–31. doi:10.1038/nsmb870.

Rodnick-Smith, M., Q. Luan, S.-L. Liu, and B.J. Nolen. 2016. Role and structural mechanism of WASP-triggered conformational changes in branched actin filament nucleation by Arp2/3 complex. *Proc. Natl. Acad. Sci. U. S. A.* 201517798. doi:10.1073/PNAS.1517798113.

Roelants, F.M., K.L. Leskoske, R.T.A. Pedersen, A. Muir, J.M.-H. Liu, G.C. Finnigan, and J. Thorner. 2017. TOR Complex 2-regulated protein kinase Fpk1 stimulates endocytosis via inhibition of Ark1/Prk1-related protein kinase Akl1 in Saccharomyces cerevisiae. *Mol. Cell. Biol.* 37:MCB.00627-16. doi:10.1128/MCB.00627-16.

Roux, A., K. Uyhazi, A. Frost, and P. De Camilli. 2006. GTP-dependent twisting of dynamin implicates constriction and tension in membrane fission. *Nature*. 441:528–531. doi:10.1038/nature04718.

Simunovic, M., J.B. Manneville, H.F. Renard, E. Evergren, K. Raghunathan, D. Bhatia, A.K. Kenworthy, G.A. Voth, J. Prost, H.T. McMahon, L. Johannes, P. Bassereau, and A. Callan-Jones. 2017. Friction Mediates Scission of Tubular Membranes Scaffolded by BAR Proteins. *Cell*. 170:172-184.e11. doi:10.1016/j.cell.2017.05.047.

Skruzny, M., T. Brach, R. Ciuffa, S. Rybina, M. Wachsmuth, and M. Kaksonen. 2012. Molecular basis for coupling the plasma membrane to the actin cytoskeleton during clathrin-mediated endocytosis. *Proc. Natl. Acad. Sci. U. S. A.* 109:E2533–E2542. doi:10.1073/pnas.1207011109.

Smaczynska-de Rooij, I.I., E.G. Allwood, S. Aghamohammadzadeh, E.H. Hettema, M.W. Goldberg, and K.R. Ayscough. 2010. A role for the dynamin-like protein Vps1 during endocytosis in yeast. *J. Cell Sci.* 123:3496–3506. doi:10.1242/jcs.070508.

Smaczynska-de Rooij, I.I., E.G. Allwood, R. Mishra, W.I. Booth, S. Aghamohammadzadeh, M.W. Goldberg, and K.R. Ayscough. 2012. Yeast Dynamin Vps1 and Amphiphysin Rvs167 Function Together During Endocytosis. *Traffic*. 13:317–328. doi:10.1111/j.1600-0854.2011.01311.x.

Smaczynska-de Rooij, I.I., C.J. Marklew, S.E. Allwood, W.I. Booth, R. Mishra, M.W. Goldberg, and K.R. Ayscough. 2016. Phosphorylation Regulates the Endocytic Function of the Yeast Dynamin-Related Protein Vps1. *Mol. Cell. Biol.* 36:742–755. doi:10.1128/MCB.00833-15.

Stefan, C.J., S.M. Padilla, A. Audhya, and S.D. Emr. 2005. The Phosphoinositide Phosphatase Sjl2 Is Recruited to Cortical Actin Patches in the Control of Vesicle Formation and Fission during Endocytosis. *Mol. Cell. Biol.* 25:2910–2923. doi:10.1128/mcb.25.8.2910-2923.2005.

Stimpson, H.E.M., C.P. Toret, A.T. Cheng, B.S. Pauly, and D.G. Drubin. 2009. Early-Arriving Syp1p and Ede1p Function in Endocytic Site Placement and Formation in Budding Yeast. *Mol. Biol. Cell*. 20:4640–4651. doi:10.1091/mbc.E09.

Sun, Y., S. Carroll, M. Kaksonen, J.Y. Toshima, and D.G. Drubin. 2007. PtdIns(4,5)P2 turnover is required for multiple stages during clathrin- and actin-dependent endocytic internalization. *J. Cell Biol.* 177:355–67. doi:10.1083/jcb.200611011.

Sun, Y., and D.G. Drubin. 2012. The functions of anionic phospholipids during clathrin-mediated endocytosis site initiation and vesicle formation. *J. Cell Sci.* doi:10.1242/jcs.115741.

Sun, Y., N.T. Leong, T. Jiang, A. Tangara, X. Darzacq, and D.G. Drubin. 2017. Switch-like Arp2/3 activation upon WASP and WIP recruitment to an apparent threshold level by multivalent linker proteins in vivo. *Elife*. 6:1–25. doi:10.7554/elife.29140.

Sun, Y., A.C. Martin, and D.G. Drubin. 2006. Endocytic Internalization in Budding Yeast Requires Coordinated Actin Nucleation and Myosin Motor Activity. *Dev. Cell*. 11:33–46. doi:10.1016/j.devcel.2006.05.008.

Toret, C.P., L. Lee, M. Sekiya-Kawasaki, and D.G. Drubin. 2008. Multiple pathways regulate endocytic coat disassembly in Saccharomyces cerevisiae for optimal downstream trafficking. *Traffic*. 9:848–859. doi:10.1111/j.1600-0854.2008.00726.x.

Toshima, J.Y., J. Toshima, M. Kaksonen, A.C. Martin, D.S. King, and D.G. Drubin. 2006. Spatial dynamics of receptor-mediated endocytic trafficking in budding yeast revealed by using fluorescent alpha-factor derivatives. *Proc. Natl. Acad. Sci. U. S. A.* 103:5793–8. doi:10.1073/pnas.0601042103.

Wagner, A.R., Q. Luan, S.-L. Liu, and B.J. Nolen. 2013. Dip1 Defines a Class of Arp2/3 Complex Activators that Function without Preformed Actin Filaments. *Curr. Biol.* 23:1990–8. doi:10.1016/j.cub.2013.08.029.

Weinberg, J.S., and D.G. Drubin. 2014. Regulation of Clathrin-mediated endocytosis by dynamic ubiquitination and deubiquitination. *Curr. Biol.* 24:951–959. doi:10.1016/j.cub.2014.03.038.

Winter, D., T. Lechler, and R. Li. 1999. Activation of the yeast Arp2/3 complex by Bee1p, a WASP-family protein. *Curr. Biol.* 9:501–505. doi:10.1016/S0960-9822(99)80218-8.

Winter, D., a V Podtelejnikov, M. Mann, and R. Li. 1997. The complex containing actin-related proteins Arp2 and Arp3 is required for the motility and integrity of yeast actin patches. *Curr. Biol.* 7:519–29.

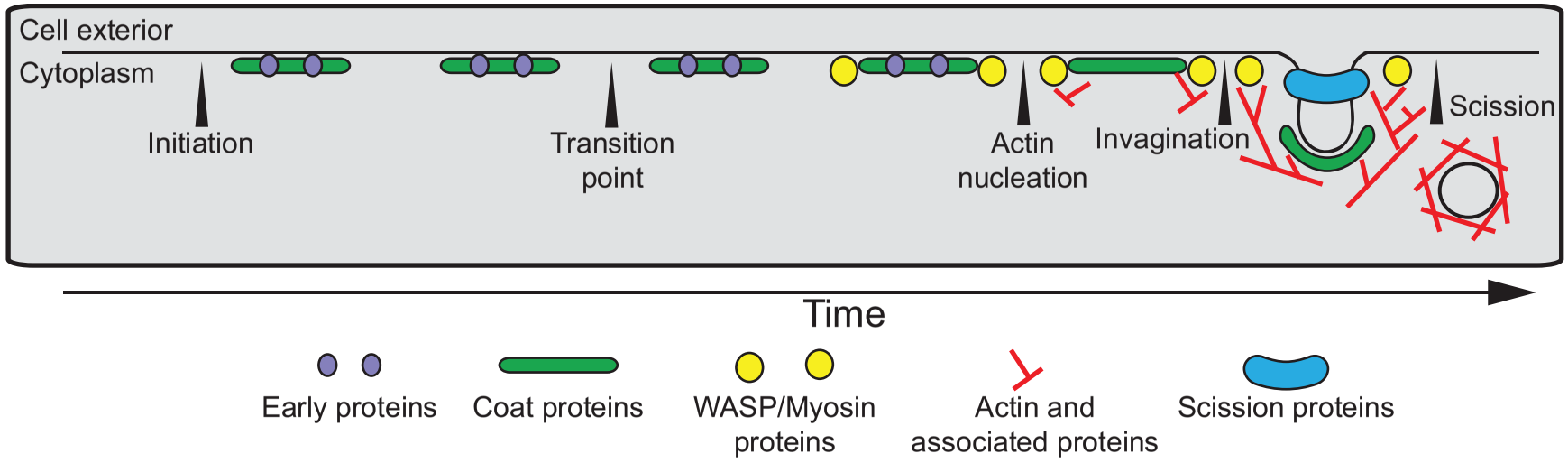
Cell exterior
Cytoplasm
Initiation
Transition point
Actin nucleation
Invagination
Scission
Time
Early proteins
Coat proteins
WASP/Myosin proteins
Actin and associated proteins
Scission proteins

Figure 1.1: Timeline of progression through the clathrin-mediated endocytic pathway in budding yeast

Clathrin-mediated endocytosis initiates when proteins of the early and early coat module (purple circles and green ovals, respectively) select a site for internalization on the inner leaflet of the plasma membrane. This coat matures through a regulatory transition point and recruits proteins of the WASP/Myosin module (yellow circles). The WASP/Myosin module triggers a burst of actin assembly, also recruiting a host of proteins in the actin module (red lines). Actin assembly provides force to invaginate the membrane into a deep pit that is resolved by proteins of the scission module (blue collar).

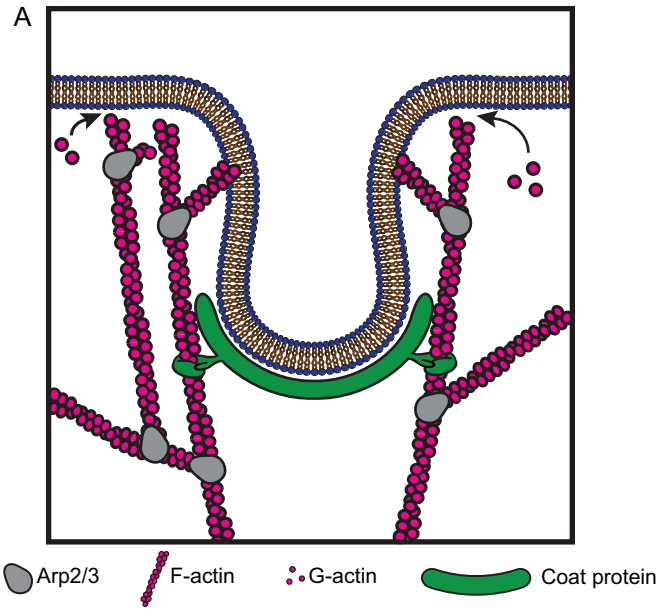
A
Arp2/3
F-actin
G-actin
Coat protein

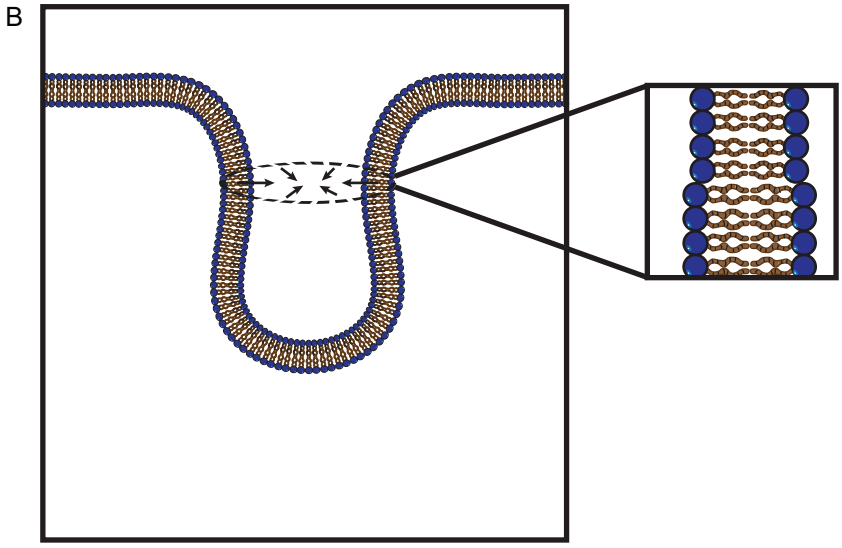
B

Figure 1.2: Mechanisms of force generation during clathrin-mediated endocytosis

(A) Proposed model of actin assembly-based force generation during membrane invagination. New monomers (magenta circles) are added to Arp2/3 (grey avocados) actin networks near the plasma membrane. Actin filaments are linked to the tip of the growing invagination by coat proteins (green mittens). This assembly results in a force that drives deeper membrane invagination. (B) Proposed model of endocytic scission by line tension. Segregation of subsets of phospholipids along the endocytic invagination generates a phase boundary that is thermodynamically unfavorable. An example of such a phase boundary is shown in the inset, where the phospholipids display hydrophobic mismatch. Minimization of the area occupied by such a phase boundary results in a pinching (arrows).

Chapter 2 : Type I myosins anchor actin assembly to the plasma membrane during clathrin-mediated endocytosis

Reproduced from: Pedersen RTA and Drubin DG. 2019. Type I myosins anchor actin assembly to the plasma membrane during clathrin-mediated endocytosis. *J. Cell Biol.* 218: 1138-1147.

Abstract

The actin cytoskeleton generates forces on membranes for a wide range of cellular and subcellular morphogenic events, from cell migration to cytokinesis and membrane trafficking. For each of these processes, filamentous actin (F-actin) interacts with membranes and exerts force through its assembly, its associated myosin motors, or both. These two modes of force generation are well-studied in isolation, but how they are coordinated in cells is mysterious. During clathrin-mediated endocytosis, F-actin assembly initiated by the Arp2/3 complex and several proteins that compose the WASP/Myosin complex generates the force necessary to deform the plasma membrane into a pit. Here I present evidence that type I myosin is the key membrane anchor for endocytic actin assembly factors in budding yeast. By mooring actin assembly factors to the plasma membrane, this myosin organizes endocytic actin networks and couples actin-generated forces to the plasma membrane to drive invagination and scission. Through this unexpected mechanism myosin facilitates force generation independent of its motor activity.

Introduction

Clathrin-mediated endocytosis (CME) is a highly conserved cellular process for internalizing soluble and membrane-associated cargos into nascent vesicles derived from the plasma membrane (PM). During the final stages of CME the PM is bent into a deep pit that constricts at its neck and then undergoes scission. Clathrin and associated adaptor proteins are able to deform the PM when it is under low tension; however, force from the actin cytoskeleton is needed to bend the PM when it is under high tension in mammalian cells (Batchelder and Yarar, 2010; Boulant et al., 2011) or pressed against a cell wall by turgor pressure in fungal cells (Aghamohammadzadeh and Ayscough, 2009). Growing evidence indicates that actin assembly usually occurs during the final stages of CME, even in situations where F-actin is not required (Grassart et al., 2014).

Assembly of an Arp2/3 complex-derived actin network at endocytic sites generates force for PM deformation during CME, but experiments in live cells indicate that type I myosins are also required for force-generation (Sun et al., 2006, Lewellyn et al. 2015). In the actin assembly-based force generation model, new monomers join endocytic actin networks near the PM, pushing F-actin in the network deeper into the cytoplasm (Kaksonen et al., 2003, 2005; Picco et al., 2015). F-actin is attached to the apex of endocytic pits by adaptor proteins, so this inward movement of the actin network drags the tip of the growing membrane invagination inwards and facilitates transition from a U-shaped pit to an omega-shaped pit (Skruzny et al., 2012; Hassinger et al., 2017). Reconstitution experiments indicate that growth of endocytic actin networks is sufficient to generate force: beads coated with the endocytic Arp2/3 complex activator from *Saccharomyces cerevisiae*, the Wiscott-Aldrich Syndrome Protein (WASP) homologue Las17, assemble actin tails and are motile in budding yeast cytoplasmic lysates or in the presence of actin, Arp2/3 complex, and capping protein (Michelot et al., 2010). However, budding yeast cells harboring mutations in the genes encoding type I myosins assemble robust endocytic actin networks but fail to internalize vesicles by CME (Sun et al., 2006). These data demonstrate that both actin assembly and type I myosin activity are required for CME *in vivo.*

The Arp2/3 complex is activated at the base of endocytic sites (near the PM) by nucleation promoting factors (NPFs). In budding yeast, the principal NPFs, Las17 and the type I myosins Myo5 and Myo3, exist in a complex termed the WASP/Myosin complex that stays at the base of the endocytic site while the coat internalizes (Kaksonen et al., 2005). This complex also includes the homologues of WASP interacting protein (Vrp1) and the F-BAR protein Toca-1 (Bzz1) along with the NPF regulator Bbc1 (Soulard et al., 2002). Previously, we distilled this complex down to a single engineered Myo5-Las17 fusion protein with non-essential domains deleted to reveal the minimal activities of the WASP/Myosin complex required to build an actin cytoskeleton capable of generating force for CME. Our fusion protein revealed that the following domains are sufficient to support CME even in the absence of all other members of the WASP/Myosin complex: (1) a domain for recruitment to endocytic sites, (2) an NPF domain to activate the Arp2/3 complex, (3) a functional myosin motor domain, and (4) a membrane binding domain from Myo5 (Lewellyn et al., 2015). However, the mechanistic contributions of the activities provided by Myo5 in our minimal fusion protein were unclear.

To determine the mechanistic contributions of membrane binding by Myo5 during CME, I engineered budding yeast strains lacking membrane-bound Myo5. My results reveal

that Myo5 serves as the key membrane anchor for the actin assembly factors of the WASP/Myosin complex.

Results and discussion

To investigate how type I myosin membrane binding contributes to CME, I made *Saccharomyces cerevisiae* strains with *MYO5* genes encoding mutant proteins linked to a carboxy-terminal (C-terminal) 13Myc tag for immunoblotting to ensure that the mutant alleles were expressed (Fig. 2.2A). I examined CME phenotypes using live-cell imaging of Sla1-GFP as a marker for the endocytic coat and Abp1-mRFP as a marker for endocytic actin networks. Because Myo3 and Myo5 are redundant under laboratory conditions (Goodson et al., 1996), I used a background with the *MYO3* gene deleted throughout my study. When I deleted *MYO5* completely or replaced it with a mutant lacking the membrane-binding Tail homology 1 (TH1) domain (Feeser et al., 2010; Fernández-Golbano et al., 2014), CME was severely defective. While F-actin still assembled at endocytic sites, the sites turned over slowly and became depolarized (Fig. 2.1A), puncta of Sla1-GFP failed to move off of the PM (Fig. 2.1B-C), and lifetimes of Sla1-GFP and Abp1-mRFP at endocytic sites were extended in comparison to wild-type *MYO5* cells (Fig. 2.2B). Surprisingly, rather than being restricted to endocytic sites, endocytic actin networks marked by Abp1-mRFP frequently formed motile comets deep in the cytoplasm (Fig. 2.1A and 2.1D, Lewellyn *et al.* 2015). These observations suggest that actin assembly can become uncoupled from endocytic sites in mutants lacking membrane-bound Myo5.

All observed mutant cells lacking membrane-bound Myo5 had negligible rates of endocytic vesicle internalization (Fig. 2.1C), but not all cells had cytoplasmic actin comets in epifluorescence movies (Fig. 2.1D). To resolve this discrepancy, I imaged my mutants lacking membrane-binding competent Myo5 using total internal reflection fluorescence microscopy (TIRFM), reasoning that actin comets could be an exaggerated manifestation of a more penetrant actin assembly phenotype occurring close to the PM. In wild-type *MYO5* cells, TIRFM movies revealed discrete actin assembly events at each Sla1-GFP-marked endocytic site after 16 ± 4 s (n = 60 sites, mean ± SD), even in situations where multiple sites were clustered together. In *myo5Δ* and *myo5-TH1Δ* cells, however, actin assembly initiated at individual endocytic sites after 20 ± 7 s (n = 85 and 50 sites, p = 0.0001 and 0.0022 respectively, compared to *MYO5* by one-way ANOVA (F = 9.509) followed by Dunnett's test) and then spread as a wave in the plane of the PM, frequently engulfing neighboring endocytic sites (Fig. 2.1E and 2.1F, Fig. 2.2C and 2.2D). This phenomenon was evident in every cell examined; thus, delocalized actin assembly is a fully penetrant phenotype. Together, these data indicate that Myo5 restricts actin assembly to endocytic sites.

The Arp2/3 complex nucleates actin assembly during CME, so aberrant actin assembly in *myo5* mutants suggests that membrane binding by Myo5 may restrict actin assembly to endocytic sites through localizing Arp2/3 complex activity. To determine whether the Arp2/3 complex becomes mislocalized in *myo5* mutants deficient in membrane-binding, I visualized the complex by creating an in-frame GFP fusion of *ARC15*, which encodes the *S. cerevisiae* homologue of the Arp2/3 complex subunit ARPC5, at its endogenous genomic locus. In wild-type *MYO5* cells, the Arp2/3 complex localized exclusively to Abp1-mRFP patches at the cell cortex, but in *myo5Δ* cells or cells expressing the myo5-TH1Δ membrane-binding mutant, 99±2% (*myo5Δ*) and 100% (*myo5-TH1Δ*) of cytoplasmic Abp1-mRFP-labeled actin comets colocalized with the Arp2/3 complex (Fig.

2.3A). To test whether the mislocalized Arp2/3 complex was active, I treated cells with CK-666, a reversible small molecule inhibitor of the Arp2/3 complex (Nolen et al., 2009), or with an equivalent control concentration of DMSO (Fig. 2.2E and 2.2F). Addition of CK-666 to cells containing cytoplasmic actin comets caused rapid dissolution of the cytoplasmic actin structures (Fig. 2.3B), and drastically reduced the percentage of cells with visible comets (Fig. 2.3C). These results show that Myo5 constrains Arp2/3 complex activity to endocytic sites.

The observed mislocalization of active Arp2/3 complex suggested that membrane binding by Myo5 retains Arp2/3 complex activators (NPFs) at endocytic sites. The *S. cerevisiae* genome encodes four NPFs. The primary NPF activities are contained within the WASP/Myosin complex and comprise (1) Las17 and (2) Vrp1 working in cooperation with Myo3 or Myo5. These factors remain at the base of CME sites during membrane invagination (Sun et al., 2006; Kaksonen et al., 2005). Abp1 and the budding yeast intersectin homologue Pan1 have also been reported to have NPF activity, but these activities are not essential for CME (Sun et al., 2006; Goode et al., 2001; Duncan et al., 2001). To test whether the WASP/Myosin complex is restricted to endocytic sites by Myo5, I localized each member of the complex by epifluorescence microscopy. While all members of the WASP/myosin complex (Las17, Vrp1, Bbc1, and Bzz1) localized to cortical CME sites in wild-type *MYO5* cells, they were found at the tips of the cytoplasmic actin comets in *myo5-TH1Δ* cells. Conversely, Pan1 localized exclusively to the cell cortex in both wild-type *MYO5* and *myo5-TH1Δ* cells (Fig. 2.3D). The myo5-TH1Δ protein itself similarly localized to the tips of the cytoplasmic actin comets (Fig. 2.2G, Lewellyn et al., 2015). The relocalization of the WASP/Myosin complex in the absence of membrane binding by Myo5 indicates that Myo5 restricts actin assembly to endocytic sites by constraining the location of Arp2/3 complex activation.

Membrane binding by Myo5 could be important for restricting Arp2/3 complex activation to sites of CME either by physically linking the WASP/Myosin complex to the PM at CME sites, by preventing continued WASP/Myosin complex activity after vesicle internalization, or by preventing aggregation of WASP/Myosin complex proteins in the cytoplasm. Knowing the origin of actin comets in *myo5* mutants would help to distinguish between these models. I suspected that actin comets represented actin internalized from endocytic sites without coincident vesicle internalization for several reasons. First, I repeatedly observed comets that appeared to pull away from the PM in epifluorescence movies (Fig. 2.4A). Second, actin waves originated at CME sites in TIRFM movies (Fig. 2.1E, Fig. 2.2C). Finally, Sla1-GFP labeled patches failed to move off the PM in Myo5 mutants (Fig. 2.1C), making it unlikely that the actin comets represented internalized vesicles that failed to disassemble the WASP/Myosin complex. Pulse-chase experiments with the membrane dye FM4-64 supported this conclusion by revealing that *myo5* mutants internalized very small amounts of dye (Fig. 2.4B and 2.4C). While the trace amount of dye internalized in *myo5* mutants is similar to the amount internalized in CME-defective *sla2Δ* cells (Peng et al., 2015), I cannot exclude the possibility that small amounts of membrane internalize in these mutants. Because actin comets appear to originate at the PM in *myo5* mutants, and these same mutants fail to internalize membrane by CME, I conclude that Myo5 plays the role of anchoring the WASP/Myosin complex to the PM at endocytic sites.

To directly visualize the role of Myo5 as a membrane anchor for the WASP/Myosin complex, I performed CK-666 washout experiments. I pre-treated cells with CK-666 to synchronize CME events, stalling them at the stage prior to actin assembly. I then added media to dilute the CK-666 below its effective concentration and observed growth of endocytic actin networks by epifluorescence microscopy. In wild-type *MYO5* cells, actin assembly following CK-666 washout coincided with internalization of Sla1-GFP patches (Fig. 2.4D, Fig. 2.5A and 2.5B). In mutant cells deficient for membrane-bound Myo5, actin still assembled at endocytic sites following CK-666 washout, but Sla1-GFP patches failed to move off the PM. Sla1-GFP signal decreased coincident with actin assembly, likely reflecting recruitment of endocytic disassembly factors by F-actin (Toret et al., 2008). Strikingly, flares of Abp1-mRFP signal were frequently observed to separate from endocytic sites and internalize (Fig. 2.4D, Fig. 2.5A and 2.5B). These flares moved off the PM with an average velocity of 240 ± 80 nm/s, similar to the reported speed of Abp1 patches after vesicle scission in wild-type cells of 230 nm/s (Fig. 2.5C)(Kaksonen et al., 2003). A one-sample t-test comparing the measured actin flare velocities to the known value of 230 nm/s yielded a p value of 0.55, supporting the hypothesis that these two actin structures move similarly. These data strongly suggest that the observed flares represent actin internalization uncoupled from membrane internalization. Neither Abp1-mRFP nor Sla1-GFP signal internalized in control or mutant cells without CK-666 washout (Fig. 2.4D). When I performed CK-666 washout experiments on cells expressing the WASP/Myosin complex protein Vrp1-GFP, I once again observed actin flares peeling off the plasma membrane (Fig. 2.4E). However, unlike Sla1-GFP, which remained on the plasma membrane (Fig. 2.4D), Vrp1-GFP puncta occasionally splintered perceptibly, with a subset of the protein internalizing with the Abp1-mRFP-labeled actin flare (Fig. 2.4E). This behavior contrasts starkly with the behavior of Vrp1 puncta in wild-type *MYO5* cells, which remain on the PM during CME (Fig. 2.4E, Kaksonen et al., 2005). Thus Myo5 membrane binding is crucial for coupling actin assembly to vesicle internalization through anchorage of the WASP/Myosin complex to the PM at endocytic sites.

Thus far, I have revealed a novel function for Myo5 in anchoring actin assembly to the PM during CME. While I have observed uncoupling of actin assembly from endocytic sites upon deletion of the membrane-binding domain of Myo5, I have not identified the other end of this crucial linkage: how Myo5 contacts actin assembly factors to anchor them. To elucidate this end of the Myo5 membrane-actin linkage, I scored cytoplasmic actin comet formation in strains harboring a series of *myo5* alleles encoding domain-deleted versions of the protein, each linked to a C-terminal 13Myc tag for immunoblotting to ensure that the mutant alleles were expressed (Fig. 2.6A, Fig. 2.7A). While deletion of the membrane-binding TH1 domain caused formation of actin comets, no other individual domain truncation elicited this phenotype (Fig. 2.1D, Fig. 2.6B-C, Lewellyn et al., 2015). Because Myo5 motor activity itself is crucial for CME (Sun et al., 2006; Idrissi et al., 2012; Lewellyn et al., 2015), I reasoned that Myo5 may be redundantly linked to the actin cytoskeleton through binding of its motor domain to F-actin and one of its other domains to actin assembly factors in the WASP/Myosin complex. To identify these domains, I made *myo5* alleles encoding proteins with pairwise deletions, combining motor domain deletion with deletion of the F-actin-binding Tail homology 2 (TH2) domain (Geli et al., 2000), the poly-proline domain-binding Src homology 3 (SH3) domain, and the Arp2/3 complex-binding Connector/acidic (CA) domain. Both *myo5-motorΔ TH2Δ* and *myo5-motorΔ SH3Δ*

cells contained cytoplasmic actin comets (Fig. 2.6B and 2.6D), indicating that Myo5 is linked to the endocytic actin cytoskeleton through both its motor domain and domains in the non-motor tail of the protein.

Myo5 is normally recruited to endocytic sites and bound into the WASP/Myosin complex by its SH3 domain, with possible contributions from the TH2 domain (Sun et al., 2006; MacQuarrie et al., 2018 *Preprint*). Because the entire WASP/Myosin complex becomes uncoupled from endocytic sites in *myo5* membrane-binding mutants (Fig. 2.3D) and *myo5* motor mutants unable to bind the other WASP/Myosin proteins, I concluded that Myo5 exerts its actin-membrane bridging function by directly anchoring the WASP/Myosin complex to the PM. To test whether Myo5 is the membrane anchor for the WASP/Myosin complex, I expressed versions of each myo5 truncation that formed comets fused via a flexible peptide linker to Vrp1, a WASP/Myosin complex protein that normally binds to Myo5. If Myo5 is the membrane anchor for the WASP/Myosin complex, I reasoned that this linkage might eliminate actin comet formation in *myo5* truncation mutants that fail to bind to the WASP/Myosin proteins but not in mutants that fail to bind to the PM. Vrp1 linkage to myo5-TH1Δ failed to rescue the cytoplasmic actin comet phenotype, but the linkage did rescue comet formation for myo5-motorΔ TH2Δ and the myo5-motorΔ SH3Δ mutant proteins (Fig. 2.6E), supporting the conclusion that Myo5 binds to and anchors other WASP/Myosin complex components to the PM. Internalization of Sla1-GFP patches and lifetimes of Sla1-GFP and Abp1-mRFP patches were not rescued in these mutants, confirming the essential role of the Myo5 motor domain in CME (Fig. 2.7B and 2.7C). A detailed characterization of the contribution of Myo5 motor activity to CME will be the subject of a future study. Nevertheless, *myo5* mutants that did not exhibit comets were healthier than mutants that did exhibit comets, as illustrated by restored growth of the cells at high temperatures, indicating that cytoplasmic actin comets represent a bona fide pathology on the cellular level (Fig. 2.6F). My data demonstrate that Myo5 anchors assembling actin networks to the PM at endocytic sites redundantly through its motor and tail domains (Fig. 2.6G).

A recent study demonstrated that the WASP/Myosin complex is recruited to endocytic sites as a ring around the presumptive invagination site in the plane of the PM and that this symmetrical organization of Arp2/3 complex activators results in optimal force generation by actin assembly (Mund et al., 2018). My results indicate that Myo5 is anchors Arp2/3 complex activators to CME sites, most likely through direct membrane-binding, and that this linkage is crucial for maintaining their ordered localization. This organization restricts actin nucleation to discrete areas on the PM, resulting in an ordered actin network that can generate force (Fig. 2.8A)(Mund et al., 2018). Absent membrane anchoring, Arp2/3 complex activation and subsequent actin nucleation can occur throughout the actin network, leading to disordered networks that fail to generate force to bend the membrane and, in the most catastrophic circumstances, pull away from the membrane completely (Fig. 2.8B). This model differs from a previous interpretation where we proposed that Myo5 links actin filaments themselves to the PM at endocytic sites (Lewellyn *et al.* 2015). Interestingly, a requirement for a membrane anchor for NPFs has also been reported in engineered motile systems, and absence of the linkage causes a qualitatively similar phenotype to what I observed, with actin tails separating from their initial substrate (Co et al., 2007).

PM-anchoring of actin assembly factors by Myo5 is a novel, conserved membrane-actin linkage at endocytic sites, adding to our understanding of the CME actin machinery. Previous studies have described how endocytic coat components recruit actin assembly factors to endocytic sites (Sun et al., 2015), and how movement of F-actin into the cytoplasm is coupled to inward movement of the endocytic coat (Skruzny et al., 2012). My experiments reveal the mechanism by which actin assembly factors are anchored to the PM during actin assembly. Interestingly, the human homologue of Myo5, Myosin 1e, also interacts with a variety of endocytic proteins through its tail domains (Krendel et al., 2007), and mislocalization of Myosin 1e in human cells also leads to misocalization of Arp2/3 complex activators (Cheng et al., 2012). These observations suggest that membrane anchoring of WASP family proteins is a conserved function of type I myosins.

It is particularly intriguing that unmooring of the actin assembly machinery from endocytic sites results in waves of actin assembly that spread across the PM (Fig. 2.1E-F, fig. 2.2C). Similar waves of assembling F-actin manifest in diverse systems ranging from immune cells to oocytes and embryos (Inagaki and Katsuno, 2017; Weiner et al., 2007; Bement et al., 2015), and are usually generated by activator-inhibitor-coupled systems, where actin assembly leads to the delayed recruitment of an inhibitor of actin assembly (Allard and Mogilner, 2013). Indeed, F-actin itself indirectly recruits disassembly factors to endocytic sites (Toret et al., 2008), and negative feedback of F-actin on Arp2/3 regulators partially accounts for the transient assembly and disassembly of the actin machinery at endocytic sites (Wang et al., 2016). My data substantiate the existence of such feedback relationships in clathrin-mediated endocytosis by demonstrating that spatially uncoupling the actin assembly machinery (the WASP/Myosin complex) from the endocytic disassembly factors (recruited by F-actin) results in traveling waves characteristic of activator-inhibitor-coupled systems.

Type I myosins are pervasive components of actin machinery involved in membrane trafficking events (Almeida et al., 2011; Sokac et al., 2006). Here I have shown that anchoring actin to the PM is a principle role of type I myosin during CME. It is now important to determine whether type I myosins serve a similar mechanistic role during other membrane trafficking processes.

Methods

Strains and Plasmids

All budding yeast strains were derived from the wild-type diploid DDY1102 and propagated using standard techniques (Amberg et al., 2005). Mutant strains were constructed using plasmid DNA encoding *URA3*-marked *MYO5* variants flanked by the *MYO5* 5' and 3' untranslated regions as templates for genomic integration in diploids that were *MYO5/myo5Δ::HygMX6*. Integration of the full-length mutant allele was ensured by cross selection for acquisition of uracil prototrophy and loss of hygromycin resistance. C-terminal GFP fusions and C-terminal 13Myc fusions and truncations were constructed as described previously (Longtine et al., 1998). All strains were verified by PCR and immunoblotting. For growth comparisons, mid log phase starter cultures were diluted to an OD_{600} of 0.1, 0.02, and 0.004, spotted on plates, and grown for 48 hours at 25º C and 37º C. The strains used in this study are listed in table 2.1. Plasmids used for genomic integration are listed in table 2.2.

Live cell imaging

Cells were grown to mid log phase in imaging media (synthetic minimal media supplemented with Adenine, L-Histidine, L-Lucine, L-Lysine, L-Methionine, Uracil, and 2% glucose), then adhered to coverslips coated with 0.2 mg/ml Concanavalin A.

Epifluorescence imaging was carried out on a Nikon Eclipse Ti inverted microscope with a Nikon 100x 1.4 numerical aperture (NA) Plan Apo VC oil immersion objective and an Andor Neo 5.5 sCMOS camera. GFP and mRFP fluorescence were excited using a Lumencore Spectra X LED light source with 550/15 nm and 470/22 nm excitation filters. For two-color imaging, channels were acquired sequentially using an FF-493/574-Di01 dual pass dichroic mirror and FF01-512/630-25 dual pass emission filters (Semrock, Rochester, NY). The system was controlled with either Metamorph or Nikon Elements software and maintained at 25°C by an environmental chamber (In Vivo Scientific, St. Louis, MO). Frames were separated by either 2 s or 1.15 s depending on the software used.

TIRFM imaging was carried out on a Nikon Eclipse Ti2 inverted microscope with a Nikon CFI60 60x 1.49 NA Apo oil immersion TIRF objective and a Hamamatsu Orca-Flash 4.0 V2 sCMOS camera. GFP and mRFP fluorescence were excited using 488 nm and 561 nm lasers and detected using a Chroma HC TIRF Quad Dichroic (C-FL TIRF Ultra Hi S/N 405/488/561/638) and Chroma HC Quad emission filters BP 525/50 and BP600/50, respectively (Bellows Falls, VT). Channels were acquired sequentially. The system was controlled with Nikon Elements software and maintained at 25°C by an OkoLab environmental chamber (Burlingame, CA). Frames were separated by 1 s.

All image analysis was carried out using Fiji software (NIH). For quantification of Sla1-GFP internalization and Sla1-GFP/Abp1-mRFP patch lifetimes, 10 radial kymographs were generated at random for each cell, measured, and judged as "internalized" if the Sla1-GFP patch moved at least 3 pixels (194 nm) towards the cell interior. The Manual Tracking Fiji plugin was used for particle tracking in Fig. 2.5C. For figure panels and movies,

individual cells were cropped, background fluorescence was uniformly subtracted from the image stack, and photo bleaching was corrected using a custom Fiji macro. Look up tables used for display are linear and cover the full range of data. Figures were assembled in Adobe Illustrator CS6.

CK-666 experiments

CK-666 (≥ 98% pure) was purchased from Sigma Life Sciences (St. Louis, MO), resuspended in DMSO, and used at 250 μM (Fig. 2.2E). All CK-666 experiments were conducted in epifluorescence. For wash-in experiments, cells were adhered to a coverslip as described above and submerged in 500 μL imaging media. After 10-20 frames of imaging, 500 μL of 500 μM CK-666 was added to the cells. To score actin comets across a population of cells treated with CK-666 (Fig. 2C), cells were pre-treated with 250 μM CK-666 for 10 minutes prior to imaging. For CK-666 washout experiments, cells were adhered to coverslips and submerged in 250 μL imaging media with 250-500 μM CK-666. After 10-20 frames of imaging, 4mL of fresh imaging media was added to the cells, diluting CK-666 to ≤29 μM, well below the effective concentration (Fig. 2.2E).

FM4-64 pulse-chase experiments

Cells were immobilized on coverslips, quickly equilibrated with a single wash of imaging media with 10 μg/mL FM4-64 (Molecular probes, Eugene, OR), and then incubated in imaging media with 10 μg/mL FM4-64 for 5 minutes at room temperature. Coverslips were then washed vigorously with fresh imaging media to eliminate excess FM4-64. Coverslips were photographed immediately to identify cells that stained brightly with FM4-64 at a zero time-point, these cells were interpreted to be dead or to have compromised plasma membrane permeability and were eliminated from analysis. Coverslips were then photographed a second time after a 5-minute chase.

Images were collected on a Nikon Eclipse Ti inverted microscope with a Nikon 100x 1.45 NA Plan Apo λ oil immersion objective, an Andor IXon X3 EM-CCD camera and Andor CSU-X spinning disc confocal equipment. FM4-64 fluorescence was excited using a 488 nm laser and detected with a Chroma 605/52 nm emission filter (Bellows Falls, VT). The system was controlled with Nikon Elements software. Imaging was conducted at room temperature (~23°C). The fraction of FM4-64 internalized was determined by dividing the total integrated signal of FM4-64 signal inside of the obvious plasma membrane by the total integrated FM4-64 signal of the cell.

Western Blotting

Cells were grown to mid log phase in rich media (20 g/L bacto-peptone, 10 g/L bacto-yeast extract, 2% glucose), harvested by centrifugation, washed with water, and lysed by bead beating in a lysis buffer with 5 mM Tris-HCl pH 8, 5 mM EDTA pH 8, and 15%

Trichloroacetic acid (TCA). The TCA precipitate was then washed with ice-cold acetone and resuspended in tris/urea sample buffer (62.5 mM tris pH 6.8, 3 M urea, 1% sodium dodecyl sulfate, 5% beta mercaptoethanol, 0.05% bromophenol blue). Extracts were separated electrophoretically on 8% polyacrylamide gels and transferred to nitrocellulose. Membranes were blocked with 5% milk, probed with mouse monoclonal antibody clone 9E10 against a 13-myc tag (prepared from hybridoma supernatant (Lewellyn et al., 2015)) and mouse monoclonal anti-Pgk1 (459250; Novex, Winston-Salem, NC), and then incubated with secondary antibodies conjugated to infrared fluorophores (Li-Cor Biosciences inc., Lincoln, NE). Bands were visualized using an Odyssey infrared imaging system (Li-Cor Biosciences).

Statistics and Reproducibility of experiments

All experimental results presented were replicated in at least three distinct experiments to ensure reproducibility. For imaging experiments, multiple cells from each replicate were analyzed. As data from different days were indistinguishable, they were pooled for statistical analysis. The specific number of cells analyzed is indicated in each figure legend. Statistical analysis was conducted in Prism 7.0 (GraphPad Software, San Diego, CA). Data distribution was assumed to be normal but this was not formally tested. All raw data are available upon reasonable request.

Acknowledgements

I thank J. Hassinger, D. Serwas, and M. Welch for critically evaluating the manuscript along with M. Akamatsu and members of the Drubin/Barnes lab for constant informal input. Spinning disc confocal microscopy was conducted at the University of California, Berkeley Cancer Research Laboratory Molecular Imaging center, supported by the Gordon and Betty Moore foundation. I would like to thank H. Aaron and F. Ives for their microscopy training and assistance. This work was supported by the National Institutes of Health grant R35GM118149 to D.G.D. The authors declare no competing financial interests.

References

Aghamohammadzadeh, S., and K.R. Ayscough. 2009. Differential requirements for actin during yeast and mammalian endocytosis. *Nat. Cell Biol.* 11:1039–1042. doi:10.1038/ncb1918.

Allard, J., and A. Mogilner. 2013. Traveling waves in actin dynamics and cell motility. *Curr. Opin. Cell Biol.* 25:1–9. doi:10.1016/j.ceb.2012.08.012.

Almeida, C.G., A. Yamada, D. Tenza, D. Louvard, G. Raposo, and E. Coudrier. 2011. Myosin 1b promotes the formation of post-Golgi carriers by regulating actin assembly and membrane remodelling at the trans-Golgi network. *Nat. Cell Biol.* 13:779–789. doi:10.1038/ncb2262.

Amberg, D.C., D.J. Burke, and J.N. Strathern. 2005. Methods in Yeast Genetics: A Cold Spring Harbor Laboratory Course Manual, 2005 Edition. 205 pp.

Batchelder, E.M., and D. Yarar. 2010. Differential Requirements for Clathrin-dependent Endocytosis at Sites of Cell–Substrate Adhesion. *Mol. Biol. Cell*. 21:3070–3079. doi:10.1091/mbc.E09.

Bement, W.M., M. Leda, A.M. Moe, A.M. Kita, M.E. Larson, A.E. Golding, C. Pfeuti, K.-C. Su, A.L. Miller, A.B. Goryachev, and G. von Dassow. 2015. Activator–inhibitor coupling between Rho signalling and actin assembly makes the cell cortex an excitable medium. *Nat. Cell Biol.* 17:1471–1483. doi:10.1038/ncb3251.

Boulant, S., C. Kural, J.-C. Zeeh, F. Ubelmann, and T. Kirchhausen. 2011. Actin dynamics counteract membrane tension during clathrin-mediated endocytosis. *Nat. Cell Biol.* 13:1124–31. doi:10.1038/ncb2307.

Cheng, J., A. Grassart, and D.G. Drubin. 2012. Myosin 1E coordinates actin assembly and cargo trafficking during clathrin-mediated endocytosis. *Mol. Biol. Cell*. 23:2891–904. doi:10.1091/mbc.E11-04-0383.

Co, C., D.T. Wong, S. Gierke, V. Chang, and J. Taunton. 2007. Mechanism of Actin Network Attachment to Moving Membranes: Barbed End Capture by N-WASP WH2 Domains. *Cell*. 128:901–913. doi:10.1016/j.cell.2006.12.049.

Duncan, M.C., M.J. Cope, B.L. Goode, B. Wendland, and D.G. Drubin. 2001. Yeast Eps15-like endocytic protein, Pan1p, activates the Arp2/3 complex. *Nat. Cell Biol.* 3:687–90. doi:10.1038/35083087.

Feeser, E.A., C.M.G. Ignacio, M. Krendel, and E.M. Ostap. 2010. Myo1e binds anionic phospholipids with high affinity. *Biochemistry*. 49:9353–60. doi:10.1021/bi1012657.

Fernández-Golbano, I.M., F.Z. Idrissi, J.P. Giblin, B.L. Grosshans, V. Robles, H. Grötsch, M.M. Borrás, and M.I. Geli. 2014. Crosstalk between PI(4,5)P_2 and CK2 Modulates Actin Polymerization during Endocytic Uptake. *Dev. Cell*. 30:746–758. doi:10.1016/j.devcel.2014.07.020.

Geli, M.I., R. Lombardi, B. Schmelzl, and H. Riezman. 2000. An intact SH3 domain is required for myosin I-induced actin polymerization. *EMBO J.* 19:4281–4291. doi:10.1093/emboj/19.16.4281.

Goode, B.L., A.A. Rodal, G. Barnes, and D.G. Drubin. 2001. Activation of the Arp2/3 Complex by the Actin Filament Binding Protein Abp1p. *J. Cell Biol.* 153:627–634. doi:10.1083/jcb.153.3.627.

Goodson, H. V, B.L. Anderson, H.M. Warrick, L.A. Pon, and J.A. Spudich. 1996. Synthetic lethality screen identifies a novel yeast myosin I gene (MYO5): myosin I proteins are required for polarization of the actin cytoskeleton. *J. Cell Biol.* 133:1277–1291. doi:10.1083/JCB.133.6.1277.

Grassart, A., A.T. Cheng, S.H. Hong, F. Zhang, N. Zenzer, Y. Feng, D.M. Briner, G.D. Davis, D. Malkov, and D.G. Drubin. 2014. Actin and dynamin2 dynamics and interplay during clathrin-mediated endocytosis. *J. Cell Biol.* 205:721–735. doi:10.1083/jcb.201403041.

Hassinger, J.E., G. Oster, D.G. Drubin, and P. Rangamani. 2017. Design principles for robust vesiculation in clathrin-mediated endocytosis. *Proc. Natl. Acad. Sci.* 114:E1118–E1127. doi:10.1073/pnas.1617705114.

Idrissi, F.-Z., A. Blasco, A. Espinal, and M.I. Geli. 2012. Ultrastructural dynamics of proteins involved in endocytic budding. *Proc. Natl. Acad. Sci.* 109:E2587–E2594. doi:10.1073/pnas.1202789109.

Inagaki, N., and H. Katsuno. 2017. Actin Waves: Origin of Cell Polarization and Migration? *Trends Cell Biol.* 27:515–526. doi:10.1016/j.tcb.2017.02.003.

Kaksonen, M., Y. Sun, and D.G. Drubin. 2003. A pathway for association of receptors, adaptors, and actin during endocytic internalization. *Cell*. 115:475–87.

Kaksonen, M., C.P. Toret, and D.G. Drubin. 2005. A modular design for the clathrin- and actin-mediated endocytosis machinery. *Cell*. 123:305–20. doi:10.1016/j.cell.2005.09.024.

Krendel, M., E.K. Osterweil, and M.S. Mooseker. 2007. Myosin 1E interacts with synaptojanin-1 and dynamin and is involved in endocytosis. *FEBS Lett.* 581:644–50. doi:10.1016/j.febslet.2007.01.021.

Lewellyn, E.B., R.T.A. Pedersen, J. Hong, R. Lu, M. Huntly, and D.G. Drubin. 2015. An Engineered Minimal WASP-Myosin Fusion Protein Reveals Essential Functions for Endocytosis. *Dev. Cell*. 35:281–294. doi:10.1016/j.devcel.2015.10.007.

Longtine, M.S., a McKenzie, D.J. Demarini, N.G. Shah, a Wach, a Brachat, P. Philippsen, and J.R. Pringle. 1998. Additional modules for versatile and economical PCR-based gene deletion and modification in *Saccharomyces cerevisiae*. *Yeast*. 14:953–61. doi:10.1002/(SICI)1097-0061(199807)14:10<953::AID-YEA293>3.0.CO;2-U.

MacQuarrie, C.D., M. Mangione, R. Carroll, M. James, K.L. Gould, and V. Sirotkin. 2018. Adaptor protein Bbc1 regulates localization of Wsp1 and Vrp1 during endocytic actin patch assembly. *bioRxiv*. 389015. doi:10.1101/389015.

Michelot, A., M. Costanzo, A. Sarkeshik, C. Boone, J.R. Yates, and D.G. Drubin. 2010. Reconstitution and protein composition analysis of endocytic actin patches. *Curr. Biol.* 20:1890–1899. doi:10.1016/j.cub.2010.10.016.

Mund, M., J.A. Van Der Beek, J. Deschamps, S. Dmitrieff, P. Hoess, J.L. Monster, A. Picco, F. Nedelec, M. Kaksonen, and J. Ries. 2018. Systematic Nanoscale Analysis of Endocytosis Links Efficient Vesicle Formation to Patterned Actin Nucleation. *Cell*. 174:884–896. doi:10.1016/j.cell.2018.06.032.

Nolen, B.J., N. Tomasevic, A. Russell, D.W. Pierce, Z. Jia, C.D. McCormick, J. Hartman, R. Sakowicz, and T.D. Pollard. 2009. Characterization of two classes of small molecule inhibitors of Arp2/3 complex. *Nature*. 460:1031–1034. doi:10.1038/nature08231.

Peng, Y., A. Grassart, R. Lu, C.C.L. Wong, J. Yates, G. Barnes, and D.G. Drubin. 2015. Casein Kinase 1 Promotes Initiation of Clathrin-Mediated Endocytosis. *Dev. Cell*. 32:231–240. doi:10.1016/j.devcel.2014.11.014.

Picco, A., M. Mund, J. Ries, F. Nedelec, and M. Kaksonen. 2015. Visualizing the functional architecture of the endocytic machinery. *Elife*. 1–29. doi:10.7554/eLife.04535.

Skruzny, M., T. Brach, R. Ciuffa, S. Rybina, M. Wachsmuth, and M. Kaksonen. 2012. Molecular basis for coupling the plasma membrane to the actin cytoskeleton during clathrin-mediated endocytosis. *Proc. Natl. Acad. Sci.* 109:E2533–E2542. doi:10.1073/pnas.1207011109.

Sokac, A.M., C. Schietroma, C.B. Gundersen, and W.M. Bement. 2006. Myosin-1c couples assembling actin to membranes to drive compensatory endocytosis. *Dev. Cell*. 11:629–40. doi:10.1016/j.devcel.2006.09.002.

Soulard, A., T. Lechler, V. Spiridonov, A. Shevchenko, A. Shevchenko, R. Li, and B. Winsor. 2002. *Saccharomyces cerevisiae* Bzz1p is implicated with type I myosins in actin patch polarization and is able to recruit actin-polymerizing machinery in vitro. *Mol. Cell. Biol.* 22:7889–7906. doi:10.1128/MCB.22.22.7889-7906.2002.

Sun, Y., N.T. Leong, T. Wong, and D.G. Drubin. 2015. A Pan1/End3/Sla1 complex links Arp2/3-mediated actin assembly to sites of clathrin-mediated endocytosis. *Mol. Biol. Cell*. 26:3841–3856. doi:10.1091/mbc.E15-04-0252.

Sun, Y., A.C. Martin, and D.G. Drubin. 2006. Endocytic Internalization in Budding Yeast Requires Coordinated Actin Nucleation and Myosin Motor Activity. *Dev. Cell*. 11:33–46. doi:10.1016/j.devcel.2006.05.008.

Toret, C.P., L. Lee, M. Sekiya-Kawasaki, and D.G. Drubin. 2008. Multiple pathways regulate endocytic coat disassembly in *Saccharomyces cerevisiae* for optimal downstream trafficking. *Traffic*. 9:848–859. doi:10.1111/j.1600-0854.2008.00726.x.

Wang, X., B.J. Galletta, J.A. Cooper, and A.E. Carlsson. 2016. Actin-Regulator Feedback Interactions during Endocytosis. *Biophys. J.* 110:1430–1443. doi:10.1016/j.bpj.2016.02.018.

Weiner, O.D., W.A. Marganski, L.F. Wu, S.J. Altschuler, and M.W. Kirschner. 2007. An actin-based wave generator organizes cell motility. *PLoS Biol.* 5:2053–2063. doi:10.1371/journal.pbio.0050221.

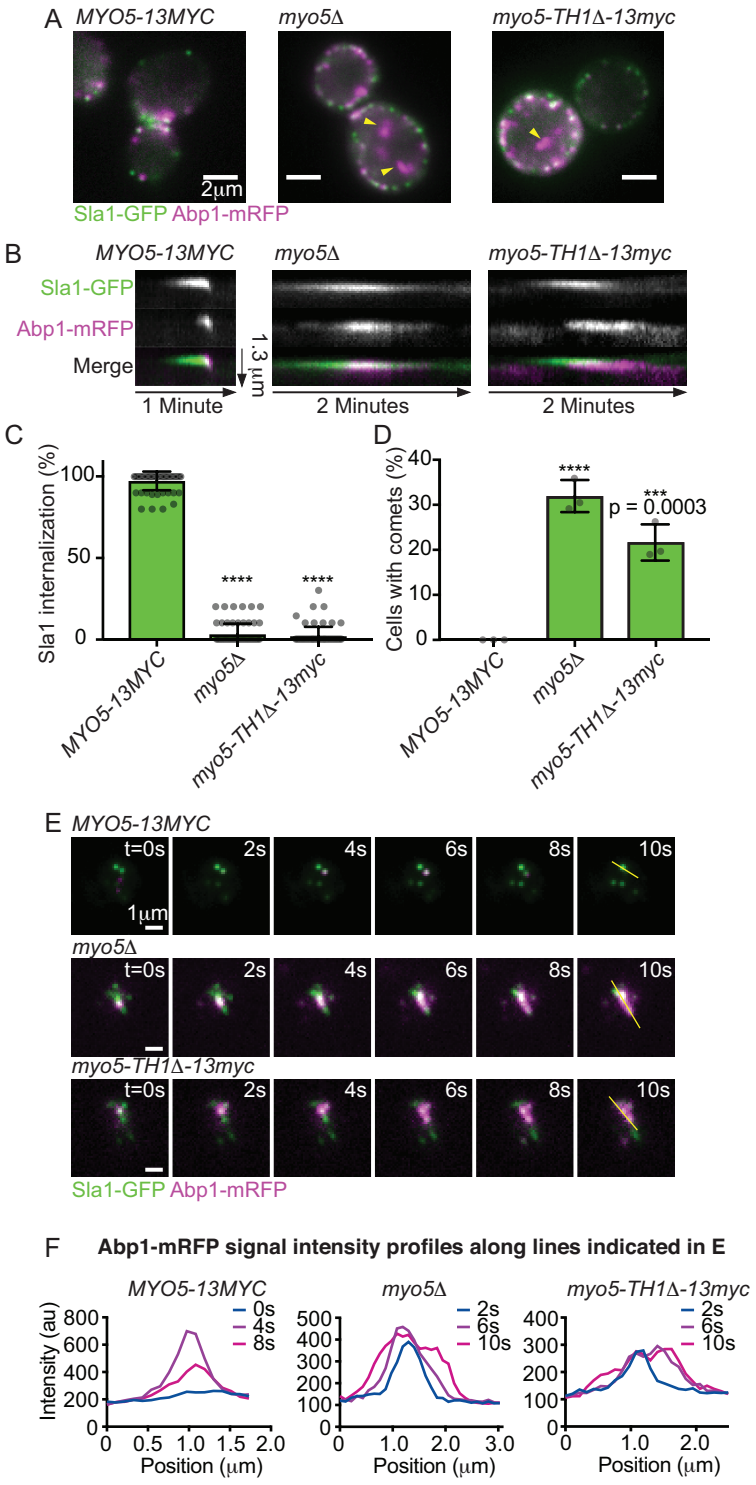
A
MYO5-13MYC
myo5Δ
myo5-TH1Δ-13myc
2μm
Sla1-GFP Abp1-mRFP
B
MYO5-13MYC
myo5Δ
myo5-TH1Δ-13myc
Sla1-GFP
Abp1-mRFP
Merge
1.3 μm
1 Minute
2 Minutes
2 Minutes
C
Sla1 internalization (%)
100
50
0
****
****
MYO5-13MYC
myo5Δ
myo5-TH1Δ-13myc
D
Cells with comets (%)
40
30
20
10
0
****
***
p = 0.0003
MYO5-13MYC
myo5Δ
myo5-TH1Δ-13myc
E
MYO5-13MYC
t=0s
2s
4s
6s
8s
10s
1μm
myo5Δ
myo5-TH1Δ-13myc
Sla1-GFP Abp1-mRFP
F
Abp1-mRFP signal intensity profiles along lines indicated in E
MYO5-13MYC
myo5Δ
myo5-TH1Δ-13myc
Intensity (au)
0s
4s
8s
2s
6s
10s
Position (μm)
Position (μm)
Position (μm)

Figure 2.1: Membrane-bound Myo5 restricts actin assembly to endocytic sites.

(A) Stills from epifluorescence movies of cells endogenously expressing Sla1-GFP (green) to label endocytic coats and Abp1-mRFP (magenta) to label endocytic actin networks. Yellow arrowheads mark cytoplasmic actin comets in mutants. (B) Kymographs of individual attempted endocytic events. Extracellular space is up and the cytoplasm down. (C) Quantification Sla1-GFP patch internalization during a 2-minute movie. Each data point represents the proportion of patches internalized in one cell. n = 61 (*MYO5*), 64 (*myo5Δ*), and 65 (*myo5-TH1Δ*) cells observed. Asterisks denote statistical significance compared to *MYO5* by one-way ANOVA (F = 5168) followed by Dunnett's test. Error bars are standard deviation (SD). (D) Quantification of the proportion of cells manifesting cytoplasmic actin comets in epifluorescence movies. Each data point represents a separate experiment during which at least 110 cells were observed. Asterisks denote statistical significance compared to *MYO5* as in C (F = 82.29). Error bars are SD. (E) Montages from TIRFM movies of cells endogenously expressing Sla1-GFP (green) and Abp1-mRFP (magenta). Yellow lines indicate selections used for intensity profiles in Figure 1F. Montages are representative of observations from 80 (*MYO5*), 156 (*myo5Δ*), and 71 (*myo5-TH1Δ*) cells. (F) Abp1-mRFP fluorescence intensity profiles from the indicated time points along the line indicated in E. ****p<0.0001. All cells are *myo3Δ.*

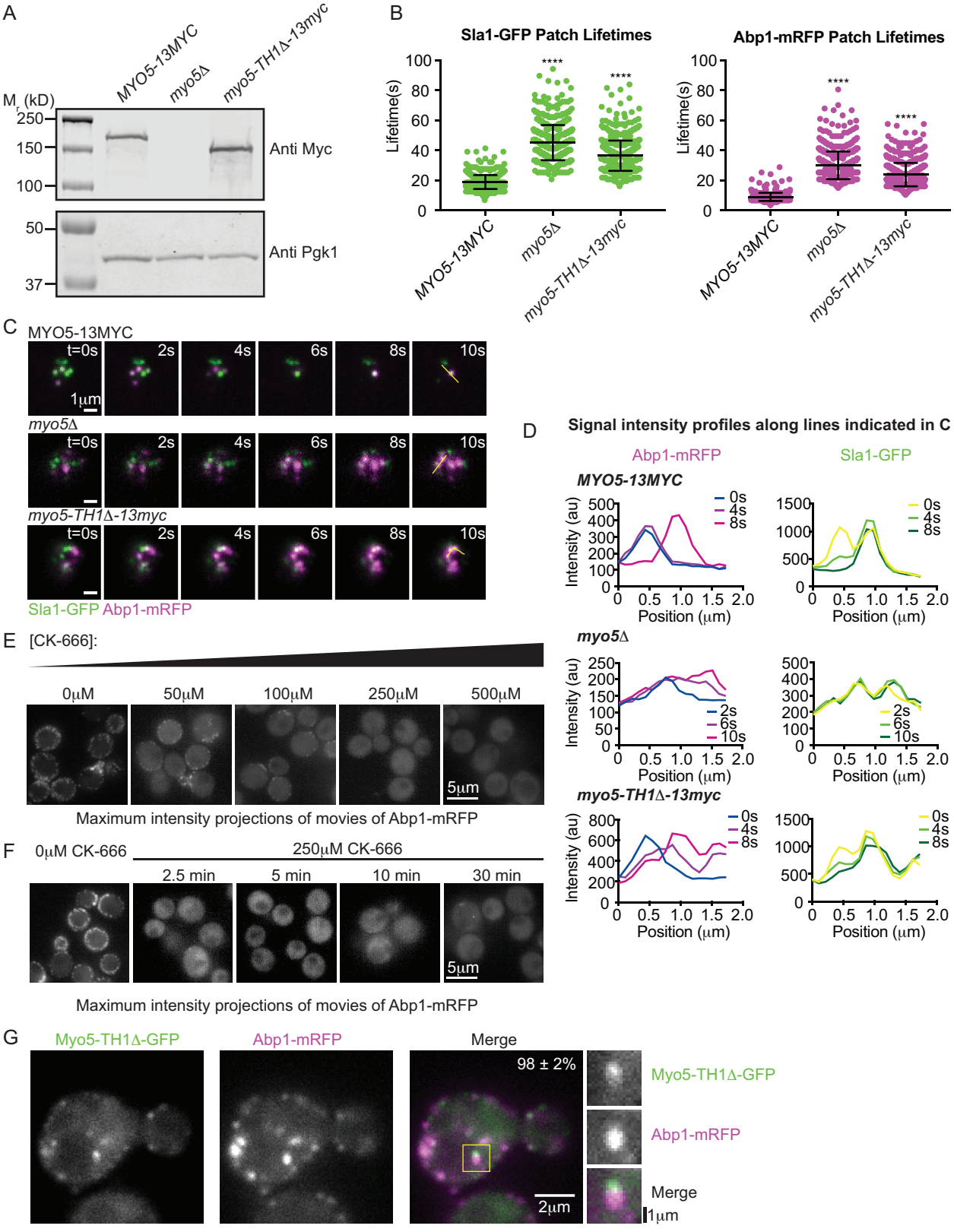
A
MYO5-13MYC
myo5Δ
myo5-TH1Δ-13myc
M_r (kD)
250
150
100
50
37
Anti Myc
Anti Pgk1
B
Sla1-GFP Patch Lifetimes
Abp1-mRFP Patch Lifetimes
Lifetime(s)
100
80
60
40
20
0
****
MYO5-13MYC
myo5Δ
myo5-TH1Δ-13myc
C
MYO5-13MYC
t=0s
2s
4s
6s
8s
10s
1μm
myo5Δ
myo5-TH1Δ-13myc
Sla1-GFP Abp1-mRFP
D
Signal intensity profiles along lines indicated in C
Abp1-mRFP
Sla1-GFP
MYO5-13MYC
myo5Δ
myo5-TH1Δ-13myc
Intensity (au)
Position (μm)
0s
4s
8s
2s
6s
10s
E
[CK-666]:
0μM
50μM
100μM
250μM
500μM
5μm
Maximum intensity projections of movies of Abp1-mRFP
F
0μM CK-666
250μM CK-666
2.5 min
5 min
10 min
30 min
5μm
Maximum intensity projections of movies of Abp1-mRFP
G
Myo5-TH1Δ-GFP
Abp1-mRFP
Merge
98 ± 2%
2μm
Myo5-TH1Δ-GFP
Abp1-mRFP
Merge
1μm

Figure 2.2: Related to Figures 2.1 and 2.3: Membrane-bound Myo5 restricts actin assembly and actin assembly factors to endocytic sites.

(A) Immunoblot of *MYO5-13Myc, myo5Δ,* and *myo5-TH1Δ-13Myc* strains used in this study. Myo5 variants were recognized via a 13Myc epitope tag with the 9E10 anti myc antibody. Pgk1 was probed as a loading control. (B) Sla1-GFP and Abp1-mRFP patch lifetimes for each indicated genotype. n = 587 (*MYO5*), 600 (*myo5Δ*), and 596 (*myo5-TH1Δ*) patches measured. Asterisks denote statistical significance compared to *MYO5* as in Figure 1C (F_{Sla1} = 1212, F_{Abp1} = 1342). Error bars are SD. (C) Additional montages from TIRFM movies of cells of the indicated genotypes endogenously expressing Sla1-GFP (green) and Abp1-mRFP (magenta). Yellow lines indicate selections used for intensity profiles in D. (D) Abp1-mRFP fluorescence intensity profiles from the indicated time points along the line indicated in C. (E) Effects of increasing concentrations of CK-666 on assembly of endocytic actin networks, labeled by Abp1-mRFP in wild-type *MYO5* cells. Cells were treated with the indicated concentration of CK-666 for 45 minutes. (F) Effects of increasing CK-666 treatment times on assembly of endocytic actin networks, labeled by Abp1-mRFP in wild-type *MYO5* cells. (G) Still from an epifluorescence movie of a *myo5-TH1Δ-GFP* (green) cell endogenously expressing Abp1-mRFP (magenta). The yellow box indicates an Abp1-mRFP comet with Myo5-TH1Δ-GFP at the tip. This selection is enlarged two-fold and shown in gray scale at right. The percentage shown is the proportion of Abp1-mRFP comets with associated GFP signal ± SD. n = 153 total comets observed. ****p<0.0001. All cells are *myo3Δ.*

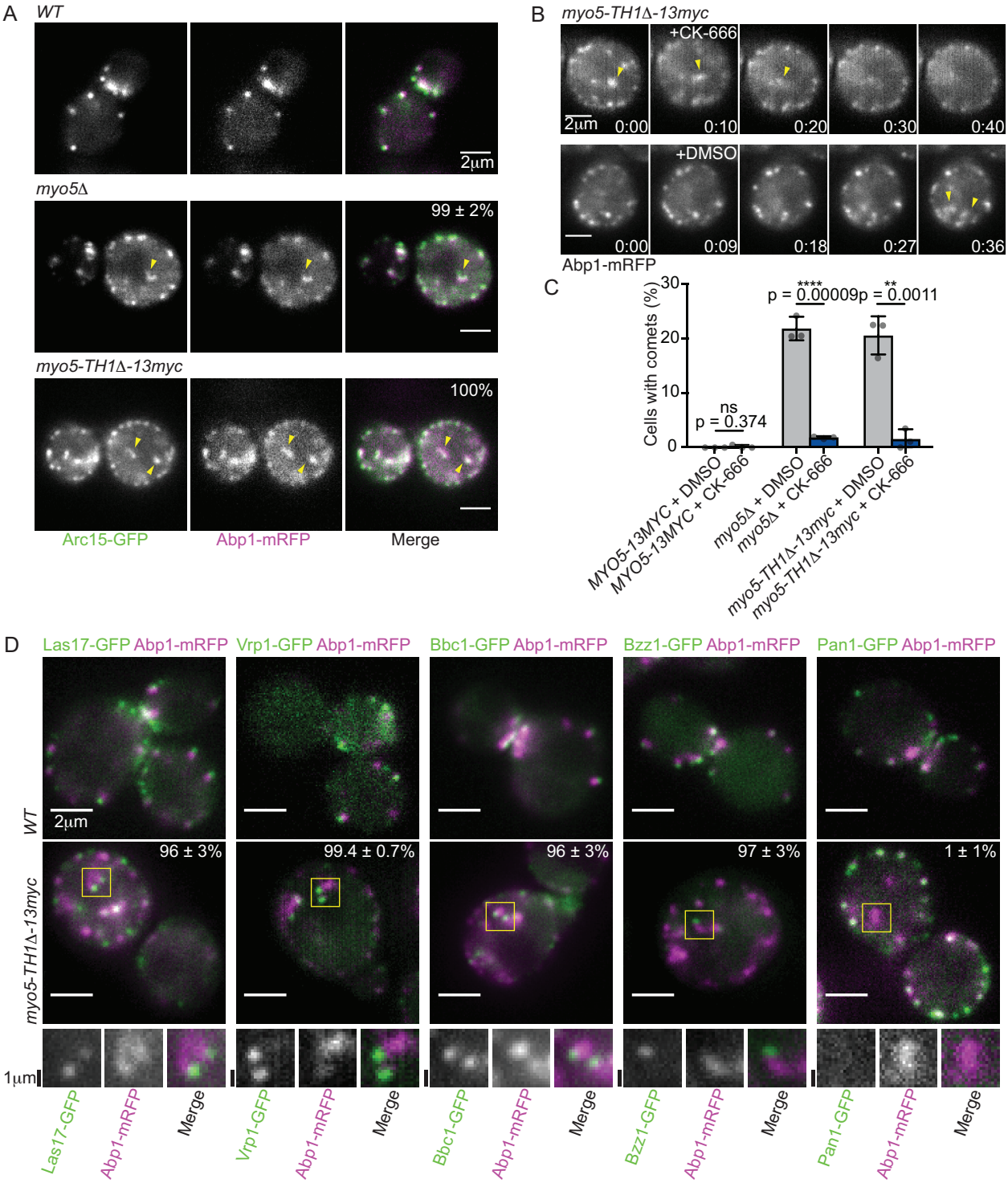
A
WT
2μm
myo5Δ
99 ± 2%
myo5-TH1Δ-13myc
100%
Arc15-GFP
Abp1-mRFP
Merge
B
myo5-TH1Δ-13myc
+CK-666
2μm
0:00
0:10
0:20
0:30
0:40
+DMSO
0:00
0:09
0:18
0:27
0:36
Abp1-mRFP
C
Cells with comets (%)
30
20
10
0
p = 0.00009
****
p = 0.0011
**
ns
p = 0.374
MYO5-13MYC + DMSO
MYO5-13MYC + CK-666
myo5Δ + DMSO
myo5Δ + CK-666
myo5-TH1Δ-13myc + DMSO
myo5-TH1Δ-13myc + CK-666
D
Las17-GFP Abp1-mRFP
Vrp1-GFP Abp1-mRFP
Bbc1-GFP Abp1-mRFP
Bzz1-GFP Abp1-mRFP
Pan1-GFP Abp1-mRFP
WT
2μm
myo5-TH1Δ-13myc
96 ± 3%
99.4 ± 0.7%
96 ± 3%
97 ± 3%
1 ± 1%
1μm
Las17-GFP
Abp1-mRFP
Merge
Vrp1-GFP
Abp1-mRFP
Merge
Bbc1-GFP
Abp1-mRFP
Merge
Bzz1-GFP
Abp1-mRFP
Merge
Pan1-GFP
Abp1-mRFP
Merge

Figure 2.3: Membrane-bound Myo5 restricts the activity of the Arp2/3 complex and its regulators to endocytic sites.

(A) Stills from epifluorescence movies of cells endogenously expressing Arc15-GFP (green) to label the Arp2/3 complex and Abp1-mRFP (magenta). Yellow arrowheads mark cytoplasmic actin comets in mutants. Percentages are proportions of Abp1-mRFP comets with associated Arc15-GFP signal ± SD. n = 192 (*myo5Δ*) and 207 (*myo5-TH1Δ*) total comets observed. (B) Montages from epifluorescence movies during which 250 μM CK-666 or 0.5% DMSO was added to *myo5-TH1Δ* cells endogenously expressing Abp1-mRFP. Yellow arrowheads indicate cytoplasmic actin comets that dissolve upon CK-666 addition and persist upon DMSO addition. Times are minutes:seconds. Montages are representative of 7 experiments. (C) Quantification of the proportion of cells displaying cytoplasmic actin comets in epifluorescence movies in the presence of 0.5% DMSO or 250 μM CK-666. Each data point represents a separate experiment during which at least 50 cells were observed. Asterisks denote statistical significance according to students t tests corrected for multiple comparisons using the two-stage setup method of Benjamani, Kreiger, and Yekutieli with a false discovery rate of 5%. Error bars are SD. (D) Stills from epifluorescence movies of *MYO5* and *myo5-TH1Δ* cells endogenously expressing Abp1-mRFP (magenta) and GFP-tagged Arp2/3 complex regulators (green). Yellow boxes indicate Abp1-mRFP comets with the corresponding GFP-tagged protein at the tip or, in the case of Pan1, absent from the comet. These selections are enlarged two-fold and shown in gray scale below. Percentages are proportions of Abp1-mRFP comets with associated GFP signal ± SD. n = 143, 343, 328, 188, and 179 total comets observed for Las17, Vrp1, Bbc1, Bzz1, and Pan1, respectively. All cells are *myo3Δ.*

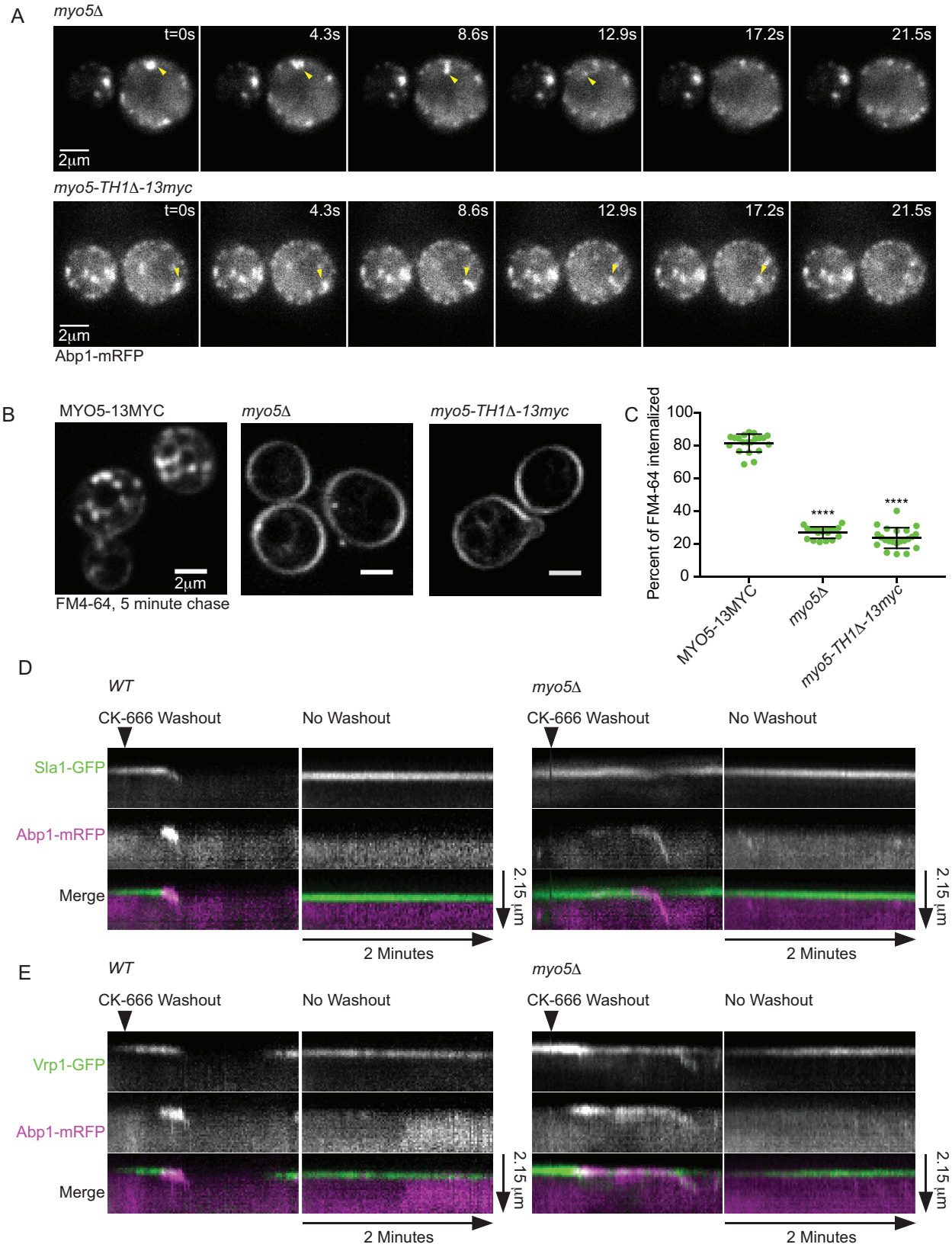
A
myo5Δ
t=0s
4.3s
8.6s
12.9s
17.2s
21.5s
2μm
myo5-TH1Δ-13myc
Abp1-mRFP
B
MYO5-13MYC
myo5Δ
myo5-TH1Δ-13myc
FM4-64, 5 minute chase
C
Percent of FM4-64 internalized
100
80
60
40
20
0
****
MYO5-13MYC
myo5Δ
myo5-TH1Δ-13myc
D
WT
myo5Δ
CK-666 Washout
No Washout
Sla1-GFP
Abp1-mRFP
Merge
2.15 μm
2 Minutes
E
Vrp1-GFP

Figure 2.4: Myo5 couples the assembling actin network to the plasma membrane during clathrin-mediated endocytosis.

(A) Montages from the same epifluorescence movies shown in Figure 2.3A. Yellow arrowheads indicate actin comets pulling away from the PM. Similar behavior was observed in at least 50 cells across many different experiments. (B) Spinning disc confocal images of cells subjected to a 5-minute pulse of FM4-64 staining followed by a 5-minute chase with imaging media. (C) Quantification of percent of FM4-64 signal internalized during a 5-minute chase. n = 20 (*MYO5*), 19 (*myo5Δ*), and 22 (*myo5-TH1Δ*) cells. Asterisks denote statistical significance compared to *MYO5* by one-way ANOVA (F = 767.1) followed by Dunnett's test. Error bars are SD. ****p<0.0001. (D) Kymographs of individual endocytic events following washout of CK-666 or no washout in wild-type *MYO5* and *myo5Δ* cells endogenously expressing Sla1-GFP (green) and Abp1-mRFP (magenta). See Figure 2.5 for montages. Kymographs are representative of 13 (*MYO5*) and 14 (*myo5Δ*) separate experiments. (E) Kymographs as in panel D from movies of cells endogenously expressing Vrp1-GFP (green) and Abp1-mRFP (magenta). Kymographs are representative of 8 (*MYO5*) and 16 (*myo5Δ*) separate experiments. All cells are *myo3Δ.*

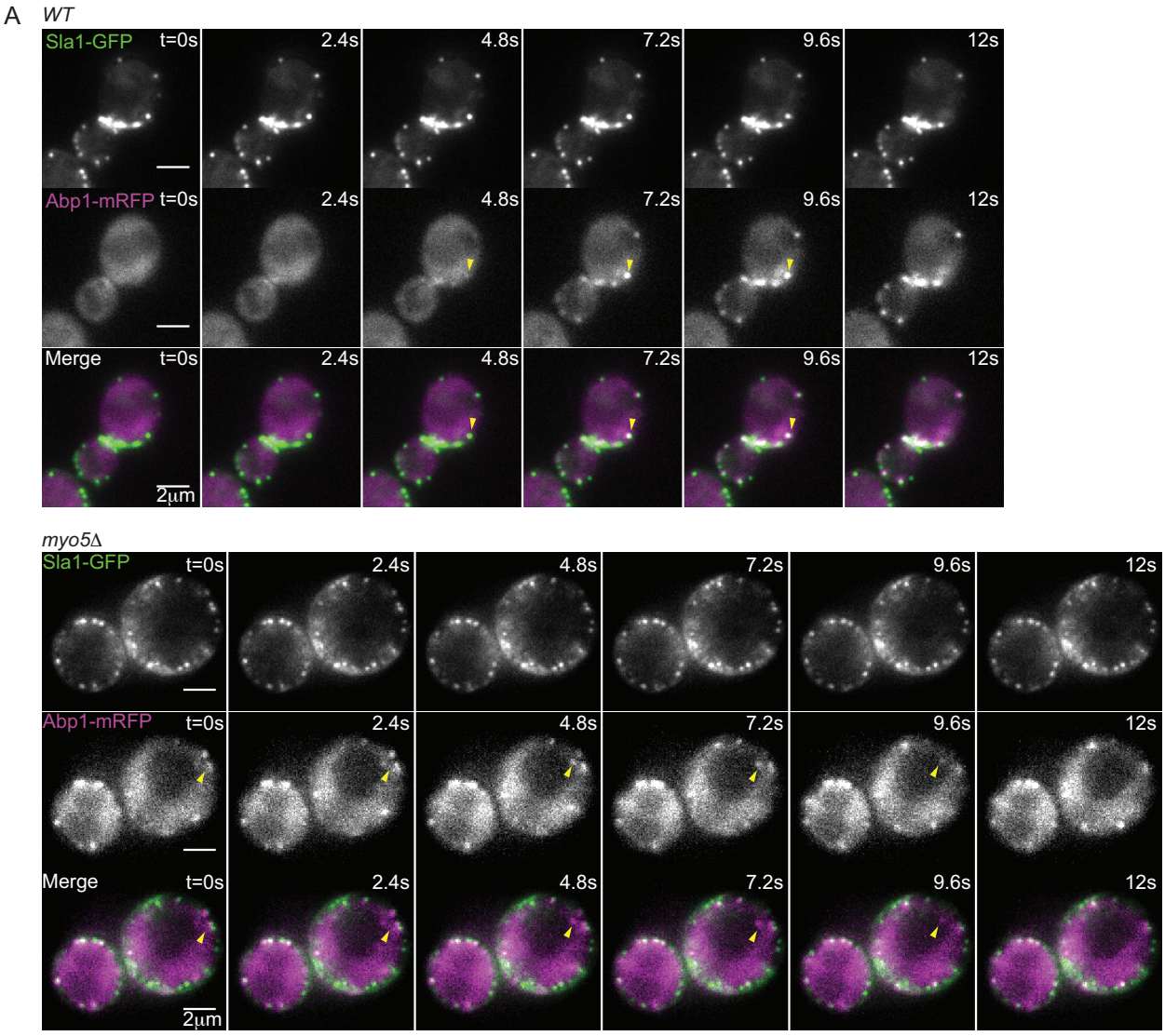
A
WT
Sla1-GFP
Abp1-mRFP
Merge
t=0s
2.4s
4.8s
7.2s
9.6s
12s
2μm
myo5Δ
B
WT
myo5Δ
CK-666 Washout
Sla1-GFP
Abp1-mRFP
Merge
2.15 μm
2 Minutes
C
Abp1 comet velocity (nm/s)
500
400
300
200
100
0

Figure 2.5: Related to Figure 2.4: Myo5 couples the assembling actin network to the plasma membrane during clathrin-mediated endocytosis.

(A) Montages from epifluorescence movies of cells of the indicated genotypes endogenously expressing Sla1-GFP (green) and Abp1-mRFP (magenta) following washout of CK-666. Yellow arrowheads mark endocytic actin assembly events. (B) Kymographs of additional individual endocytic events following washout of CK-666 from the movies shown in A. (C) Quantification of the velocity of Abp1-mRFP actin comets as they leave the plasma membrane following washout of CK-666 in *myo5Δ* cells. n = 31 comets tracked from 28 cells. Error bars are SD. All cells are *myo3Δ.*

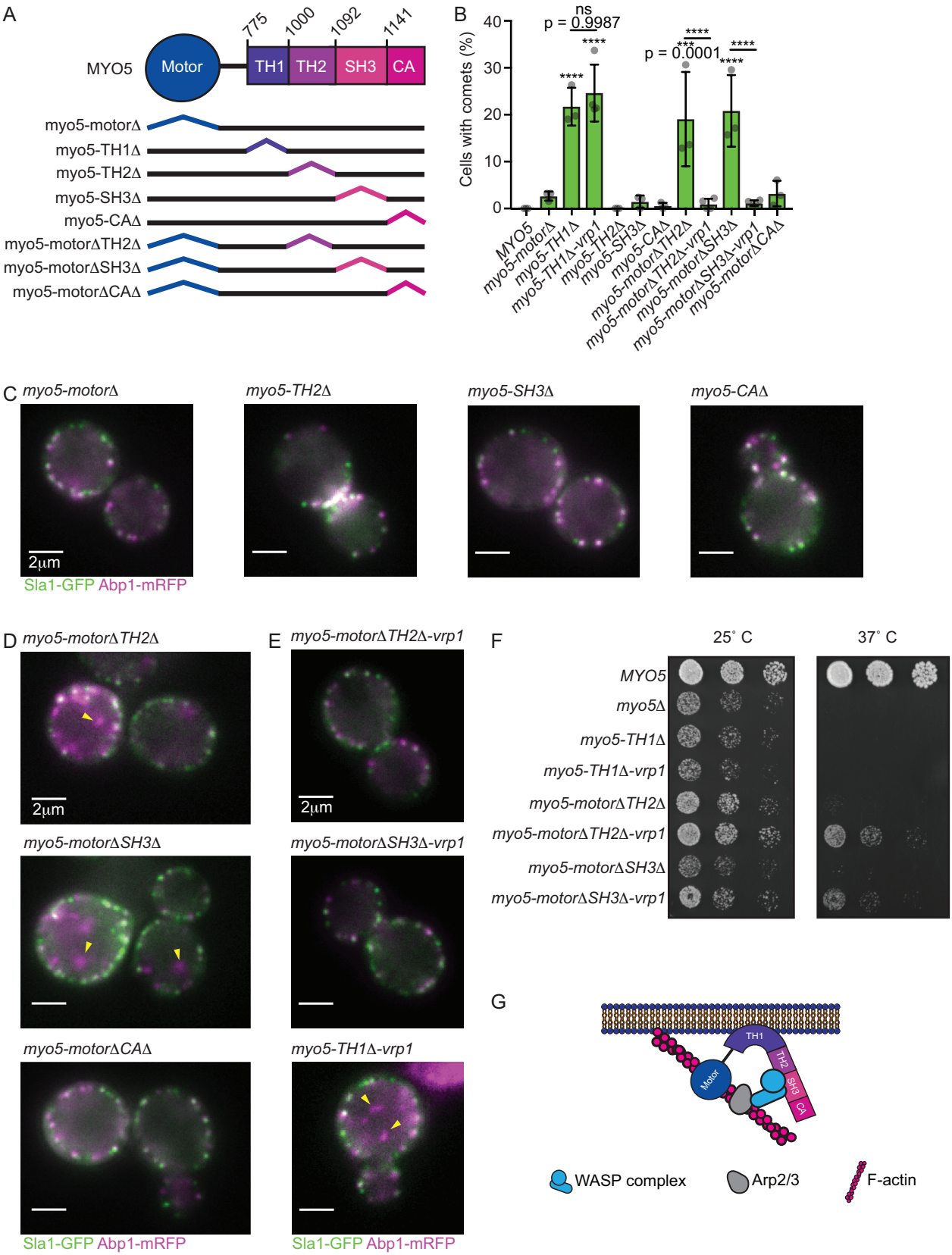
A
MYO5
Motor
775
1000
1092
1141
TH1
TH2
SH3
CA
myo5-motorΔ
myo5-TH1Δ
myo5-TH2Δ
myo5-SH3Δ
myo5-CAΔ
myo5-motorΔTH2Δ
myo5-motorΔSH3Δ
myo5-motorΔCAΔ
B
Cells with comets (%)
ns
p = 0.9987
p = 0.0001
****
***
MYO5
myo5-motorΔ
myo5-TH1Δ
myo5-TH1Δ-vrp1
myo5-TH2Δ
myo5-SH3Δ
myo5-CAΔ
myo5-motorΔTH2Δ
myo5-motorΔTH2Δ-vrp1
myo5-motorΔSH3Δ
myo5-motorΔSH3Δ-vrp1
myo5-motorΔCAΔ
C
myo5-motorΔ
myo5-TH2Δ
myo5-SH3Δ
myo5-CAΔ
2μm
Sla1-GFP Abp1-mRFP
D
myo5-motorΔTH2Δ
myo5-motorΔSH3Δ
myo5-motorΔCAΔ
E
myo5-motorΔTH2Δ-vrp1
myo5-motorΔSH3Δ-vrp1
myo5-TH1Δ-vrp1
F
25˚ C
37˚ C
MYO5
myo5Δ
myo5-TH1Δ
myo5-TH1Δ-vrp1
myo5-motorΔTH2Δ
myo5-motorΔTH2Δ-vrp1
myo5-motorΔSH3Δ
myo5-motorΔSH3Δ-vrp1
G
TH1
TH2
SH3
CA
Motor
WASP complex
Arp2/3
F-actin

Figure 2.6: Molecular determinants of myosin-mediated coupling of actin assembly to endocytic sites.

(A) Schematic diagram of Myo5 domains and deletion mutants analyzed. Domain boundaries are marked with the corresponding amino acid number. All mutants were linked to a C-terminal 13Myc tag. (B) Quantification of the proportion of cells harboring the indicated *MYO5* truncation mutant displaying cytoplasmic actin comets in epifluorescence movies. Each data point represents a separate experiment during which at least 70 cells were observed. Data points for *MYO5* and *myo5-TH1Δ* are repeated from Figure 2.1C. Asterisks denote statistical significance compared to *MYO5* or between bracketed variants after one-way ANOVA (F = 18.88) followed by Sidak's multiple comparisons test. Error bars are SD. (C-E) Stills from epifluorescence movies of cells endogenously expressing Sla1-GFP (green) and Abp1-mRFP (magenta). Yellow arrowheads indicate cytoplasmic actin comets in mutants. (F) Growth of cells harboring truncation mutations in *MYO5* on YPD plates. Photos are representative of results from 3 separate experiments. (G) Schematic diagram illustrating membrane anchoring of actin assembly factors by Myo5. All cells are *myo3Δ.*

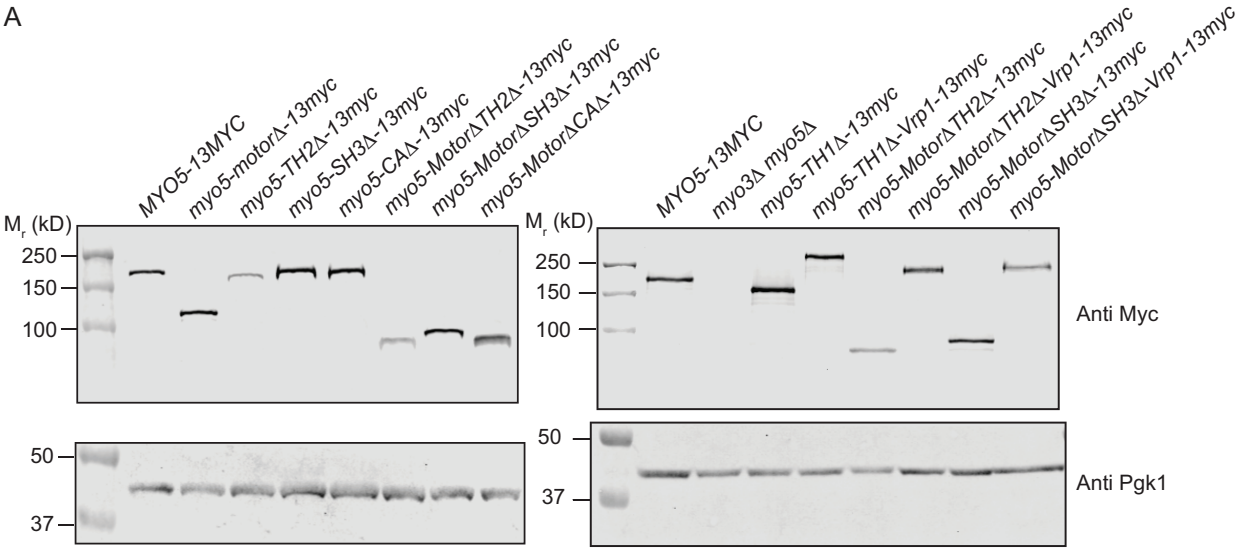
A
MYO5-13MYC
myo5-motorΔ-13myc
myo5-TH2Δ-13myc
myo5-SH3Δ-13myc
myo5-CAΔ-13myc
myo5-MotorΔTH2Δ-13myc
myo5-MotorΔSH3Δ-13myc
myo5-MotorΔCAΔ-13myc
Mr (kD)
250
150
100
50
37
MYO5-13MYC
myo3Δ myo5Δ
myo5-TH1Δ-13myc
myo5-TH1Δ-Vrp1-13myc
myo5-MotorΔTH2Δ-13myc
myo5-MotorΔTH2Δ-Vrp1-13myc
myo5-MotorΔSH3Δ-13myc
myo5-MotorΔSH3Δ-Vrp1-13myc
Anti Myc
Anti Pgk1

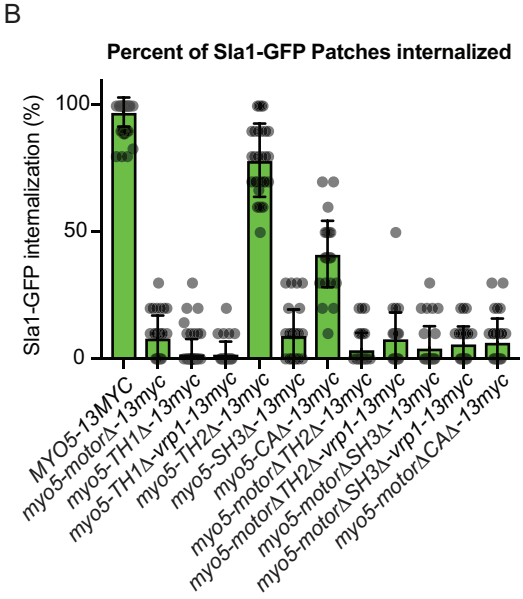
B
Percent of Sla1-GFP Patches internalized
Sla1-GFP internalization (%)
100
50
0
MYO5-13MYC
myo5-motorΔ-13myc
myo5-TH1Δ-13myc
myo5-TH1Δ-vrp1-13myc
myo5-TH2Δ-13myc
myo5-SH3Δ-13myc
myo5-CAΔ-13myc
myo5-motorΔTH2Δ-13myc
myo5-motorΔTH2Δ-vrp1-13myc
myo5-motorΔSH3Δ-13myc
myo5-motorΔSH3Δ-vrp1-13myc
myo5-motorΔCAΔ-13myc

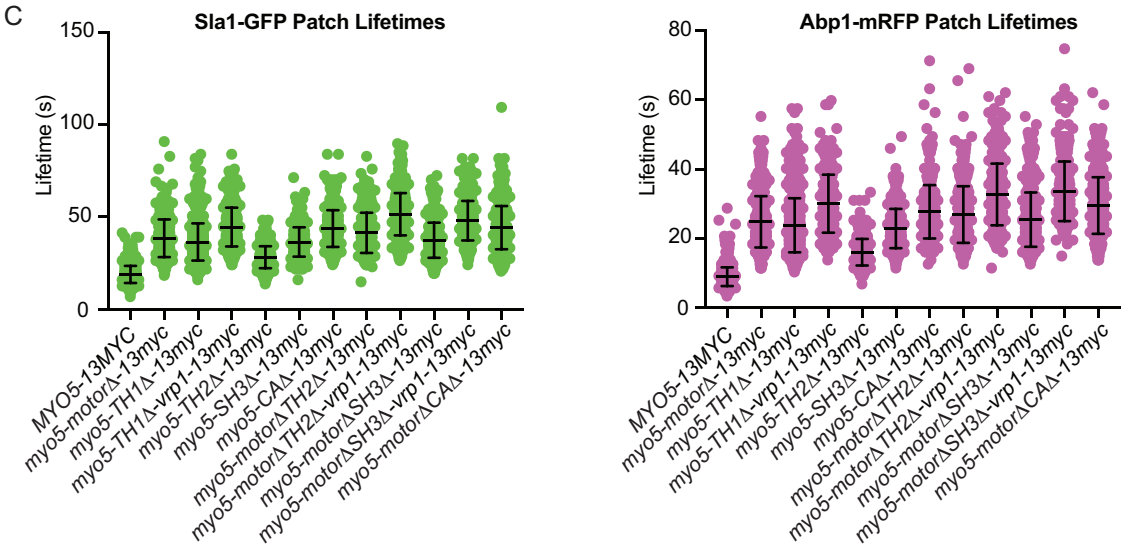
C
Sla1-GFP Patch Lifetimes
Lifetime (s)
150
100
50
0
Abp1-mRFP Patch Lifetimes
Lifetime (s)
80
60
40
20
0
MYO5-13MYC
myo5-motorΔ-13myc
myo5-TH1Δ-13myc
myo5-TH1Δ-vrp1-13myc
myo5-TH2Δ-13myc
myo5-SH3Δ-13myc
myo5-CAΔ-13myc
myo5-motorΔTH2Δ-13myc
myo5-motorΔTH2Δ-vrp1-13myc
myo5-motorΔSH3Δ-13myc
myo5-motorΔSH3Δ-vrp1-13myc
myo5-motorΔCAΔ-13myc

Figure 2.7: Related to Figure 2.6: Molecular determinants of myosin-mediated coupling of actin assembly to endocytic sites.

(A) Immunoblot of *MYO5* truncation mutant strains used in this study. Myo5 variants were recognized via a 13Myc epitope tag with the 9E10 anti myc antibody. Pgk1 was probed as a loading control. (B) Quantification of the proportion of Sla1-GFP vesicles internalized in individual cells of each indicated genotype during a 2-minute movie. Data for *MYO5* and *myo5-TH1Δ* are repeated from Figure 2.1D. n = 61 (*MYO5*), 65 (*myo5-TH1Δ*), 31 (*myo5-TH2Δ*) cells, and 30 cells for all other variants. All variants are statistically significantly different ($p < 0.0001$) when compared to *MYO5* by one-way ANOVA ($F = 641.2$) followed by Dunnett's test. (C) Sla1-GFP and Abp1-mRFP patch lifetimes for each indicated genotype. Data for *MYO5* and *myo5-TH1Δ* are repeated from Figure 2.2B. n = 587 (*MYO5*), 596 (*myo5-TH1Δ*), 306 (*myo5-TH2Δ*) patches, and 300 patches measured for all other variants. All variants are statistically significantly different ($p < 0.0001$) when compared to *MYO5* by one-way ANOVA ($F_{Sla1} = 373.8$, $F_{Abp1} = 409.6$) followed by Dunnett's test. All cells analyzed were *myo3Δ.*

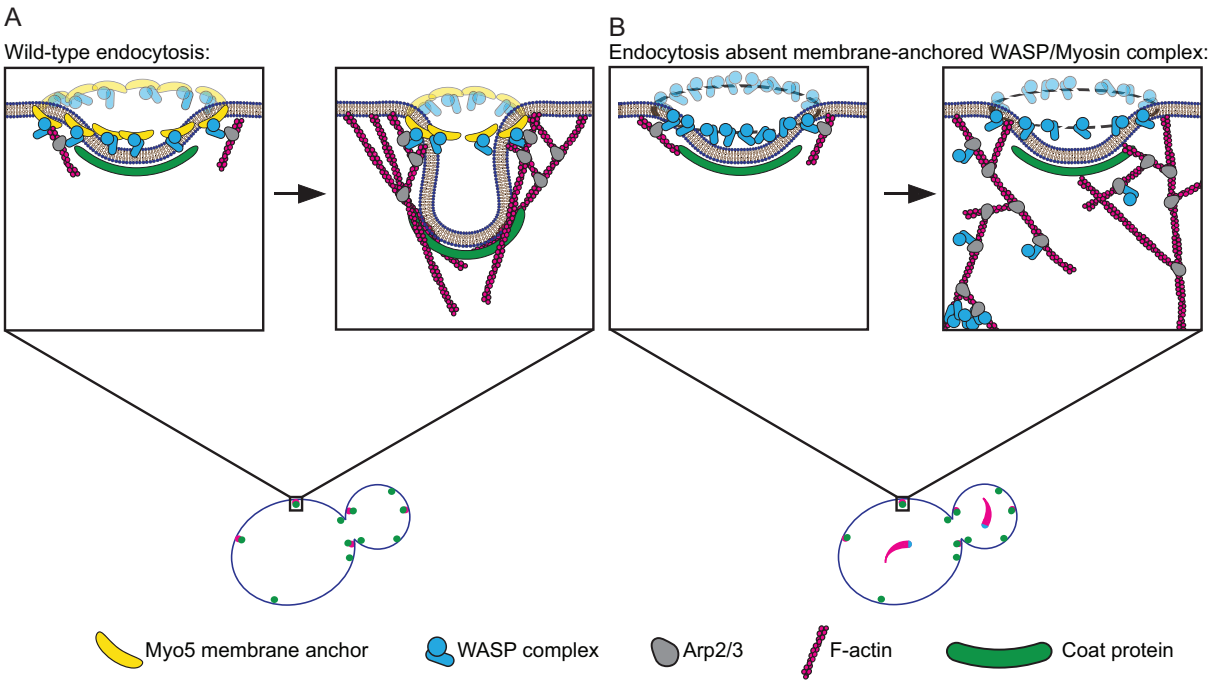
A
Wild-type endocytosis:
B
Endocytosis absent membrane-anchored WASP/Myosin complex:
Myo5 membrane anchor
WASP complex
Arp2/3
F-actin
Coat protein

Figure 2.8: Model for Myo5 function in anchoring actin assembly to the plasma membrane at endocytic sites.

(A) Myo5 (yellow bananas) restricts activation of the Arp2/3 complex (grey avocados) by the WASP complex (blue widgets) to a discrete location, generating an actin array that grows predominantly in the same direction to generate force. (B) Absent this critical linkage, Arp2/3 activators splinter off of the plasma membrane, leading to Arp2/3 complex activation throughout the actin network. Delocalized Arp2/3 complex activation results in disordered actin arrays that fail to produce force. In the most catastrophic cases, the Arp2/3 complex and its activators pull away from the plasma membrane completely to form cytoplasmic actin comets (lower left of zoom).

Table 2.1: strains used in this study

Name	Genotype	Source
DDY1102	*MATa/MATα his3-Δ200/his3-Δ200, leu2-3, 112/leu2-3, 112, ura3-52/ura3-52, ade2-1/ADE2, lys2-801/LYS2*	Drubin Lab collection
DDY5684	*MATa/MATα his3-Δ200/his3-Δ200, leu2-3, 112/leu2-3, 112, ura3-52/ura3-52, MYO5/myo5Δ::HygMX, myo3Δ::cgLEU2/myo3Δ::cgLEU2, ABP1-mRFP::HIS3/ABP1-mRFP::HIS3, SLA1-GFP::KanMX6/SLA1-GFP::KanMX6*	This study
DDY5685	*MATa his3-Δ200, leu2-3, 112, ura3-52, MYO5-13MYC::URA3, myo3Δ::cgLEU2, ABP1-mRFP::HIS3, SLA1-GFP::KanMX*	This study
DDY5686	*MATa his3-Δ200, leu2-3, 112, ura3-52, myo5Δ::URA3, myo3Δ::cgLEU2, ABP1-mRFP::HIS3, SLA1-GFP::KanMX6*	This study
DDY5687	*MATa his3-Δ200, leu2-3, 112, ura3-52, myo5-TH1Δ-13myc::URA3, myo3Δ::cgLEU2, ABP1-mRFP::HIS3, SLA1-GFP::KanMX6*	This study
DDY5688	*MATa his3-Δ200, leu2-3, 112, ura3-52, myo3Δ::cgLEU2, ABP1-mRFP::HIS3, ARC15-GFP::KanMX*	This study
DDY5689	*MATa his3-Δ200, leu2-3, 112, ura3-52, myo5Δ::URA3, myo3Δ::cgLEU2, ABP1-mRFP::HIS3, ARC15-GFP::KanMX*	This study
DDY5690	*MATa his3-Δ200, leu2-3, 112, ura3-52, myo5-TH1Δ-13myc::URA3, myo3Δ::cgLEU2, ABP1-mRFP::HIS3, ARC15-GFP::KanMX*	This study
DDY5691	*MATa his3-Δ200, leu2-3, 112, ura3-52, myo3Δ::cgLEU2, ABP1-mRFP::HIS3, LAS17-GFP::HIS3*	This study
DDY5692	*MATa his3-Δ200, leu2-3, 112, ura3-52, myo5-TH1Δ-13myc::URA3, myo3Δ::cgLEU2, ABP1-mRFP::HIS3, LAS17-GFP::HIS3*	This study
DDY5693	*MATa his3-Δ200, leu2-3, 112, ura3-52, myo3Δ::cgLEU2, ABP1-mRFP::HIS3, VRP1-GFP::KanMX*	This study
DDY5694	*MATa his3-Δ200, leu2-3, 112, ura3-52, myo5-TH1Δ-13myc::URA3, myo3Δ::cgLEU2, ABP1-mRFP::HIS3, VRP1-GFP::KanMX*	This study
DDY5695	*MATa his3-Δ200, leu2-3, 112, ura3-52, myo3Δ::cgLEU2, ABP1-mRFP::HIS3, BBC1-GFP::HIS3*	This study

DDY5696	*MATα his3-Δ200, leu2-3, 112, ura3-52, myo5-TH1Δ-13myc::URA3, myo3Δ::cgLEU2, ABP1-mRFP::HIS3, BBC1-GFP::HIS3*	This study
DDY5697	*MATα his3-Δ200, leu2-3, 112, ura3-52, myo3Δ::cgLEU2, ABP1-mRFP::HIS3, BZZ1-GFP::HIS3*	This study
DDY5698	*MATa his3-Δ200, leu2-3, 112, ura3-52, myo5-TH1Δ-13myc::URA3, myo3Δ::cgLEU2, ABP1-mRFP::HIS3, BZZ1-GFP::HIS3*	This study
DDY5699	*MATa his3-Δ200, leu2-3, 112, ura3-52, myo3Δ::cgLEU, ABP1-mRPF::HIS3, PAN1-GFP::HIS3*	This study
DDY5700	*MATa his3-Δ200, leu2-3, 112, ura3-52, myo5-TH1Δ-13myc::URA3, myo3Δ::cgLEU2, ABP1-mRFP::HIS3, PAN1-GFP::HIS3*	This study
DDY4773	*MATa his3-Δ200, leu2-3, 112, ura3-52, MYO5-13MYC::URA3, myo3Δ::cgLEU2*	Lewellyn *et al.* 2015
DDY4828	*MATa his3-Δ200, leu2-3, 112, ura3-52, myo5□::URA3, myo3Δ::cgLEU2*	Lewellyn *et al.* 2015
DDY4775	*MATa his3-□200, leu2-3, 112, ura3-52, myo5-TH1Δ-13myc::URA3, myo3Δ::cgLEU2*	Lewellyn *et al.* 2015
DDY5701	*MATa his3-Δ200, leu2-3, 112, ura3-52, myo5-motorΔ-13myc::URA3, myo3Δ::cgLEU2, ABP1-mRFP::HIS3, SLA1-GFP::KanMX*	This study
DDY5702	*MATα his3-Δ200, leu2-3, 112, ura3-52, myo5-TH2Δ-13myc::URA3, myo3Δ::cgLEU2 , ABP1-mRFP::HIS3, SLA1-GFP::KanMX6*	This study
DDY5703	*MATa his3-Δ200, leu2-3, 112, ura3-52, myo5-SH3Δ-13myc::URA3, myo3Δ::cgLEU2, ABP1-mRFP::HIS3, SLA1-GFP::KanMX6*	This study
DDY5704	*MATa his3-Δ200, leu2-3, 112, ura3-52, myo5-CAΔ-13myc::URA3, myo3Δ::cgLEU2, ABP1-mRFP::HIS3, SLA1-GFP::KanMX*	This study
DDY5705	*MATa his3-Δ200, leu2-3, 112, ura3-52, myo5-motorΔTH2Δ-13myc::URA3, myo3Δ::cgLEU2, ABP1-mRFP::HIS3, SLA1-GFP::KanMX*	This study
DDY5706	*MATa his3-Δ200, leu2-3, 112, ura3-52, myo5-motorΔSH3Δ-13myc::URA3, myo3Δ::cgLEU2, ABP1-mRFP::HIS3, SLA1-GFP::KanMX*	This study
DDY5707	*MATa his3-Δ200, leu2-3, 112, ura3-52, myo5-motorΔCAΔ-13myc::URA3, myo3Δ::cgLEU2, ABP1-mRFP::HIS3, SLA1-GFP::KanMX*	This study

DDY4786	*MATa his3-Δ200, leu2-3, 112, ura3-52, myo5-TH1Δ-vrp1-13myc:URA3, myo3Δ::cgLEU2, ABP1-mRFP::HIS3, SLA1-GFP::KanMX6*	Lewellyn *et al.* 2015
DDY5708	*MATa his3-Δ200, leu2-3, 112, ura3-52, myo5-motorΔTH2Δ-vrp1-13myc::URA3, myo3Δ::cgLEU2, ABP1-mRFP::HIS3, SLA1-GFP::KanMX*	This study
DDY5709	*MATa his3-Δ200, leu2-3, 112, ura3-52, myo5-motorΔSH3Δ-vrp1-13myc::URA3, myo3Δ::cgLEU2, ABP1-mRFP::HIS3, SLA1-GFP::KanMX*	This study
DDY5710	*MATa his3-Δ200, leu2-3, 112, ura3-52, myo3Δ::cgLEU2, ABP1-mRFP::HIS3, SLA1-GFP::KanMX*	This study
DDY5711	*MATa his3-Δ200, leu2-3, 112, ura3-52, myo5Δ::URA3, myo3Δ::cgLEU2, ABP1-mRFP::HIS3, VRP1-GFP::KanMX6*	This study
DDY5712	*MATa his3-Δ200, leu2-3, 112, ura3-52, myo5-TH1Δ-GFP::URA3, myo3Δ::cgLEU2, ABP1-mRFP::HIS3*	This study

Table 2.2: Plasmids used in this study

Plasmid	Description
pDD2679	pBluescript containing *myo5-motorΔTH2Δ-13myc* marked with *URA3*
pDD2680	pBluescript containing *myo5-motorΔSH3Δ-13myc* marked with *URA3*
pDD2681	pBluescript containing *myo5-motorΔCAΔ-13myc* marked with *URA3*
pDD2682	pBluescript containing *myo5-motorΔTH2Δ-vrp1-13myc* marked with *URA3*
pDD2683	pBluescript containing *myo5-motorΔSH3Δ-vrp1-13myc* marked with *URA3*
pDD2684	pBluescript containing *myo5-motorΔCAΔ-vrp1-13myc* marked with *URA3*

Chapter 3 : Endocytic type I myosins generate force

Abstract

During clathrin-mediated endocytosis, the plasma membrane is bent into a deep pit that undergoes scission, releasing a nascent vesicle into the cytoplasm. In the budding yeast *Saccharomyces cerevisiae,* where plasma membrane deformation is opposed by turgor pressure, coat proteins such as clathrin generate insufficient force to invaginate the membrane. Similar challenges are confronted on membrane surfaces under tension in vertebrate cells. In such cases, transient assembly of a filamentous actin network provides the additional force required. Actin assembly itself is capable of generating force during clathrin-mediated endocytosis; however, clathrin-mediated endocytosis is defective in *S. cerevisiae* mutants deficient in type I myosin motor activity. How type I myosins contribute to clathrin-mediated endocytosis was not known. Previous studies on other type I myosins found that broadly some seem to be force generators while others are tension-sensitive clamps. Understanding how type I myosin functions in clathrin-mediated endocytosis requires determining whether it is a force generator or tension sensor. Here I present the first biochemical and biophysical characterization of the budding yeast type I myosin Myo5. Myo5 is a low duty ratio motor that is activated about 10-fold by heavy chain phosphorylation. Single molecule experiments indicate that Myo5 detachment kinetics from actin are not especially force sensitive. I conclude that Myo5 is well suited to generate force to assist in membrane deformation during clathrin-mediated endocytosis.

Introduction

The actin cytoskeleton is a central player in cellular morphogenesis. Cells harness forces generated by the actin cytoskeleton for processes ranging from cytokinesis to cell migration to endocytosis (Pollard and Cooper, 2009) . At least two mechanisms account for force generation by the actin cytoskeleton. First, localized assembly of actin filaments, typically nucleated by the Arp2/3 complex, can generate forces to push cellular structures, as it does at the leading edge of a migrating cell or behind motile intracellular bacteria such as *Listeria monocytogenes* (Pollard and Borisy, 2003; Loisel et al., 1999; Mogilner and Oster, 2003). Second, actin-based motors called myosins bind and move actin filaments to create contractile forces within cells (O'Connell et al., 2007). How these basic mechanisms of force generation are coordinated and integrated to create the observed diversity of actin-based morphogenic processes is of intense research interest.

Clathrin-mediated endocytosis (CME) integrates contributions from both actin assembly and myosin contraction. When the plasma membrane is under significant tension, the actin cytoskeleton is required for membrane invagination during CME (Boulant et al., 2011). The plasma membrane of the budding yeast *Saccharomyces cerevisiae* is constitutively under high tension due to turgor pressure, so all CME events in yeast are dependent on the actin cytoskeleton (Aghamohammadzadeh and Ayscough, 2009). This makes yeast a particularly useful organism for studying actin-dependent CME. A combination of genetic manipulations and live cell imaging in yeast has revealed that both actin polymerization and myosin motor activity are required for productive CME (Sun et al., 2006). Thus, CME in budding yeast represents an ideal biological process in which to study how actin polymerization and myosin contraction can cooperate.

The myosins involved in CME, including the yeast myosin Myo5, belong to the Myosin I family of motors. Type I myosins are small (~ 100 - 150 kD), monomeric, non-processive motors. They generally associate with phospholipids through a cryptic pleckstrin homology domain in the non motor "tail" portion of the protein (Coluccio, 1997; Zot et al., 1992; Hokanson et al., 2006; Feeser et al., 2010). Myosins from this family have been implicated in a variety of processes dependent on actin assembly-generated forces (Jung et al., 2001; Sokac et al., 2006; Almeida et al., 2011). Because of their conserved ability to bind phospholipids and move actin filaments, type I myosins have been widely proposed to be important links between membranes and the actin cytoskeleton (McConnell and Tyska, 2010). As membrane-cytoskeletal crosslinkers, these motor proteins are well suited to function in membrane trafficking processes such as CME.

How type I myosin motor activity contributes to the process of CME is unclear. Motor activity could serve one of at least two possible functions during CME. First, type I myosin motor activity could contribute appreciable force to assist in deforming the PM. Second, type I myosins could act as tension-sensitive anchors, coupling actin filaments to the plasma membrane or preventing reversal of the endocytic invagination process. Biophysical characterizations of type I myosins from vertebrates have uncovered remarkable diversity within this class of motors members. At least one type I myosin, mouse Myosin-1c, has contractile properties consistent with the motor being a significant force generator: its mechanochemical cycle is relatively insensitive to resistive forces, making it ideally suited to move cargos (Greenberg et al., 2012). Another closely related family member, rat Myosin-1b, is more ideally suited to behave as a tension-sensitive

anchor. Its detachment kinetics slow dramatically under resistive forces, making it unlikely to move appreciable loads (Laakso et al., 2008). Biophysical studies of the type I myosins involved in CME have not been undertaken, making it impossible to eliminate any models of motor function during endocytosis.

Here I present the first biochemical and biophysical characterization of the endocytic type I myosin Myo5. Compared to the previously mentioned myosins, Myo5 unbinds actin filaments quickly, leading to a relatively fast velocity of actin filaments in motility assays. Myo5 detachment kinetics do not slow appreciably in the presence of load, meaning that this motor is likely to be a significant force generator during CME.

Results

Unloaded kinetics of Myo5

To correlate biochemical transitions with mechanical transitions observed in single molecule experiments, I first determined rate and equilibrium constants for key steps of the Myo5 Mg^{2+}ATPase cycle (Fig. 3.1A). A Myo5 construct containing the motor and lever arm domains was purified from *S. cerevisiae*. As Myo5 is regulated by heavy chain phosphorylation, a phosphorylated version and a dephosphorylated version of the protein were purified separately (See methods, Fig. 3.1B, Bement and Mooseker, 1995). The light chain for Myo5 is the budding yeast calmodulin homologue, Cmd1 (Geli et al., 1998). Cmd1 was purified from *E. coli* and included at 2 μM in all experiments (See methods, Fig. 3.1B).

Steady-state actin-activated Mg^{2+}ATPase activity of Myo5: The steady state actin-activated Mg^{2+}ATPase activity of Myo5 is activated ~10-fold by heavy chain phosphorylation (Fig. 3.1C). Phospho-Myo5 Mg^{2+}ATPase rates fit to a rectangular hyperbola with actin concentration, indicating a V_{max} of ~3 s^{-1} and a K_m of ~3 μM (Fig. 3.1C, Table 3.1). Compared to other type I myosins, Myo5 is a slow Mg^{2+}ATPase with high affinity for actin.

Mg^{2+}ATP-induced dissociation of ActoMyo5: Light scattering was used to monitor the Mg^{2+}-induced population of the weakly actin-bound states of Myo5, as Myo5 failed to quench pyrene actin. Dissociation of actomyosin was measured at 100 nM ActoMyo5, well below the K_m, to ensure complete unbinding. Time courses of light scattering signal followed single exponential decay functions. For Phospho-Myo5, the observed rates increased linearly with Mg^{2+}ATP concentration (Fig. 3.1D). At high concentrations of Mg^{2+}ATP, the actomyosin complex was completely dissociated within the response time of the stopped-flow instrument, precluding measurement. For Dephospho-Myo5, the observed rates fit a rectangular hyperbola with increasing Mg^{2+}ATP concentration.

The mechanism of Mg^{2+}ATP-induced dissociation of actomyosin was modeled as the following three step chemical reaction:

$$AM + Mg^{2+}ATP \overset{K_1'}{\rightleftharpoons} AM(Mg^{2+}ATP) \overset{k_{+2}'}{\rightarrow} A * M(Mg^{2+}ATP) \overset{K_8}{\rightleftharpoons} A + M(Mg^{2+}ATP)$$

where AM(Mg^{2+}ATP) is the collision complex in rapid equilibrium (K_1') with free nucleotide that isomerizes (k_{+2}') to a state that dissociates from actin very rapidly (K_8). At high concentrations of Mg^{2+}ATP, formation of AM(Mg^{2+}ATP) is fast, so observed rates approximate k_{+2}'. At lower concentrations of AM(Mg^{2+}ATP), observed rates approximate $K_1'k_{+2}'$. Because observed rates of Mg^{2+}ATP-induced dissociation were unmeasurable for Phospho-Myo5 at high Mg^{2+}ATP concentrations, I was unable to determine k_{+2}', although it is greater than or equal to the fastest observed rate of 335 s^{-1} (Table 3.1). $K_1'k_{+2}'$ for Phospho-Myo5 is 0.39 $\mu M^{-1}s^{-1}$ (Table 3.1). For Dephospho-Myo5, k_{+2}' is 293 s^{-1} and $K_1'k_{+2}'$ is 1.74 (Table 3.1).

Mg^{2+}ADP dissociation from ActoMyo5: Mg^{2+}ADP dissociation from ActoMyo5 was measured through modifying the Mg^{2+}ATP-induced dissociation of ActoMyo5 experiment to report on the following reaction:

$$AM(Mg^{2+}ADP) \underset{k_{-5}'}{\overset{k_{+5}'}{\rightleftharpoons}} AM + Mg^{2+}ATP \overset{K_1'}{\rightleftharpoons} AM(Mg^{2+}ATP) \overset{k_{+2}'}{\rightarrow} A*M(Mg^{2+}ATP) \overset{K_8}{\rightleftharpoons} A + M(Mg^{2+}ATP)$$

To observe this reaction, I measured Mg^{2+}ATP-induced dissociation of 200nM ActoMyo5 in the presence of 200 μM Mg^{2+}ADP, such that the starting materials were Mg^{2+}ADP-bound ActoMyo5. Dissociation was measured at 2.5 mM Mg^{2+}ATP, beyond the measurable range of observed rates for Phospho-Myo5 and saturating concentration for Dephospho-Myo5. The observed rates in this experiment, were 74 s^{-1} for Phospho-Myo5 and 106 s^{-1} for Dephospho-Myo5 (Table 3.1). Since these rates are slower than the observed rates of Mg^{2+}ATP induced dissociation of ActoMyo5 at the same nucleotide concentration, k_{+5}' is rate limiting in this reaction. The observed rates therefore approximate k_{+5}'. Myo5 Mg^{2+}ADP release is much faster than Mg^{2+}ADP release from either Myo1b or Myo1c (Greenberg et al., 2012; Lewis et al., 2006). It is more similar to the vertebrate Myo5 homologue, Myo1e, which interestingly is also implicated in clathrin-mediated endocytosis (Mezgueldi et al., 2002).

Comparison of the kinetic mechanisms of Phospho- and Dephospho-Myo5: Dephospho-Myo5 is ~10-fold slower than Phospho-Myo5 in steady-state actin-activated Mg^{2+}ATPase experiments, but none of the measured rate or equilibrium constants revealed slowing to the same extent. Because type I myosins have unloaded Mg^{2+}ATPase rates that are limited by inorganic phosphate release, the most likely explanation for the slow actin-activated Mg^{2+}ATPase activity of Dephospho-Myo5 is slow inorganic phosphate release of the dephosphorylated enzyme. Phosphorylation state has previously been found to alter the rate of inorganic phosphate release for *Acanthameoba castellanii* type I myosins (Ostap and Pollard, 1996; Ostap et al., 2002). Because type I myosins are rate limited by inorganic phosphate release and weakly actin-bound prior to that step, they have low duty ratios, i.e. they spend the majority of their unloaded Mg^{2+}ATPase cycle unbound from actin filaments. Taken together with the slow V_{max} and assuming that inorganic phosphate release is limiting as for other type I myosins, the fast Mg^{2+}ADP release rate of Myo5 means that Phospho-Myo5 is a low duty ratio motor (~5%), with Dephospho-Myo5 having a lower duty ratio still. Thus, if heavy chain phosphorylation of Myo5 does in fact accelerate the rate of inorganic phosphate release, it also increases the duty ratio. In this way, heavy chain phosphorylation may regulate the number of myosins actively moving actin at any given moment rather than the power output of an individual myosin.

Motility of Myo5

To determine how phosphorylation affects Myo5 velocity, I performed *in vitro* motility assays with Phospho- and Dephospho-Myo5 motor/lever constructs at (Fig. 3.1B). Motility assays were performed at 1 mM Mg^{2+}ATP. At low surface densities of Myo5, motility of actin filaments was fast and lurching, likely reflecting discontinuous connection of the filaments to the Myo5-coated surface. At higher concentrations, motility was smooth at ~720 – 820 nm/s for Phospho-Myo5 (Fig. 3.1E). Much higher surface densities of

Dephospho-Myo5 were required to achieve motility, likely reflecting a lower duty ratio for the dephosphorylated motor. At high surface densities, motility was smooth at ~120 nm/s (Fig. 3.1E). Velocity of actin filaments in motility assays is equal to the step size of the myosin divided by the time the myosin spends bound to actin. At 1 mM Mg^{2+}ATP, I observed considerably slower dissociation of Dephospho-Myo5 from actin when compared with Phospho-Myo5 (~250 s^{-1} vs. ≥335 s^{-1}), possibly explaining a part of the difference in observed velocities in motility assays. Type I myosins typically exert their power stroke over two substeps, the first accompanying inorganic phosphate release upon binding to actin and the second accompanying Mg^{2+}ADP release (Veigel et al., 1999). A fraction of the slowed velocity of Dephospho-Myo5 may therefore also be accounted for by a slowing of the first, inorganic phosphate release-accompanied substep.

Single molecule characterization of Myo5

To assess the force-sensitivity of Myo5 kinetics, I performed single molecule experiments in collaboration with Serapion Pyrpassopoulos and E. Michael Ostap (University of Pennsylvania) to measure individual Myo5 interactions with actin. We used the three-bead configuration, in which a single actin filament drawn between two beads, each held in an optical trap, is lowered to a single myosin molecule on a third, stationary bead (Fig. 3.2A, Finer et al., 1994). Phospho-Myo5 was used for all single molecule experiments. We reasoned that the higher duty ratio of the phosphorylated enzyme would allow observation of more ActoMyo5 interactions. Additionally, yeast type I myosins are known to be phosphorylated *in vivo* (Attanapola et al., 2009; Grosshans et al., 2006). A cumulative frequency distribution of the attachment durations for 276 ActoMyo5 interactions was fit well by a single exponential function, indicating a uniform sample (Fig. 3.2B). The average displacement of a Myo5 binding event was 3.1 nm (Fig. 3.2C). To detect any force sensitivity of Myo5 actin unbinding kinetics, we generated a scatter plot relating the attachment duration to the average interaction force for each individual ActoMyo5 binding event (Fig. 3.2D). This plot suggests Myo5 detachment from actin is force insensitive. Short duration interactions were observed even at considerable interaction forces, contrasting sharply with rat Myo1b, for which even 1-2 pN of force dramatically extends interaction durations (Laakso et al., 2008).

Discussion

Although type I myosin activity has long been known to be critical for CME (Geli and Riezman, 1996), how these motors function during CME was not known. Current models of CME postulate that force for membrane invagination comes primarily from actin assembly (Kaksonen et al., 2006; Nickaeen et al., 2019). In this model, actin assembly factors comprising the Arp2/3 complex activators Las17 (yeast WASP) and Myo3/Myo5 working together with Vrp1 (yeast WASP interacting protein, WIP) are organized in a ring at the base of endocytic invaginations, triggering actin nucleation such that new monomers are added to endocytic actin networks near the plasma membrane (Mund et al., 2018). Actin filaments within the network are attached to the tip of endocytic invaginations by coat proteins that bind both phospholipids and filamentous actin (Skruzny et al., 2012). Growth of such an actin network creates a driving force to invaginate the membrane more deeply by facilitating extension of the length of actin filaments spanning the plasma membrane and the invagination tip. Reconstitution experiments indicate that endocytic actin networks are indeed capable of generating pushing forces (Michelot et al., 2010). Although the yeast type I myosins can activate the Arp2/3 complex to nucleate actin assembly in cooperation with Vrp1, this activity is dispensable for CME (Geli et al., 2000; Evangelista et al., 2000; Sun et al., 2006; Sirotkin et al., 2005). Motor activity, on the other hand, is critical for endocytic internalization (Lewellyn et al., 2015; Sun et al., 2006). How type I myosin motor function cooperates with actin assembly to carry out CME remains unclear.

Possible roles for type I myosin motor activity during CME depend heavily on the motors' biophysical properties. Closely related type I myosins from vertebrates, Myo1b and Myo1c, have similar enzymatic properties to one another in unloaded biochemical assays, however the load dependence of their Mg^{2+}ATPase cycle differs significantly (Lewis et al., 2006; Greenberg et al., 2012; Laakso et al., 2008; Greenberg and Ostap, 2013). Even modest resistive force slows the rate of Mg^{2+}ADP release from Myo1b significantly, meaning that Myo1b spends more time in a tightly actin-bound state, extending attachment durations under tension (Laakso et al., 2008). The rate of Mg^{2+}ADP release from Myo1c, on the other hand, is relatively force insensitive. Only under higher forces, when an isomerization step following Mg^{2+}ATP binding slows, do Myo1c attachment durations extend appreciably. These differences in force sensitivity make Myo1b more ideally suited to act as a tension sensitive anchor, while Myo1c is more likely to act as a transporter.

Here I have demonstrated that like Myo1c, Myo5 detachment from actin filaments is relatively force insensitive. This finding does not preclude a role for type I myosins in bridging the actin cytoskeleton and plasma membrane (Lewellyn et al., 2015; Pedersen and Drubin, 2019). However, given their relative force insensitivity, type I myosin motors are likely required to generate force during CME.

One intriguing possibility is that type I myosin motor activity during CME facilitates elongation of actin filaments growing against the plasma membrane. Such actin filaments are growing against a resistive load, which has been previously predicted to slow rates of actin elongation (Peskin et al., 1993). Experimental studies demonstrated that relatively modest resistive forces stall actin filament elongation completely (Footer et al., 2007). Thus, type I myosin activity may be required to reduce the load on growing actin filaments, thereby allowing for elongation. Intriguingly, a recent study has found that actin assembly rates at CME sites can be altered by varying the dosage of endocytic type I myosins

(Manenschijn et al., 2018). Previous observations have also pointed to a role for type I myosin motor activity in actin assembly, as point mutations in the *MYO5* gene can lead to an impaired "flux" of actin monomers through endocytic actin networks (Sun et al., 2006; Lewellyn et al., 2015). Actin flux through endocytic actin networks has been measured through fluorescence recovery after photobleaching experiments to be ~50 nm/s (Kaksonen et al., 2003; Okreglak and Drubin, 2007). Based on my motility assays, either Phospho- or Dephospho-Myo5 could move actin filaments at velocities faster than the observed flux rate, making it possible that myosin motor activity assists actin filament elongation.

Heavy chain phosphorylation itself may allow cells to tune how much force is provided by type I myosins during CME. By controlling the duty ratio of Myo5, heavy chain phosphorylation controls how many myosins are actively pulling actin filaments at any given time. Interestingly, the TEDS site of Myo5 has previously been shown to be phosphorylated by Ypk1, a kinase that is activated by the Target of Rapamycin Complex 2 (TORC2) upon hypotonic shock (Grosshans et al., 2006; Berchtold et al., 2012). Such osmotic shock would cause the plasma membrane to swell, presumably leading to a higher force barrier to membrane invagination during CME (Aghamohammadzadeh and Ayscough, 2009). One way that cells may overcome such elevated force requirements is through phosphorylation of Myo5 to increase the number of active motors at CME sites.

Although actin assembly-based force generation and myosin motor-based force generation have each been studied extensively, how the two modes of force generation cooperate was unclear. Here I have demonstrated that *S. cerevisiae* Myo5, a myosin required for CME, an actin assembly-based force generating process, is capable of generating force. It is now important to determine whether myosins involved in other actin assembly-based processes have similar properties.

Methods

Reagents, proteins, and buffers

Mg^{2+}ATP concentrations were determined spectrophotometrically after each experiment by absorbance at 259 nm, $\epsilon_{259} = 15{,}400\ M^{-1}cm^{-1}$. Rabbit skeletal muscle actin was prepared and gel filtered (Spudich and Watt, 1971). Actin concentrations were determined spectrophotometrically by absorbance at 290 nm, ϵ_{290} = 26,600 $M^{-1}cm^{-1}$. All actin was stabilized with one molar equivalent of phalloidin (Sigma). Steady state and transient experiments were performed at 20°C in KMg25 buffer (60 mM MOPS pH 7, 25 mM KCl, 1 mM EGTA, 1 mM $MgCl_2$, 1 mM DTT). Apyrase VII was obtained from Sigma. Purity and concentration of purified proteins were determined by comparing in-gel Coomassie blue staining to staining of known amounts of bovine serum albumin (Pierce).

Expression and Purification of Cmd1

The *S. cerevisiae* calmodulin gene *CMD1* was cloned from genomic DNA into a bacterial expression plasmid with a sequence encoding His_6-TEV situated at the 5' end to generate pRP7. pRP7 was transformed into Rosetta *E. coli*, optimized for expression (Novagen). A saturated overnight culture in LB was used to inoculate a 1L culture to OD_{600} = 0.1. Cells were grown to OD_{600} = 0.6-1, induced with 0.5 mM IPTG for 5 hours at 37°C, pelleted at 5,000 rpm for 20 minutes at 4°C, washed with cold 20 mM HEPES pH 7.5, and repelleted at 3,500 rpm for 10 minutes at 4°C in a Jouan CR3i centrifuge. Cell pellets were flash frozen in 45 mL lysis buffer (20 mM HEPES pH 7.5, 1 M KCl, 20 mM Imidazole). Upon thawing, cells were lysed by sonication, 2 mg DNase I (Roche) and triton X-100 to 1% were added, and the resulting lysate was incubated on ice for 30 minutes and spun at 30,000 rpm for 25 minutes in a 70 TI rotor. The supernatant was loaded onto a 1 mL HisTrap HP column (GE healthcare) preequilibrated with binding buffer (20 mM HEPES pH 7.5, 500 mM KCl, 20 mM imidazole). The column was washed with 20 mL binding buffer and Cmd1 was eluted over a 30 mL 0-100% gradient of elution buffer (20 mM HEPES pH 7.5, 500 mM KCl, 500 mM imidazole). Fractions containing Cmd1 were pooled, Cmd1 was cleaved from His_6 with TEV protease and dialyzed overnight at 4°C into low salt buffer (10 mM Tris pH 7, 25 mM NaCl, 2 mM $MgCl_2$, 5 mM DTT). Following dialysis, purified, cleaved Cmd1 was bound to a MonoQ column and eluted over a 10 mL 0-70% gradient of high salt buffer (10 mM Tris pH 7, 1 M NaCl, 2 mM $MgCl_2$, 5 mM DTT). Fractions containing Cmd1 were pooled, dialyzed into KMg50 buffer (60 mM MOPS pH 7, 50 mM KCl, 1 mM $MgCl_2$, 1 mM EGTA, 1 mM DTT, 5% glycerol), and stored at -80°C.

Expression and Purification of Myo5

Myo5 was coexpressed with the myosin chaperone She4 in *S. cerevisiae.* The *MYO5* open reading frame (ORF) from *S. cerevisiae* was cloned from genomic DNA and truncated at Gly^{763}, generating a construct containing the motor domain and both Cmd1-binding IQ

motifs of the lever arm. The *SHE4* ORF was cloned in its entirety from *S. cerevisiae* genomic DNA. Both ORFs were ligated into a 2μ expression plasmid with a partially defective *LEU2* gene (*leu2d*) to ensure high copy number, creating plasmid pRP8 (Roy et al., 2011). The *MYO5* ORF was situated with a sequence encoding AviTag-TEV-His_9 at the 3' end. Expression of the *MYO5* and *SHE4* ORFs was driven by a bidirectional Gal 1/10 promotor.

pRP8 was transformed into D1074 yeast (Roy et al., 2011). Saturated overnight cultures in synthetic minimal media (1.5 g/L Difacto yeast nitrogen base, 5 g/L ammonium sulfate) supplemented with 2% glucose and dropout uracil and leucine were used to inoculate 1.5 L cultures in the same media with raffinose substituted for glucose to OD_{600} = 0.1. After 18 hours of growth at 30°C, cultures were induced with 2% galactose, Bacto yeast extract was added to 10 g/L, and Bacto peptone to 20 g/L. After 8 hours of expression, the cells were harvested at 5,000 rpm for 10 minutes at 4°C in a TLA3000 rotor, washed with 25 mL cold Milli-Q water, reharvested at 3,500 rpm for 10 minutes at 4°C in a Jouan CR3i centrifuge, resuspended in 0.2 volumes of cold Milli-Q water, and drop frozen into liquid nitrogen. Lysis was achieved through cryomilling (10 cycles of 3 minutes grinding with one minute cooldown) in the large vials of a 6870 freezer/mill (SPEX Sample Prep).

Cell powders were thawed in binding buffer (10 mM Tris pH 7, 500 mM NaCl, 4 mM $MgCl_2$, 2 mM ATP, 20 mM imidazole, 5 mM DTT) supplemented with 1 mM PMSF, 1 x cOmplete protease inhibitor cocktail without EDTA (Roche), and 1 μM Cmd1. For purification of Phospho-Myo5, 1 μg Pak1 (Sigma) was included in the lysis buffer and 10 mM β-glycerophosphate, 5 mM sodium pyrophosphate, and 50 mM sodium fluoride were included in all purification buffers. For purification of Dephospho-Myo5, 4000 units lambda phosphatase (NEB) and 1 mM $MnCl_2$ were included in the lysis buffer. The lysate was then spun at 80,000 rpm for 10 minutes at 4°C in a TLA100.3 rotor, filtered through a 0.22 μm filter, and loaded onto a 1 mL HisTrap HP column. The column was washed with wash buffer (Binding buffer with only 200 mM NaCl), and eluted over a 20 mL 0-100% gradient of elution buffer (wash buffer with 1 M imidazole).

Fractions containing Myo5 were pooled and supplemented with Cmd1 to 1 μM. For Dephospho-Myo5 purification, a further 20,000 units lambda phosphatase were added along with $MnCl_2$ to 1 mM and the fractions were incubated at 30°C for 30 minutes. Purified protein was dialyzed through a 3.5 KDa MWCO membrane into 1 L storage buffer (KMg50 with 50% glycerol) overnight at 4°C and again into 500 mL of the same buffer for 2 hours at 4°C, then stored at -20°C.

Kinetic measurements

Kinetic experiments were conducted using an Applied Photophysics (Surrey, UK) SX.18 MV stopped-flow apparatus. To monitor light scattering, 450 nm excitation light was used with a 400 nm emission filter. Transients were fit to single exponentials using the software provided with the stopped flow apparatus. 1-7 traces were averaged together to generate each data point. Steady state actin-activated Mg^{2+}ATPase activity was measured using the NADH enzyme-linked assay (De La Cruz and Michael Ostap, 2009). NADH loss was monitored by absorbance at 340 nm (ϵ_{340} = 6,220 $M^{-1}cm^{-1}$). Mg^{2+}ATP-induced dissociation of ActoMyo5 was measured and analyzed as described (De La Cruz and Michael Ostap, 2009). 0.04 units/mL apyrase was added to solutions of ActoMyo5 before mixing to

remove contaminating ADP and ATP. Dephospho-ActoMyo5 required prolonged treatment with apyrase to achieve sufficient signal, presumably because a larger fraction of the population was bound to ATP left over from purification and because the actin-activated Mg^{2+}ATPase rate of Dephospho-Myo5 is slow. Concentrations reported are post mixing.

Motility assays

Motility assays were performed essentially as described (Lin et al., 2005). Myo5 was adhered to nitrocellulose coated coverslips via 20 µg anti His_6 antibody (Roche) blocked with casein. Motility was recorded in the presence of 1 mM Mg^{2+}ATP and 5 µM Cmd1. The rate of actin filament gliding was determined using the manual tracking plugin in Fiji.

Single Molecule measurements

Single molecule characterization of Myo5 was carried out essentially as described (Greenberg et al., 2012, 2017). Chambers were constructed as described for motility assays. Dumbbell beads were coated with streptavidin. Actin filaments were attached to the beads by virtue of 20% of the actin monomers being biotinylated.

Acknowledgements

Initial conditions for purifying Myo5 and Cmd1 were determined with the assistance of E. Lewellyn and A. Kunibe. This work would not have been possible without the generous collaboration of E.M. Ostap, S. Pyrpassapoulos, M.J. Greenberg, and D. Safer.

References

Aghamohammadzadeh, S., and K.R. Ayscough. 2009. Differential requirements for actin during yeast and mammalian endocytosis. *Nat. Cell Biol.* 11:1039–1042. doi:10.1038/ncb1918.

Almeida, C.G., A. Yamada, D. Tenza, D. Louvard, G. Raposo, and E. Coudrier. 2011. Myosin 1b promotes the formation of post-Golgi carriers by regulating actin assembly and membrane remodelling at the trans-Golgi network. *Nat. Cell Biol.* 13:779–789. doi:10.1038/ncb2262.

Attanapola, S.L., C.J. Alexander, and D.P. Mulvihill. 2009. Ste20-kinase-dependent TEDS-site phosphorylation modulates the dynamic localisation and endocytic function of the fission yeast class I myosin, Myo1. *J. Cell Sci.* 122:3856–61. doi:10.1242/jcs.053959.

Bement, W.M., and M.S. Mooseker. 1995. TEDS rule: A molecular rationale for differential regulation of myosins by phosphorylation of the heavy chain head. *Cell Motil. Cytoskeleton*. 31:87–92. doi:10.1002/cm.970310202.

Berchtold, D., M. Piccolis, N. Chiaruttini, I. Riezman, H. Riezman, A. Roux, T.C. Walther, and R. Loewith. 2012. Plasma membrane stress induces relocalization of Slm proteins and activation of TORC2 to promote sphingolipid synthesis. *Nat. Cell Biol.* 14:542–547. doi:10.1038/ncb2480.

Boulant, S., C. Kural, J.-C. Zeeh, F. Ubelmann, and T. Kirchhausen. 2011. Actin dynamics counteract membrane tension during clathrin-mediated endocytosis. *Nat. Cell Biol.* 13:1124–31. doi:10.1038/ncb2307.

Coluccio, L.M. 1997. Myosin I. *Am. J. Physiol.* 273:C347-59.

Evangelista, M., B.M. Klebl, A.H. Yong, B.A. Webb, T. Leeuw, E. Leberer, M. Whiteway, D.Y. Thomas, and C. Boone. 2000. A Role for Myosin-I in Actin Assembly through Interactions with Vrp1p, Bee1p, and the Arp2/3 Complex. *J. Cell Biol.* 148:353–362. doi:10.1083/jcb.148.2.353.

Feeser, E.A., C.M.G. Ignacio, M. Krendel, and E.M. Ostap. 2010. Myo1e binds anionic phospholipids with high affinity. *Biochemistry*. 49:9353–60. doi:10.1021/bi1012657.

Finer, J., R.M. Simmons, and J.A. Spudich. 1994. Single myosin muscle mechanis: piconewton forces and nanometre steps. *Nature*. 368:113–119.

Footer, M.J., J.W.J. Kerssemakers, J.A. Theriot, and M. Dogterom. 2007. Direct measurement of force generation by actin filament polymerization using an optical trap. *Proc. Natl. Acad. Sci. U. S. A.* 104:2181–6. doi:10.1073/pnas.0607052104.

Geli, M.I., R. Lombardi, B. Schmelzl, and H. Riezman. 2000. An intact SH3 domain is required for myosin I-induced actin polymerization. *EMBO J.* 19:4281–4291. doi:10.1093/emboj/19.16.4281.

Geli, M.I., and H. Riezman. 1996. Role of Type I Myosins in Receptor-Mediated Endocytosis in Yeast. *Science*. 272:533–535.

Geli, M.I., A. Wesp, and H. Riezman. 1998. Distinct functions of calmodulin are required for the uptake step of receptor-mediated endocytosis in yeast: The type I myosin Myo5p is one of the calmodulin targets. *EMBO J.* 17:635–647. doi:10.1093/emboj/17.3.635.

Greenberg, M.J., T. Lin, Y.E. Goldman, H. Shuman, and E.M. Ostap. 2012. Myosin IC generates power over a range of loads via a new tension-sensing mechanism. *Proc. Natl. Acad. Sci. U. S. A.* 109:E2433-40. doi:10.1073/pnas.1207811109.

Greenberg, M.J., and E.M. Ostap. 2013. Regulation and control of myosin-I by the motor and light chain-binding domains. *Trends Cell Biol.* 23:81–9. doi:10.1016/j.tcb.2012.10.008.
Greenberg, M.J., H. Shuman, and E.M. Ostap. 2017. Measuring the Kinetic and Mechanical Properties of Non-processive Myosins Using Optical Tweezers. *Methods Mol. Biol.* 1486:483–509. doi:10.1201/b22505.
Grosshans, B.L., H. Grötsch, D. Mukhopadhyay, I.M. Fernández, J. Pfannstiel, F.-Z. Idrissi, J. Lechner, H. Riezman, and M.I. Geli. 2006. TEDS site phosphorylation of the yeast myosins I is required for ligand-induced but not for constitutive endocytosis of the G protein-coupled receptor Ste2p. *J. Biol. Chem.* 281:11104–14. doi:10.1074/jbc.M508933200.
Hokanson, D.E., J.M. Laakso, T. Lin, D. Sept, and E.M. Ostap. 2006. Myo1c Binds Phosphoinositides through a Putative Pleckstrin Homology Domain. *Mol. Biol. Cell*. 17:4856–4865. doi:10.1091/mbc.E06.
Jung, G., K. Remmert, X. Wu, J.M. Volosky, and J. a Hammer. 2001. The Dictyostelium CARMIL protein links capping protein and the Arp2/3 complex to type I myosins through their SH3 domains. *J. Cell Biol.* 153:1479–97.
Kaksonen, M., Y. Sun, and D.G. Drubin. 2003. A pathway for association of receptors, adaptors, and actin during endocytic internalization. *Cell*. 115:475–87.
Kaksonen, M., C.P. Toret, and D.G. Drubin. 2006. Harnessing actin dynamics for clathrin-mediated endocytosis. *Nat. Rev. Mol. Cell Biol.* 7:404–414. doi:10.1038/nrm1940.
De La Cruz, E.M., and E. Michael Ostap. 2009. Kinetic and Equilibrium Analysis of the Myosin ATPase. *Methods Enzymol.* 455:157–192. doi:10.1016/S0076-6879(08)04206-7.
Laakso, J.M., J.H. Lewis, H. Shuman, and E.M. Ostap. 2008. Myosin I can act as a molecular force sensor. *Science*. 321:133–6. doi:10.1126/science.1159419.
Lewellyn, E.B., R.T.A. Pedersen, J. Hong, R. Lu, M. Huntly, and D.G. Drubin. 2015. An Engineered Minimal WASP-Myosin Fusion Protein Reveals Essential Functions for Endocytosis. *Dev. Cell*. 35:281–294. doi:10.1016/j.devcel.2015.10.007.
Lewis, J.H., T. Lin, D.E. Hokanson, and E.M. Ostap. 2006. Temperature dependence of nucleotide association and kinetic characterization of myo1b. *Biochemistry*. 45:11589–97. doi:10.1021/bi0611917.
Lin, T., N. Tang, and E.M. Ostap. 2005. Biochemical and motile properties of Myo1b splice isoforms. *J. Biol. Chem.* 280:41562–41567. doi:10.1074/jbc.M508653200.
Loisel, T.P., R. Boujemaa, D. Pantaloni, and M.F. Carlier. 1999. Reconstitution of actin-based motility of Listeria and Shigella using pure proteins. *Nature*. 401:613–616. doi:10.1038/44183.
Manenschijn, H.E., A. Picco, M. Mund, J. Ries, and M. Kaksonen. 2018. Type-I myosins promote actin polymerization to drive membrane bending in endocytosis. *bioRxiv*. 490011. doi:10.1101/490011.
McConnell, R.E., and M.J. Tyska. 2010. Leveraging the membrane - cytoskeleton interface with myosin-1. *Trends Cell Biol.* 20:418–426. doi:10.1016/j.tcb.2010.04.004.
Mezgueldi, M. El, N. Tang, S.S. Rosenfeld, and E.M. Ostap. 2002. The Kinetic Mechanism of Myo1e (Human Myosin-IC)*. *J. Biol. Chem.* 277. doi:10.1074/jbc.M200713200.
Michelot, A., M. Costanzo, A. Sarkeshik, C. Boone, J.R. Yates, and D.G. Drubin. 2010. Reconstitution and protein composition analysis of endocytic actin patches. *Curr. Biol.* 20:1890–1899. doi:10.1016/j.cub.2010.10.016.

Mogilner, A., and G. Oster. 2003. Force Generation by Actin Polymerization II: The Elastic Ratchet and Tethered Filaments. *Biophys. J.* 84:1591–1605. doi:10.1016/S0006-3495(03)74969-8.

Mund, M., J.A. Van Der Beek, J. Deschamps, S. Dmitrieff, P. Hoess, J.L. Monster, A. Picco, F. Nedelec, M. Kaksonen, and J. Ries. 2018. Systematic Nanoscale Analysis of Endocytosis Links Efficient Vesicle Formation to Patterned Actin Nucleation. *Cell*. 174:884–896. doi:10.1016/j.cell.2018.06.032.

Nickaeen, M., J. Berro, T.D. Pollard, and B.M. Slepchenko. 2019. Actin assembly produces sufficient forces for endocytosis in yeast. *Mol. Biol. Cell*. mbc.E19-01-0059. doi:10.1091/mbc.E19-01-0059.

O'Connell, C.B., M.J. Tyska, and M.S. Mooseker. 2007. Myosin at work: Motor adaptations for a variety of cellular functions. *Biochim. Biophys. Acta - Mol. Cell Res.* 1773:615–630. doi:10.1016/j.bbamcr.2006.06.012.

Okreglak, V., and D.G. Drubin. 2007. Cofilin recruitment and function during actin-mediated endocytosis dictated by actin nucleotide state. *J. Cell Biol.* 178:1251–64. doi:10.1083/jcb.200703092.

Ostap, E., T. Lin, S. Rosenfeld, and N. Tang. 2002. Mechanism of Regulation of Acanthamoeba Myosin-IC by Heavy-Chain Phosphorylation. *Biochemistry*. 1:12450–12456.

Ostap, E.M., and T.D. Pollard. 1996. Biochemical kinetic characterization of the Acanthamoeba myosin-I ATPase. *J. Cell Biol.* 132:1053–1060. doi:10.1083/jcb.132.6.1053.

Pedersen, R.T.A., and D.G. Drubin. 2019. Type I myosins anchor actin assembly to the plasma membrane during clathrin-mediated endocytosis. *J. Cell Biol.* 218:1138–1147. doi:10.1083/jcb.201810005.

Peskin, C.S., G.M. Odell, and G.F. Oster. 1993. Cellular motions and thermal fluctuations: the Brownian ratchet. *Biophys. J.* 65:316–324. doi:10.1016/S0006-3495(93)81035-X.

Pollard, T.D., and G.G. Borisy. 2003. Cellular motility driven by assembly and disassembly of actin filaments. *Cell*. 112:453–465. doi:10.1016/S0092-8674(03)00120-X.

Pollard, T.D., and J.A. Cooper. 2009. Actin, a Central Player in Cell Shape and Movement. *Science*. 326:1208–1212. doi:10.1126/science.1175862.

Roy, M.A., N. Siddiqui, and D. D'Amours. 2011. Dynamic and selective DNA-binding activity of Smc5, a core component of the Smc5-Smc6 complex. *Cell Cycle*. 10:690–700. doi:10.4161/cc.10.4.14860.

Sirotkin, V., C.C. Beltzner, J.-B. Marchand, and T.D. Pollard. 2005. Interactions of WASp, myosin-I, and verprolin with Arp2/3 complex during actin patch assembly in fission yeast. *J. Cell Biol.* 170:637–48. doi:10.1083/jcb.200502053.

Skruzny, M., T. Brach, R. Ciuffa, S. Rybina, M. Wachsmuth, and M. Kaksonen. 2012. Molecular basis for coupling the plasma membrane to the actin cytoskeleton during clathrin-mediated endocytosis. *Proc. Natl. Acad. Sci. U. S. A.* 109:E2533–E2542. doi:10.1073/pnas.1207011109.

Sokac, A.M., C. Schietroma, C.B. Gundersen, and W.M. Bement. 2006. Myosin-1c couples assembling actin to membranes to drive compensatory endocytosis. *Dev. Cell*. 11:629–40. doi:10.1016/j.devcel.2006.09.002.

Spudich, J.A., and S. Watt. 1971. The Regulation of Rabbit Skeletal Muscle Contraction. *J. Biol. Chem.* 246:4866–4871.

Sun, Y., A.C. Martin, and D.G. Drubin. 2006. Endocytic Internalization in Budding Yeast Requires Coordinated Actin Nucleation and Myosin Motor Activity. *Dev. Cell*. 11:33–46. doi:10.1016/j.devcel.2006.05.008.

Veigel, C., L.M. Coluccio, J.D. Jontes, J.C. Sparrow, R. a Milligan, and J.E. Molloy. 1999. The motor protein myosin-I produces its working stroke in two steps. *Nature*. 398:530–533. doi:10.1038/19104.

Zot, H.G., S.K. Doberstein, and T.D. Pollard. 1992. Myosin-I moves actin filaments on a phospholipid substrate: Implications for membrane targeting. *J. Cell Biol.* 116:367–376. doi:10.1083/jcb.116.2.367.

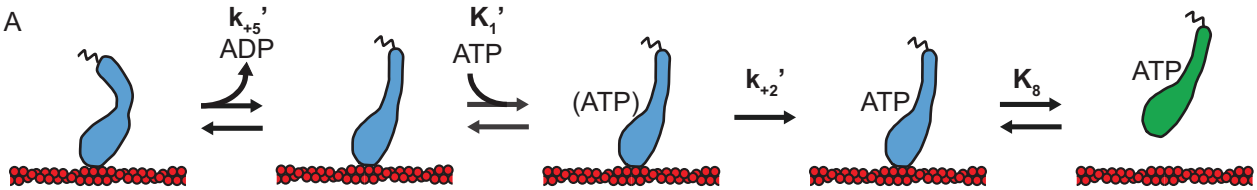
A
k_{+5}'
ADP
K_1'
ATP
(ATP)
k_{+2}'
ATP
K_8
ATP

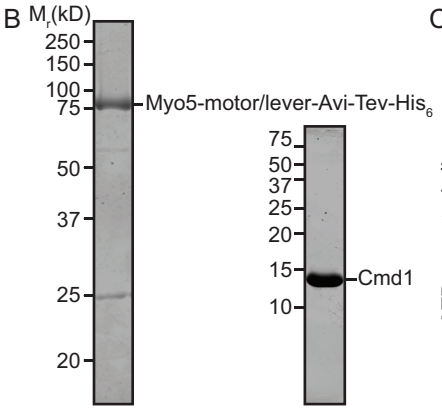
B
M_r(kD)
250
150
100
75
50
37
25
20
Myo5-motor/lever-Avi-Tev-His$_6$
75
50
37
25
20
15
10
Cmd1

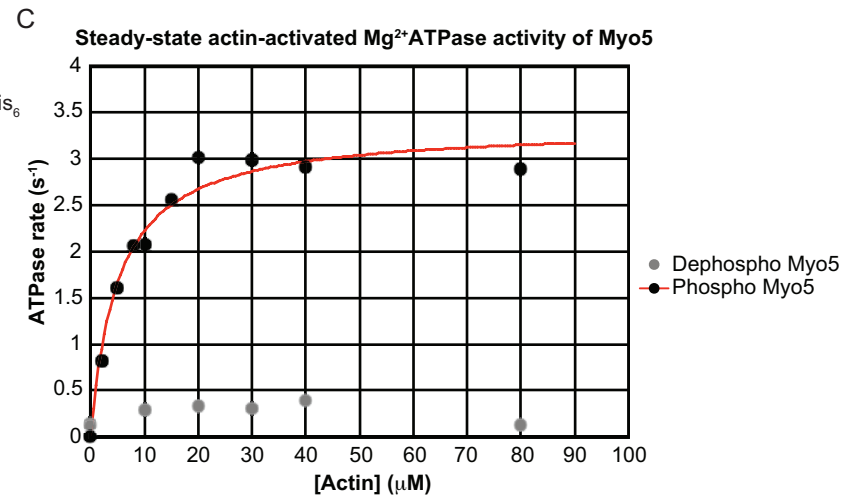
C
Steady-state actin-activated Mg²⁺ATPase activity of Myo5
ATPase rate (s⁻¹)
[Actin] (μM)
Dephospho Myo5
Phospho Myo5

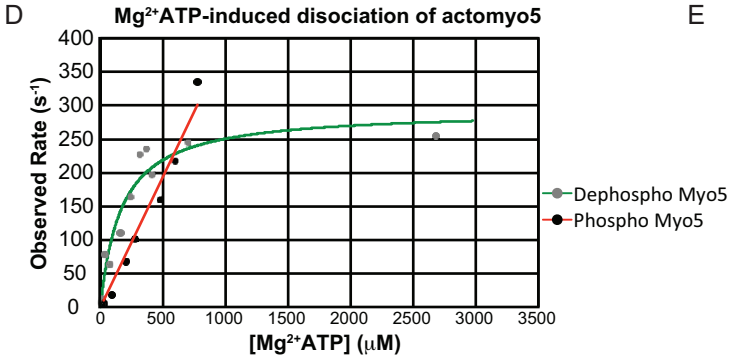
D
Mg²⁺ATP-induced disociation of actomyo5
Observed Rate (s⁻¹)
[Mg²⁺ATP] (μM)
Dephospho Myo5
Phospho Myo5

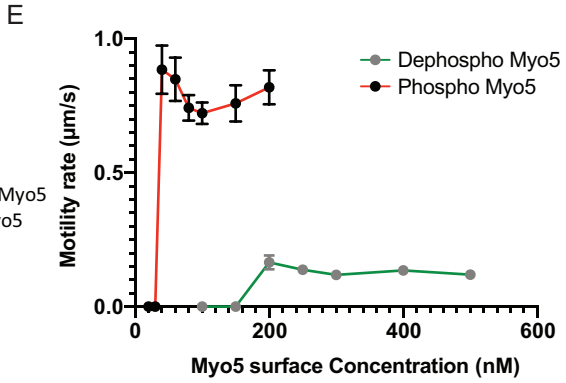
E
Motility rate (μm/s)
Myo5 surface Concentration (nM)
Dephospho Myo5
Phospho Myo5

Figure 3.1: Ensemble biochemical characterization of Myo5

(A) Schematic pathway for the relevant steps of the Myo5 Mg^{2+}ATPase cycle. Blue states represent tightly bound conformations, while the green state is weakly/unbound. (B) Coomassie-stained SDS-polyacrylamide gels showing the purified Myo5 motor/lever construct and calmodulin (Cmd1, light chain) used for biochemical characterization. (C) The actin concentration dependence of the steady-state Mg^{2+}ATPase activity of 100 nM Dephospho- (grey circles) and Phospho-Myo5 (black circles). The red line represents a best fit of the Phospho-Myo5 data to a rectangular hyperbola. (D) Mg2+ATP-induced dissociation of 100 nM Dephospho- (grey circles) and Phospho-Myo5 (black circles) was monitored by light scattering. The Mg^{2+}ATP concentration dependence of the observed rate is shown for the full range of Mg^{2+}ATP concentrations. The red line represents a linear best fit of the Phosph-Myo5 data. The green line represents a best fit of the dephospho-Myo5 data to a rectangular hyperbola.

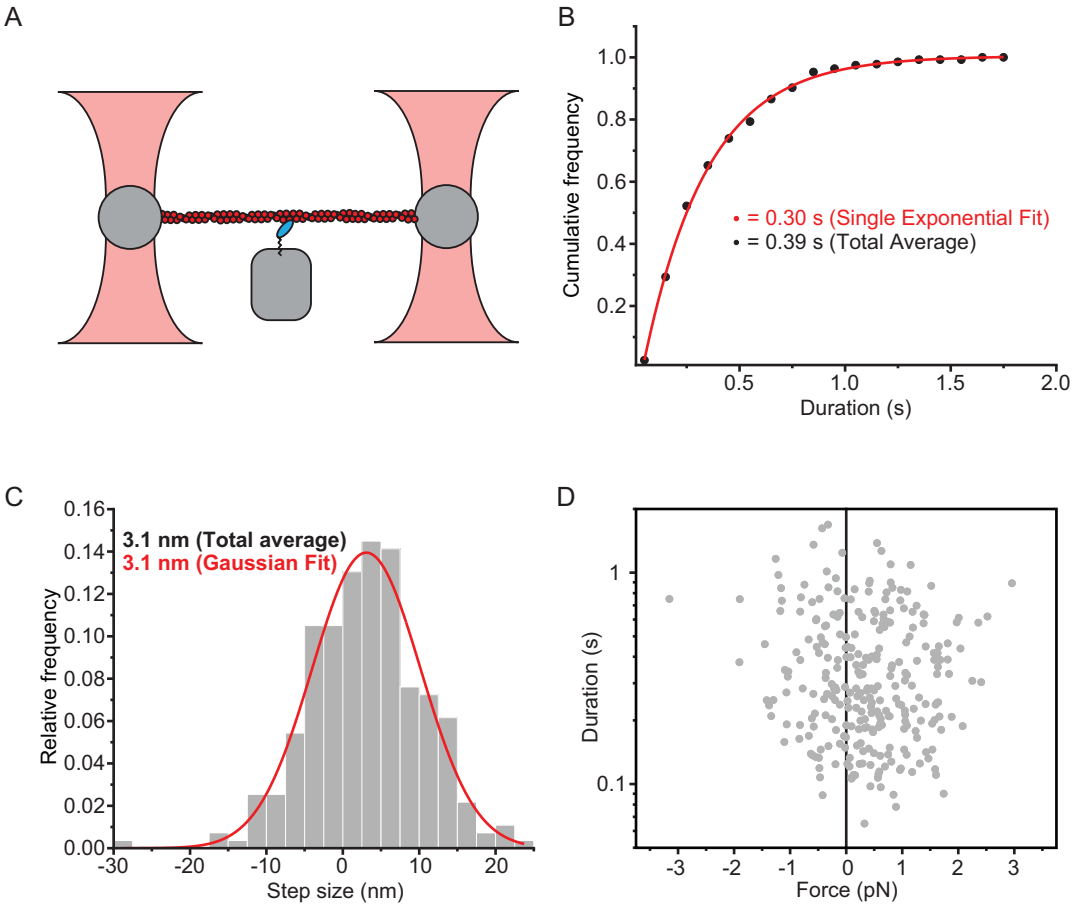
A
B
1.0
0.8
0.6
0.4
0.2
Cumulative frequency
• = 0.30 s (Single Exponential Fit)
• = 0.39 s (Total Average)
0.5
1.0
1.5
2.0
Duration (s)
C
0.16
0.14
0.12
0.10
0.08
0.06
0.04
0.02
0.00
Relative frequency
3.1 nm (Total average)
3.1 nm (Gaussian Fit)
-30
-20
-10
0
10
20
Step size (nm)
D
1
0.1
Duration (s)
-3
-2
-1
0
1
2
3
Force (pN)

Figure 3.2: Single molecule characterization of Myo5

(A) Schematic of optical trap configuration used in single molecule experiments. (B) The cumulative frequency distribution of the duration of 276 Acto-Myo5 attachment events at 1-2 μM Mg^{2+}ATP fit to a single exponential. (C) The frequency distribution of 276 Acto-Myo5 displacement events at 1-2 μM Mg^{2+}ATP fit to a single Gaussian. (D) Attachment durations of 276 Acto-Myo5 binding events plotted as a function of the average force during the attachment in the presence of 1-2 μM Mg^{2+}ATP.

Table 3.1: Rate and equilibrium constants of Myo5

	Phosphorylated Myo5	Dephosphorylated Myo5
$V_{max}(s^{-1})$	3.35	ND
K_m (μM)	5.07	ND
$K_1'k_{+2}'$ (μm^{-1} s^{-1})	0.39	1.74
k_{+2}' (s^{-1})	≥ 335	293
$k_{+5}'(s^{-1})$	74	106

Chapter 4 : Control of endocytic internalization through cargo-mediated modulation of site maturation

Abstract

Clathrin-mediated endocytosis is a highly conserved molecular pathway for generating nascent cytoplasmic vesicles from the plasma membrane, allowing cells to sample the extracellular space and internalize integral plasma membrane components. The budding yeast *Saccharomyces cerevisiae* has a well-studied clathrin-mediated endocytic pathway consisting of a variable length early phase, when endocytic sites are selected, and a more regularly timed later phase when vesicles are internalized. I noticed that the early phase was uniformly long in mothers of small-budded cells and uniformly short in mothers of large-budded cells undergoing cytokinesis. The short early phase could be induced in small-budded mothers by depolarizing the cells with osmotic shock, indicating that polarity state but not cell cycle state dictates the rate of transit through the early phase of clathrin-mediated endocytosis. Because exocytosis, likely a major route of delivery of endocytic cargos to the plasma membrane, is directed almost exclusively to the bud of small-budded cells, but is fairly uniformly distributed over the plasma membrane of large-budded cells, I propose that presence of cargo is a major determinant of the rate of maturation from the early phase of clathrin-mediated endocytosis to the later phase. This model provides a simple explanation for the long-standing observation of polarized "actin patches" or late endocytic sites: endocytic sites are initiated globally but are matured more rapidly at locations of cargo delivery.

Introduction

Endocytosis is a crucial cellular membrane trafficking processes during which the plasma membrane undergoes invagination and scission in order to generate new cytoplasmic vesicles. While numerous endocytic pathways have been described, the main route of entry into most cell types is clathrin-mediated endocytosis (CME) (Doherty and McMahon, 2009; Bitsikas et al., 2014). The budding yeast *Saccharomyces cerevisiae* is a particularly useful organism for studying the process of CME owing to the extraordinary regularity of the CME pathway in this organism. Studies in *S. cerevisiae* have demonstrated that CME relies on the coordinated recruitment of over 60 proteins responsible for selecting endocytic sites, capturing cargo, deforming the plasma membrane into a deep pit, and resolving the pit into a vesicle (Lu et al., 2016). Despite extensive knowledge of the molecular components required for this endocytic process, how progression through the pathway is regulated remains unclear.

A crucial transition occurs during budding yeast CME between site initiation and membrane internalization. CME sites are initiated by a complement of 7 known proteins and protein complexes. Ede1, Syp1, and Hrr25, known as the "early proteins," arrive at the earliest stages of CME but dissociate from CME sites prior to membrane internalization (Stimpson et al., 2009; Peng et al., 2015). Pal1, the clathrin coat complex, and the AP2 and AP180 adapter complex homologues, known at the "early coat proteins" arrive at around the same time, but remain at endocytic sites and internalize with other, later arriving coat components (Carroll et al., 2012, 2009; Newpher et al., 2005; Kaksonen et al., 2005). While the later stages of CME occur with rapid (~30 s) and regular kinetics, these early arriving CME proteins exhibit long, variable (from < 1 minute to > 4 minute) residence times at endocytic sites (Carroll et al., 2012; Stimpson et al., 2009; Newpher et al., 2005; Kaksonen et al., 2005). The identities of the factors influencing the transition from this long, variable, early phase to the more regular later phase of CME are unknown.

While the source of early and early coat protein lifetime variability is not known, the length of their lifetimes at endocytic sites appears to be roughly anti correlated with the presence endocytic cargo. In small-budded cells, the majority of exocytic traffic is directed toward the bud (Field and Schekman, 1980). Endocytic cargos such as vesicle-SNARE proteins must be retrieved from the plasma membrane after exocytosis (Lewis et al., 2000). Because septin filaments at the bud neck prevent lateral diffusion between the mother and the bud, the polarized pattern of secretion in small-budded yeast cells is presumed to concentrate cargo in the bud (Takizawa et al., 2000). Ede1 lifetimes are shorter in the buds of small-budded cells, demonstrating a correlation between abundance of endocytic cargo and abbreviated Ede1 lifetime (Layton et al., 2011). Conversely, when delivery of endocytic cargo to the plasma membrane is blocked by use of temperature sensitive secretion mutants, Ede1 lifetimes increase (Carroll et al., 2012). These results suggest that the presence of cargo at CME sites may shorten the early phase of the process.

I set out to determine how progression from the early stage of CME to the later stage is regulated. Using natural cycles of polarization and depolarization that accompany the budding yeast cell cycle along with triggered depolarization by osmotic shock, I tested whether sites of exocytosis correspond to locations where transit through the early phase of endocytosis is fast. By analyzing early phase and late phase CME markers in the mother cells of polarized and depolarized cells, I determined that a substantial portion of the

variability in early arriving protein lifetimes can be explained by polarization state. When exocytosis is mainly occurring away from the mother cell cortex, early protein lifetimes are uniformly long and less variable in duration, indicating a slow maturation rate of CME sites. However, when exocytosis was redirected toward the mother cell cortex, either naturally as a cell progressed through the cell cycle or through forced depolarization, the lifetime profile of early arriving CME proteins was starkly different: they exhibit short lifetimes, indicating a fast maturation rate. Together, these data indicate that one way in which the cell controls where endocytosis occurs is through modulating the maturation rate of pre-existing endocytic sites.

Results and Discussion

To reconcile observations of both regular and irregular behavior in the CME pathway, I considered the hypothesis that the presence of cargo influences the rate of transition from the earliest stages of CME to the more regular, later stages. Layton et al. (Layton et al., 2011) reported shorter Ede1 lifetimes in buds of highly polarized *S. cerevisiae* cells in comparison to mothers, but similar Ede1 lifetimes in mothers and buds of depolarized cells. They concluded that endocytic cargo, delivered by exocytosis to sites of polarization, influences endocytic maturation. To exclude the possibility that variability in early protein behavior is due to cell-to-cell variability, I imaged Ede1-GFP, a marker for the early phase of CME, and Sla1-mCherry, a marker for a later, more regular phase, in individual cells through the cell cycle. As *S. cerevisiae* cells progress through the cell cycle, they undergo a cycle of polarization and depolarization (Lew and Reed, 1993). In the small- and medium-budded stages of the cell cycle, when exocytosis is directed primarily to the bud (Field and Schekman, 1980), I observed extensive polarization of late, Sla1-mCherry-marked CME sites without coincident polarization of early, Ede1-GFP-marked sites (Fig. 4.1A). This disparity diminished as cells entered cytokinesis, during which exocytosis is depolarized along the mother-bud axis and is directed largely toward the bud neck, likely leading to a more uniform distribution of cargo. Polarization of late CME sites, but not early ones, reestablished as cells began polarizing for the next cell cycle (Fig. 4.1A). This result indicates that the process of CME initiation is considerably less polarized than the process of CME maturation.

I considered two possible explanations for the overabundance of early CME sites in highly polarized mothers compared to late sites, as evidenced by the presence of Ede1 but not Sla1. First, excess of sites marked only by Ede1 could represent CME sites that are initiated but aborted in the absence of cargo. Second, the sites could represent CME sites that are initiated but waiting for cargo to trigger their maturation to the late stage of the pathway. To distinguish between these possibilities, I imaged Ede1-GFP Sla1-mCherry cells using a two-step imaging protocol. First, I collected 5 μm z-stacks (11 slices, 500 nm each) to identify highly polarized and depolarized cells, defined operationally as small-budded cells with 3 or fewer Sla1-mCherry-marked late CME sites in the mother, and medium- or large-budded cells with greater than 3 Sla1-mCherry-marked late CME sites in the mother, respectively (Fig. 4.1B). Quantification of the ratio of late CME sites to early sites in these cells confirmed my observation of more early than late sites in mothers of small-budded cells (Fig. 4.1C). Next, I collected single focal plane time series of the same cells for 4 minutes with an interval of 2 seconds between frames and generated circumferential kymographs along the mother cortex (Fig. 4.1B). The kymographs failed to reveal abortive early CME sites since every Ede1-GFP track that ended in the 4-minute movie was punctuated by Sla1-mCherry signal (Fig. 4.1B). While I could not reliably extract Ede1 lifetimes due to a large fraction of Ede1 puncta being present at the start and end of my movies, I observed more long-lived Ede1-marked early CME sites in kymographs from mothers of highly polarized cells than from depolarized cells (Fig. 4.1B and D). When I conducted the same kinds of experiments with two late makers of CME, Sla1-GFP and Abp1-mRFP, neither the ratio of puncta nor the lifetimes of these proteins were sensitive to cell polarization state (Fig. 4.2A-C). Based on these observations, I conclude that the presence of cargo accelerates the rate of maturation from the early, variable stages of CME

to the later, more regular stages. Consistent with this interpretation, puncta of other early arriving CME proteins were similarly less polarized compared to Sla1-mCherry puncta in small- and medium-budded cells (Fig 4.2D and E).

To exclude the possibility that these observed differences in CME site maturation are due to cell cycle signaling pathways, I used osmotic shock to reposition CME cargo independent of cell cycle state. A previous study from our lab used a temperature sensitive secretion mutant to halt accumulation of endocytic cargo on the plasma membrane and reported increased numbers of long-lived Ede1-GFP-marked CME sites (Carroll et al., 2012). I conducted the converse experiment by adding endocytic cargo to the plasma membrane of highly polarized mothers, where early CME sites are long-lived, most likely due to cargo paucity. Diluting *S. cerevisiae* cells out of media has previously been reported to trigger depolarization (Pringle et al., 1989). I found that osmotically shocking highly polarized cells by rapidly diluting them with water caused depolarization of the polarity marker Bem1-GFP (Fig. 4.1E and F). Depolarization also resulted in redistribution of GFP-Sec4 marked secretory vesicles from a bud-localized distribution to a more uniform one, suggesting that exocytic traffic (and therefore endocytic cargo) is repositioned by this manipulation (Fig 4.2F). When I examined the CME markers Ede1-GFP and Sla1-mCherry, I found that osmotic shock caused Sla1-mCherry sites to depolarize in small-budded cells (Fig. 4.1G). Ede1-GFP sites were not noticeably affected (Fig. 4.1G). Quantification of the ratio of late phase CME sites to early phase sites in these cells revealed a transition reminiscent of the one that occurs naturally during the cell cycle (Fig. 4.1H, also see Fig 4.1C). To determine whether this transition was caused by a change in the maturation rate of CME sites, I examined Ede1-GFP tracks in kymographs made from cells before and after osmotic shock. I observed a decrease in the proportion of long-lived early CME sites upon osmotic shock, suggesting that early phase CME sites mature to the later, regular phase more quickly (Fig. 4.1I). Interestingly, the apparent shortening of Ede1-GFP lifetimes by osmotic shock did not extend to late CME proteins. While the ratio of Abp1-mRFP: Sla1-GFP puncta was unchanged, both Sla1-GFP and Abp1-mRFP lifetimes were in fact significantly increased upon osmotic shock (Fig. 4.2G-J). Lengthening of Sla1-GFP and Abp1-mRFP lifetimes is likely due to a mechanical burden on membrane invagination/internalization caused by increased turgor pressure in hypotonic solution (Hassinger et al., 2017; Aghamohammadzadeh and Ayscough, 2009). Thus, the addition of cargo increases the rate of CME site maturation from the early stages, even as the rate of internalization is slowed.

Together, my data indicate that part of the observed variability in the lifetimes of early arriving CME proteins can be explained by the availability of cargo. In the absence of cargo, the transition from the early, variable phase of CME to the more regular phase is slow, resulting in long lifetimes of early CME proteins. When cargo is present, this transition is accelerated, resulting in short lifetimes of early CME proteins. Because endocytic cargos are delivered to the plasma membrane in a polarized manner by exocytosis, the increased rate of CME site maturation in the presence of cargo provides an explanation for the polarization of actin patches in small- and medium-sized buds (Adams and Pringle, 1984).

Methods

Strains and yeast husbandry

All budding yeast strains were derived from the wild-type diploid DDY1102 and propagated using standard techniques (Amberg et al., 2005). C-terminal fluorescent protein fusions were originally constructed as described previously (Longtine et al., 1998). The strains used in this study are listed in table 4.1.

Live cell imaging

Cells were grown to mid log phase in imaging media (synthetic minimal media supplemented with Adenine, L-Histidine, L-Lucine, L-Lysine, L-Methionine, Uracil, and 2% glucose), then adhered to coverslips coated with 0.2 mg/ml Concanavalin A.

Epifluorescence imaging was carried out on a Nikon Eclipse Ti inverted microscope with a Nikon 100x 1.4 numerical aperture (NA) Plan Apo VC oil immersion objective and an Andor Neo 5.5 sCMOS camera. GFP and mCherry fluorescence were excited using a Lumencore Spectra X LED light source with 550/15 nm and 470/22 nm excitation filters. For two-color imaging, channels were acquired sequentially using an FF-493/574-Di01 dual pass dichroic mirror and FF01-524/628-25 dual pass emission filters (Semrock, Rochester, NY). The system was controlled with Nikon Elements software and maintained at 25°C by an environmental chamber (In Vivo Scientific, St. Louis, MO).

Spinning disc confocal microscopy was carried on a Nikon Eclipse Ti inverted microscope with a Nikon 100x 1.45 NA Plan Apo λ oil immersion objective, an Andor IXon X3 EM-CCD camera and Andor CSU-X spinning disc confocal equipment. GFP fluorescence was excited using a 488 nm laser and detected with a Chroma 535/20 nm emission filter (Bellows Falls, VT). mCherry fluorescence was excited using a 565 nm laser and detected with a Chroma 605/52 nm emission filter. The system was controlled with Nikon Elements software. Imaging was conducted at room temperature (~23°C).

Osmotic shock experiments

For osmotic shock experiments, cells were adhered to Concanavalin A coated coverslips for for live cell imaging, but overlaid with only 250 μL imaging media. Osmotic shock was achieved through rapid addition of 4 mL of sterile water or 4 mL imaging media as a control.

Image analysis and figure preparation

All image analysis was carried out using Fiji software (National Institutes of Health, Bethesda, MD). For quantification of Ede1-GFP turnover, circumferential kymographs were generated by drawing a line of width 5 pixels around the circumference of each cell. For

quantification of Sla1-GFP and Abp1-mRFP patch lifetimes, radial kymographs were generated using a custom Fiji macro that generates a kymograph at every radius around a circle in 2-degree increments. The lifetimes of the first 5 kymographs generated were measured to avoid bias. For intensity profile analysis of Bem1-GFP, intensity profiles were normalized to cell length and averaged using a Fiji plugin provided by C. Brownlee (Brownlee and Heald, 2019). Exact numbers of cells and CME sites measured are described in the figure legends.

For figure panels and movies, individual cells were cropped, background fluorescence was uniformly subtracted from the image stack, and photo bleaching was fit to a linear decay function and corrected using a custom Fiji macro. Look up tables used for display are linear. Figures were assembled in Adobe illustrator Creative Cloud 2019.

Statistics and Reproducibility of experiments

All experimental results presented were replicated in at least three distinct experiments to ensure reproducibility. For imaging experiments, multiple cells from each replicate were analyzed. As data from different days were indistinguishable, they were pooled for statistical analysis. The specific number of cells analyzed is indicated in each figure legend. Statistical analysis was conducted in Prism 8 (GraphPad Software, San Diego, CA).

Acknowledgements

I thank J. Hassinger, my trusted friend, colleague, and my all-time favorite collaborator. Further exploration of the CME transition point including a quantitative description can be found in his dissertation. Spinning disc confocal microscopy was conducted at the University of California, Berkeley Cancer Research Laboratory Molecular Imaging center, supported by the Gordon and Betty Moore foundation. I would like to thank H. Aaron and F. Ives for their microscopy training and assistance.

References

Adams, A.E., and J.R. Pringle. 1984. Relationship of actin and tubulin distribution to bud growth in wild- type and morphogenetic-mutant Saccharomyces cerevisiae. *J. Cell Biol.* 98:934–945. doi:10.1083/jcb.98.3.934.

Aghamohammadzadeh, S., and K.R. Ayscough. 2009. Differential requirements for actin during yeast and mammalian endocytosis. *Nat. Cell Biol.* 11:1039–1042. doi:10.1038/ncb1918.

Amberg, D.C., D.J. Burke, and J.N. Strathern. 2005. Methods in Yeast Genetics: A Cold Spring Harbor Laboratory Course Manual, 2005 Edition. 205 pp.

Bitsikas, V., I.R. Corrêa, and B.J. Nichols. 2014. Clathrin-independent pathways do not contribute significantly to endocytic flux. *Elife*. 3:1–26. doi:10.7554/elife.03970.

Brownlee, C., and R. Heald. 2019. Importin α Partitioning to the Plasma Membrane Regulates Intracellular Scaling. *Cell*. 176:805-815.e8. doi:10.1016/j.cell.2018.12.001.

Carroll, S.Y., H.E.M. Stimpson, J. Weinberg, C.P. Toret, Y. Sun, and D.G. Drubin. 2012. Analysis of yeast endocytic site formation and maturation through a regulatory transition point. *Mol. Biol. Cell*. 23:657–668. doi:10.1091/mbc.E11-02-0108.

Carroll, S.Y., P.C. Stirling, H.E.M. Stimpson, E. Gießelmann, M.J. Schmitt, and D.G. Drubin. 2009. A Yeast Killer Toxin Screen Provides Insights into A/B Toxin Entry, Trafficking, and Killing Mechanisms. *Dev. Cell*. 17:552–560. doi:10.1016/j.devcel.2009.08.006.

Doherty, G.J., and H.T. McMahon. 2009. Mechanisms of endocytosis. *Annu. Rev. Biochem.* 78:857–902. doi:10.1146/annurev.biochem.78.081307.110540.

Donovan, K.W., and a. Bretscher. 2015. Tracking individual secretory vesicles during exocytosis reveals an ordered and regulated process. *J. Cell Biol.* 1–14. doi:10.1083/jcb.201501118.

Field, C., and R. Schekman. 1980. Localized secretion of acid phosphatase reflects the pattern of cell surface growth in saccharomyces cerevisiae. *J. Cell Biol.* 86:123–128. doi:10.1083/jcb.86.1.123.

Hassinger, J.E., G. Oster, D.G. Drubin, and P. Rangamani. 2017. Design principles for robust vesiculation in clathrin-mediated endocytosis. *Proc. Natl. Acad. Sci. U. S. A.* 114:E1118–E1127. doi:10.1073/pnas.1617705114.

Kaksonen, M., C.P. Toret, and D.G. Drubin. 2005. A modular design for the clathrin- and actin-mediated endocytosis machinery. *Cell*. 123:305–20. doi:10.1016/j.cell.2005.09.024.

Layton, A.T., N.S. Savage, A.S. Howell, S.Y. Carroll, D.G. Drubin, and D.J. Lew. 2011. Modeling vesicle traffic reveals unexpected consequences for Cdc42p-mediated polarity establishment. *Curr. Biol.* 21:184–194. doi:10.1016/j.cub.2011.01.012.

Lew, D.J., and S.I. Reed. 1993. Morphogenesis in the yeast cell cycle: regulation by Cdc28 and cyclins. *J. Cell Biol.* 120:1305–1320. doi:10.1083/jcb.120.6.1305.

Lewis, M.J., B.J. Nichols, C. Prescianotto-Baschong, H. Riezman, and H.R.B. Pelham. 2000. Specific Retrieval of the Exocytic SNARE Snc1p from Early Yeast Endosomes. *Mol. Biol. Cell*. 11:23–38. doi:10.1091/mbc.11.1.23.

Longtine, M.S., a McKenzie, D.J. Demarini, N.G. Shah, a Wach, a Brachat, P. Philippsen, and J.R. Pringle. 1998. Additional modules for versatile and economical PCR-based gene deletion and modification in Saccharomyces cerevisiae. *Yeast*. 14:953–61. doi:10.1002/(SICI)1097-0061(199807)14:10<953::AID-YEA293>3.0.CO;2-U.

Lu, R., D.G. Drubin, and Y. Sun. 2016. Clathrin-mediated endocytosis in budding yeast at a glance. *J. Cell Sci.* 129:1531–1536. doi:10.1242/jcs.182303.

Newpher, T.M., R.P. Smith, V. Lemmon, and S.K. Lemmon. 2005. In vivo dynamics of clathrin and its adaptor-dependent recruitment to the actin-based endocytic machinery in yeast. *Dev. Cell*. 9:87–98. doi:10.1016/j.devcel.2005.04.014.

Peng, Y., A. Grassart, R. Lu, C.C.L. Wong, J. Yates, G. Barnes, and D.G. Drubin. 2015. Casein Kinase 1 Promotes Initiation of Clathrin-Mediated Endocytosis. *Dev. Cell*. 32:231–240. doi:10.1016/j.devcel.2014.11.014.

Pringle, J.R., R.A. Preston, A.E.M. Adams, T. Stearns, D.G. Drubin, B.K. Haarer, and E.W. Jones. 1989. Fluorescence Microscopy Methods for Yeast. *Methods Cell Biol.* 31:357–435. doi:10.1016/S0091-679X(08)61620-9.

Stimpson, H.E.M., C.P. Toret, A.T. Cheng, B.S. Pauly, and D.G. Drubin. 2009. Early-Arriving Syp1p and Ede1p Function in Endocytic Site Placement and Formation in Budding Yeast. *Mol. Biol. Cell*. 20:4640–4651. doi:10.1091/mbc.E09.

Takizawa, P.A., J.L. Derisi, J.E. Wilhelm, and R.D. Vale. 2000. Plasma Membrane Compartmentalization in Yeast by Messenger RNA Transport and a Septin Diffusion Barrier. *Science*. 290:341–344. doi:10.1126/science.290.5490.341.

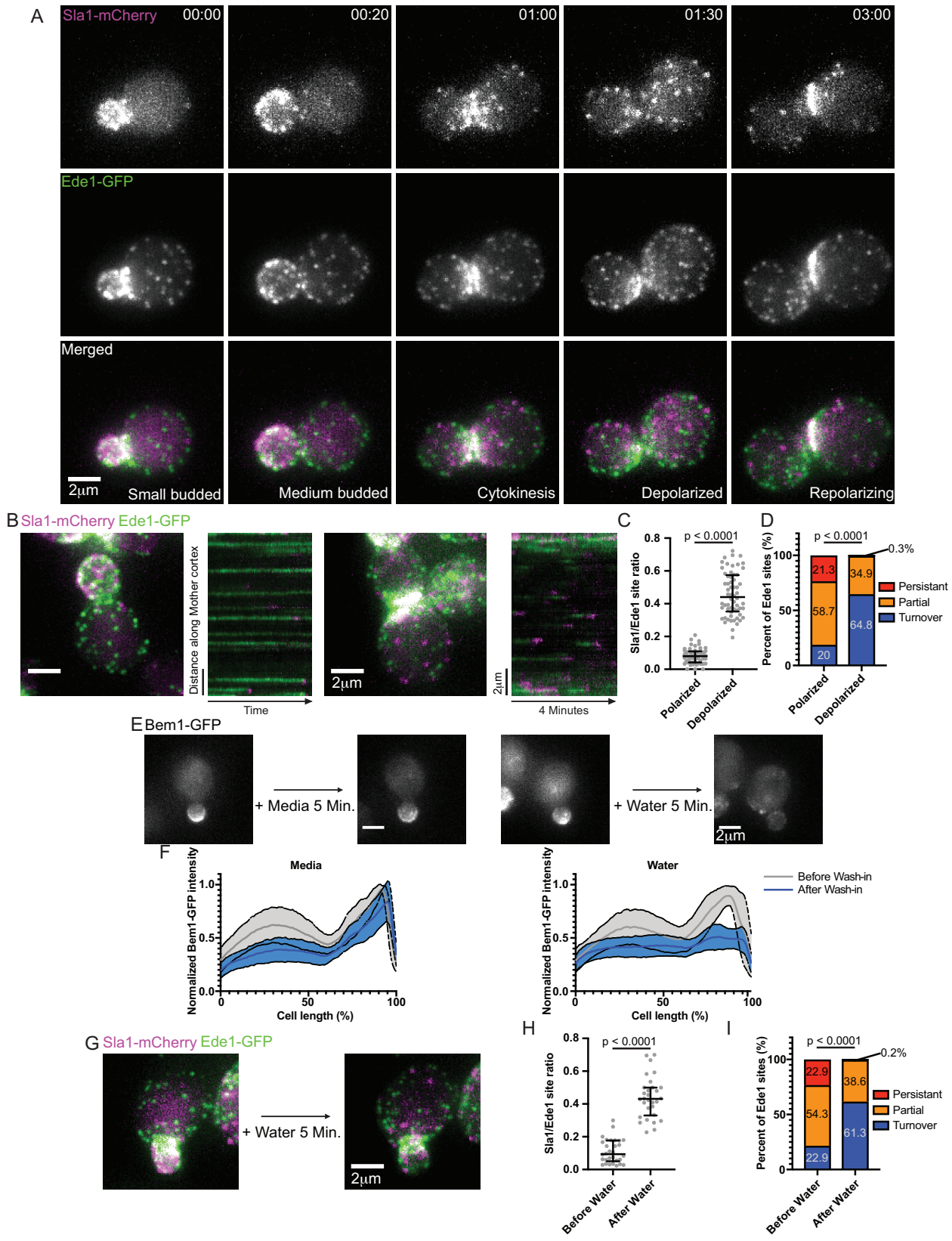
A
Sla1-mCherry
00:00
00:20
01:00
01:30
03:00
Ede1-GFP
Merged
2μm
Small budded
Medium budded
Cytokinesis
Depolarized
Repolarizing
B Sla1-mCherry Ede1-GFP
Distance along Mother cortex
Time
2μm
2μm
4 Minutes
C
p < 0.0001
Sla1/Ede1 site ratio
Polarized
Depolarized
D
p < 0.0001
0.3%
Percent of Ede1 sites (%)
21.3
58.7
20
34.9
64.8
Persistant
Partial
Turnover
Polarized
Depolarized
E Bem1-GFP
+ Media 5 Min.
+ Water 5 Min.
2μm
F
Media
Water
Normalized Bem1-GFP intensity
Cell length (%)
Before Wash-in
After Wash-in
G Sla1-mCherry Ede1-GFP
+ Water 5 Min.
2μm
H
p < 0.0001
Sla1/Ede1 site ratio
Before Water
After Water
I
p < 0.0001
0.2%
Percent of Ede1 sites (%)
22.9
54.3
22.9
38.6
61.3
Persistant
Partial
Turnover
Before Water
After Water

Figure 4.1: Cargo influences the rate of endocytic site maturation.

(A) Montage from a maximum intensity-projected epifluorescence video of a cell expressing Sla1-mCherry (magenta) and Ede1-GFP (Green). Times are minutes:seconds. (B) Maximum intensity projections of z-stacks (left) of polarized and depolarized cells paired with circumferential kymographs around the mother cortex from medial focal plane videos of the same cells (right) expressing Sla1-mCherry (magenta) and Ede1-GFP (Green). (C) Quantification of the ratio of Sla1-mCherry to Ede1-GFP sites in mother cells from maximum intensity projections of z-stacks of 60 polarized and 60 depolarized cells. A two-tailed p value from a Mann-Whitney U test with the null hypothesis that the two ratios are identical (U = 1) is displayed. The median and interquartile ranges are denoted with error bars. (D) Percentage of 596 Ede1 patches from 59 polarized mother cells and 1034 Ede1 patches from 56 depolarized mother cells that persist throughout the duration of a 4-minute video (persistent), that are present at the start or end of the video (partial), or that assemble and disassemble within the interval of the video (turnover). Numbers indicate the percentage of patches observed in each category. A two-tailed p value from a Chi-Square test with the null hypothesis that the proportion distributions are identical (chi-square = 1349, 2 degrees of freedom) is displayed. (E) Maximum intensity projections of cells endogenously expressing polarity marker Bem1-GFP before and 5 minutes after 17-fold dilution into imaging media (left) or water (right). (F) Average ± standard deviation for Bem1-GFP intensity profiles from 20 (media, left) and 30 (water, right) cells before and after dilution into the indicated media. Individual intensity profiles generated from 25 pixel wide lines were normalized to the maximum value before dilution and to cell length. (G) Maximum intensity projections of a cell endogenously expressing Sla1-mCherry (magenta) and Ede1-GFP (green) before and 5 minutes after 17-fold dilution into water. (H) Quantification of the ratio of Sla1-mCherry to Ede1-GFP sites from maximum intensity projections of z-stacks of 30 mother cells before and after osmotic shock. A two-tailed p value from a Mann-Whitney U test with the null hypothesis that the two ratios are identical (U = 7) is displayed. The median and interquartile ranges are denoted with error bars. (I) Percentage of Ede1 patches in 30 mother cells before and after osmotic shock that persist throughout the duration of a 4-minute video (persistent), are present at the start or end of the video (partial), or assemble and disassemble within the interval of the video (turnover). Numbers indicate the percentage of patches observed in each category. A two-tailed p value from a Chi-Square test with the null hypothesis that the proportions of distributions are identical (chi-square = 543.1, 2 degrees of freedom) is displayed.

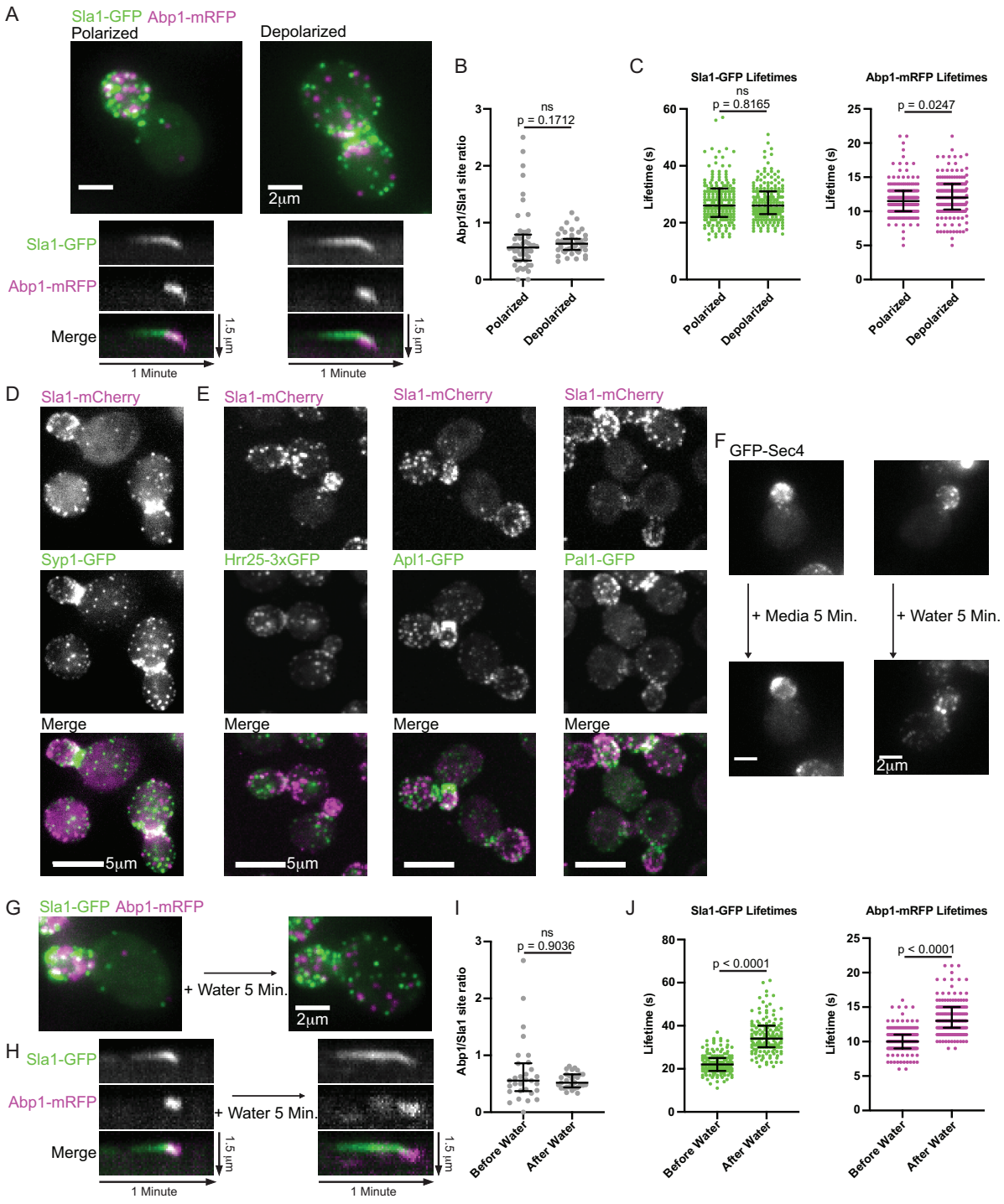
A
Sla1-GFP Abp1-mRFP
Polarized
Depolarized
2μm
Sla1-GFP
Abp1-mRFP
Merge
1.5 μm
1 Minute
B
Abp1/Sla1 site ratio
ns
p = 0.1712
Polarized
Depolarized
C
Sla1-GFP Lifetimes
ns
p = 0.8165
Abp1-mRFP Lifetimes
p = 0.0247
Lifetime (s)
D
Sla1-mCherry
Syp1-GFP
Merge
5μm
E
Sla1-mCherry
Hrr25-3xGFP
Apl1-GFP
Pal1-GFP
F
GFP-Sec4
+ Media 5 Min.
+ Water 5 Min.
2μm
G
Sla1-GFP Abp1-mRFP
+ Water 5 Min.
H
I
ns
p = 0.9036
Before Water
After Water
J
p < 0.0001

Figure 4.2: Cargo does not influence the rate of late steps in the endocytic pathway.

(A) Maximum intensity projections of z-stacks (top) of polarized and depolarized cells paired with radial kymographs of individual endocytic events from medial focal plane videos of the same cells (bottom) expressing Sla1-GFP (green) and Abp1-mRFP (magenta). (B) Quantification of the ratio of Abp1-mRFP to Sla1-GFP sites from maximum intensity projections of z-stacks of 50 polarized and 50 depolarized cells. A two-tailed p value from a Mann-Whitney U test with the null hypothesis that the two ratios are identical (U = 1051) is displayed. The median and interquartile ranges are denoted with error bars. (C) Sla1-GFP and Abp1-mRFP lifetimes measured in 40 polarized cells and 40 depolarized cells (5 representative sites per cell). Two-tailed p values from Mann-Whitney U tests (U_{Sla1} = 19732, U_{Abp1} = 17429) with the null hypothesis that the lifetimes are identical are displayed. The median and interquartile ranges are denoted with error bars. (D) Maximum intensity projection of an epifluorescence z-stack of a cluster of cells expressing Sla1-mCherry (magenta) and Syp1-GFP (green). (E) Maximum intensity projections of a spinning disc confocal z-stack of a cluster of cells expressing Sla1-mCherry (magenta) and Hrr25-3xGFP (green, left), Apl1-GFP (green, middle), or Pal1-GFP (green, right). (F) Maximum intensity projections of cells endogenously expressing GFP-Sec4 before and 5 minutes after 17-fold dilution into imaging media (left) or water (right). (G) Maximum intensity projections of a cell endogenously expressing Sla1-GFP (Green) and Abp1-mRFP (magenta) before and 5 minutes after 17-fold dilution into water. (H) Radial kymographs of individual endocytic events from medial focal plane videos of cells expressing Sla1-GFP (green) and Abp1-mRFP (magenta) before and 5 minutes after 17-fold dilution into water. (I) Quantification of the ratio of Abp1-mRFP to Sla1-GFP sites from maximum intensity projections of z-stacks of 30 cells before and after osmotic shock. A two-tailed p value from a Mann-Whitney U test with the null hypothesis that the two ratios are identical (U = 441.5) is displayed. The median and interquartile ranges are denoted with error bars. (J) Sla1-GFP and Abp1-mRFP lifetimes measured in 30 cells prior to osmotic shock and 30 cells after osmotic shock (5 representative sites per cell). Two-tailed p values from Mann-Whiney U tests with the null hypothesis that the lifetimes are identical (U_{Sla1} = 1678, U_{Abp1} = 2998) are displayed. The median and interquartile ranges are denoted with error bars.

Table 4.1: Strains used in this study

Name	Genotype	Source
DDY1102	*MATa/MATα his3-Δ200/his3-Δ200, leu2-3, 112/leu2-3, 112, ura3-52/ura3-52, ade2-1/ADE2, lys2-801/LYS2*	Drubin Lab
RPY49.1	*MATa his3-Δ200, leu2-3, 112, ura3-52, ABP1-mRFP::HIS3, SLA1-GFP::KanMX*	This study
RPY347.1	*MATa his3-Δ200, leu2-3, 112, ura3-52, bar1Δ::NatR, SLA1-mCherry::HIS3, PAL1-GFP::HIS3*	This study
RPY351.1	*MATa his3-Δ200, leu2-3, 112, ura3-52, bar1Δ::NatR, SLA1-mCherry::HIS3, APL1-GFP::HIS3*	This study
RPY353.1	*MATa his3-Δ200, leu2-3, 112, ura3-52, bar1Δ::NatR, SLA1-mCherry::HIS3, EDE1-GFP::HIS3*	This study
RPY355.1	*MATa his3-Δ200, leu2-3, 112, ura3-52, bar1Δ::NatR, SLA1-mCherry::HIS3, SYP1-GFP::KanMX*	This study
RPY359.1	*MATa his3-Δ200, leu2-3, 112, ura3-52, bar1Δ::NatR, SLA1-mCherry::HIS3, Hrr25-3xGFP::HIS3*	This study
RPY435.1	*MATα, his3Δ1, leu2Δ0, lys2Δ0, ura3Δ0, GFP-SEC4::URA3*	(Donovan and Bretscher, 2015)
DDY4884	*MATα his3-Δ200, leu2-3, 112, ura3-52, BEM1-GFP::HIS3*	Drubin Lab collection

Chapter 5 : Perspectives and future directions

The goal of my dissertation research was to increase understanding of the molecular mechanisms of clathrin-mediated endocytosis. I demonstrated that a force generating myosin is required to anchor actin assembly to CME sites (Chapters 2 and 3). I also demonstrated that the maturation rate of individual CME sites is regulated by cargo (Chapter 4). Here I will propose future avenues of research in these areas likely to bear fruit.

Actin, myosin, and force generation during CME

While my work has shed light on the mechanism of coordinated force generation by actomyosin during CME, many questions in this area remain unanswered.

In chapter 3, I demonstrated that Myo5, the endocytic type I myosin from budding yeast, is a force generating molecular motor. Measurements and models of actin growth velocity as a function of opposing force indicate that actin filament growth slows considerably when it is opposed by a stiff "cargo" (Footer et al., 2007; Peskin et al., 1993). I proposed that the activity of such a force generating motor could reduce the load on growing actin filaments by pulling them back, away from the barrier they face. Given the exquisite molecular tractability of the budding yeast system and streamlined protocol for imaging CME in this organism, this prediction can be tested experimentally. I expect that eliminating the activity of a force generating motor such as Myo5 would slow actin filament elongation at endocytic sites.

Just as measuring the relationship of between resistive force and velocity has been instructive in understanding myosin motors and actin assembly, similar measurements of the force/velocity relationship of the budding yeast endocytic actin machine would enhance our understanding of CME mechanisms. While actin assembly and myosin motor activity are both required for CME under normal laboratory conditions, it would be interesting to determine whether one system of force generation or the other is sufficient for CME under certain conditions. A possible experimental approach would involve lowering the force barrier to CME in various different mutants using osmotic manipulations (Aghamohammadzadeh and Ayscough, 2009; Basu et al., 2013). If lowering the force barrier to CME obviates the need for either mode of force generation, the conclusion would be that both actin assembly and myosin motor activity are required only in situations where CME is a particular challenge. As with any good result, this conclusion would raise even more questions. Many cell types have differential requirements for actin in CME. For example, epithelial cells require actin assembly for CME on the apical surface but not on the basolateral surface (Boulant et al., 2011). How these cells measure membrane tension and decide whether to deploy actin is incompletely understood. One model involves coincidence detection of membrane curvature along with specific phosphoinositides, a possible signature of stalled clathrin-coated pit intermediates (Daste et al., 2017). If the cells are also making a decision about whether to employ a force-generating myosin, we will have another molecular mystery. Understanding force dependence of the endocytic machinery would not only further our understanding of CME mechanisms, but would also help us articulate questions about cellular decision-making.

Mechanisms of cargo sensing and feedback to endocytic site maturation

Experiments presented here have also revealed that cells have a mechanism to decide when to mature endocytic sites. My data indicate that the decision of whether to proceed through the endocytic pathway hinges upon the presence of cargo. The molecular mechanism of cargo sensing is unknown, but given the simplicity and powerful genetics of budding yeast, pursuing this mechanism is attractive.

The casein kinase Hrr25 is a promising candidate for regulating endocytic progression. My experiments have made it clear that endocytic site maturation, but not necessarily endocytic site initiation, is polarized during the cell cycle together with exocytosis. This conclusion resulted from simultaneous examination of Ede1 and Sla1 localization during different phases of the cell cycle. If a given factor is involved in the decision of whether to mature endocytic sites, elimination of the factor should decrease the rate at which CME sites mature and overexpression should increase the rate at which endocytic sites mature. Hrr25, a kinase previously thought to be involved in CME initiation, may have these characteristics. *hrr25Δ* cells have fewer endocytic sites as marked by Sla1, and overexpression of Hrr25 leads to more endocytic sites as marked by Sla1 (Peng et al., 2015). The alteration in Sla1 site number was previously interpreted to be due to modulation of the initiation rate, but acceleration or deceleration of maturation upon overexpression or underexpression of Hrr25 (respectively) could also explain this result. To determine whether Hrr25 is involved in CME site maturation, Ede1 and Sla1 will need to be simultaneously examined during Hrr25 overexpression or knockdown.

If Hrr25 does in fact influence the rate of CME site maturation, the hunt will be on for mechanisms connecting Hrr25 activity to cargo. Hrr25 phosphorylates several early arriving endocytic proteins, including Syp1 and Ede1, each of which binds endocytic cargo, and Sla2, which along with the epsins Ent1 and Ent2 have been implicated in regulating the transition from the variable to regular phases of CME (Peng et al., 2015; Toshima et al., 2009; Reider et al., 2009; Carroll et al., 2012). It is possible that cargo binding influences the ability of Hrr25 to phosphorylate any of these proteins. Another possibility is that Hrr25's kinase activity towards these proteins is not directly influenced by cargo binding but that cargo stabilizes the early endocytic proteins at CME sites, facilitating lasting phosphorylation. Accordingly, the intensity of early arriving endocytic proteins has been observed to fluctuate during the variable stage of CME (Carroll et al., 2012). While it seems clear that CME progression is modulated by cargo, the underlying molecular mechanisms remain opaque.

References

Aghamohammadzadeh, S., and K.R. Ayscough. 2009. Differential requirements for actin during yeast and mammalian endocytosis. *Nat. Cell Biol.* 11:1039–1042. doi:10.1038/ncb1918.

Basu, R., E.L. Munteanu, and F. Chang. 2013. Role of turgor pressure in endocytosis in fission yeast. *Mol. Biol. Cell*. 25:679–87. doi:10.1091/mbc.E13-10-0618.

Boulant, S., C. Kural, J.-C. Zeeh, F. Ubelmann, and T. Kirchhausen. 2011. Actin dynamics counteract membrane tension during clathrin-mediated endocytosis. *Nat. Cell Biol.* 13:1124–31. doi:10.1038/ncb2307.

Carroll, S.Y., H.E.M. Stimpson, J. Weinberg, C.P. Toret, Y. Sun, and D.G. Drubin. 2012. Analysis of yeast endocytic site formation and maturation through a regulatory transition point. *Mol. Biol. Cell*. 23:657–668. doi:10.1091/mbc.E11-02-0108.

Daste, F., A. Walrant, M.R. Holst, J.R. Gadsby, J. Mason, J.E. Lee, D. Brook, M. Mettlen, E. Larsson, S.F. Lee, R. Lundmark, and J.L. Gallop. 2017. Control of actin polymerization via the coincidence of phosphoinositides and high membrane curvature. *J. Cell Biol.* 216:3745–3765. doi:10.1083/jcb.201704061.

Footer, M.J., J.W.J. Kerssemakers, J.A. Theriot, and M. Dogterom. 2007. Direct measurement of force generation by actin filament polymerization using an optical trap. *Proc. Natl. Acad. Sci. U. S. A.* 104:2181–6. doi:10.1073/pnas.0607052104.

Peng, Y., A. Grassart, R. Lu, C.C.L. Wong, J. Yates, G. Barnes, and D.G. Drubin. 2015. Casein Kinase 1 Promotes Initiation of Clathrin-Mediated Endocytosis. *Dev. Cell*. 32:231–240. doi:10.1016/j.devcel.2014.11.014.

Peskin, C.S., G.M. Odell, and G.F. Oster. 1993. Cellular motions and thermal fluctuations: the Brownian ratchet. *Biophys. J.* 65:316–324. doi:10.1016/S0006-3495(93)81035-X.

Reider, A., S.L. Barker, S.K. Mishra, Y.J. Im, L. Maldonado-Báez, J.H. Hurley, L.M. Traub, and B. Wendland. 2009. Syp1 is a conserved endocytic adaptor that contains domains involved in cargo selection and membrane tubulation. *EMBO J.* 28:3103–3116. doi:10.1038/emboj.2009.248.

Toshima, J.Y., J. Nakanishi, K. Mizuno, J. Toshima, and D.G. Drubin. 2009. Requirements for Recruitment of a G Protein-coupled Receptor to Clathrin-coated Pits in Budding Yeast. *Mol. Biol. Cell*. 20:5039–5050. doi:10.1091/mbc.E09.